The Estimation Methods for an Integrated INS/GPS UXO Geolocation System

by

Jong Ki Lee

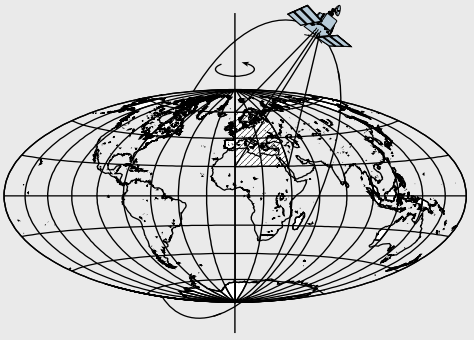

Report No. 493

Geodetic Science and Surveying

The Ohio State University
Columbus, Ohio 43210

December 2009

Abstract

Unexploded ordnance (UXO) is the explosive weapons such as mines, bombs, bullets, shells and grenades that failed to explode when they were employed. In North America, especially in the US, the UXO is the result of weapon system testing and troop training by the DOD. The traditional UXO detection method employs metal detectors which measure distorted signals of local magnetic fields. Based on detected magnetic signals, holes are dug to remove buried UXO. However, the detection and remediation of UXO contaminated sites using the traditional methods are extremely inefficient in that it is difficult to distinguish the buried UXO from the noise of geologic magnetic sources or anthropic clutter items. The reliable discrimination performance of UXO detection system depends on the employed sensor technology as well as on the data processing methods that invert the collected data to infer the UXO. The detection systems require very accurate positioning (or geolocation) of the detection units to detect and discriminate the candidate UXO from the non-hazardous clutter, greater position and orientation precision because the inversion of magnetic or EMI data relies on their precise relative locations, orientation, and depth. The requirements of position accuracy for MEC geolocation and characterization using typical state-of-the-art detection instrumentation are classified according to levels of accuracy outlined in: the *screening level* with position tolerance of 0.5 m (as standard deviation), *area mapping* (less than 0.05 m), and characterize and discriminate level of accuracy (less than 0.02m).

The primary geolocation system is considered as a dual-frequency GPS integrated with a three dimensional inertial measurement unit (IMU); INS/GPS system. Selecting the appropriate estimation method has been the key problem to obtain highly precise geolocation of INS/GPS system for the UXO detection performance in dynamic environments. For this purpose, the Extended Kalman Filter (EKF) has been used as the conventional algorithm for the optimal integration of INS/GPS system. However, the newly introduced non-linear based filters can deal with the non-linear nature of the positioning dynamics as well as the non-Gaussian statistics for the instrument errors, and the non-linear based estimation methods (filtering/smoothing) have been developed and proposed. Therefore, this study focused on the optimal estimation methods for the highly precise geolocation of INS/GPS system using simulations and analyses of two Laboratory tests (cart-based and handheld geolocation system).

First, the non-linear based filters (UKF and UKF) have been shown to yield superior performance than the EKF in various specific simulation tests which are designed similar to the UXO geolocation environment (highly dynamic and small area). The UKF yields 50% improvement in the position accuracy over the EKF particularly in the curved sections (medium-grade IMUs case). The UKF also performed significantly better than EKF and shows comparable improvement over the UKF when the IMU noise probability

density function is symmetric and non-symmetric. Also, since the UXO detection survey does not require the real-time operations, each of the developed filters was modified to accommodate the standard Rauch-Tung-Striebel (RTS) smoothing algorithms. The smoothing methods are applied to the typical UXO detection trajectory; the position error was reduced significantly using a minimal number of control points. Finally, these simulation tests confirmed that tactical-grade IMUs (e.g. HG1700 or HG1900) are required to bridge gaps of high-accuracy ranging solution systems longer than 1 second. Second, these result of the simulation tests were validated from the laboratory tests using navigation-grade and medium-grade accuracy IMUs. To overcome inaccurate a priori knowledge of process noise of the system, the adaptive filtering methods have been applied to the EKF and UKF and they are called the AEKS and AUKS. The neural network aided adaptive nonlinear filtering/smoothing methods (NN-EKS and NN-UKS) which are augmented with RTS smoothing method were compared with the AEKS and AUKS. Each neural network-aided, adaptive filter/smoother improved the position accuracy in both straight and curved sections. The navigation grade IMU (H764G) can achieve the area mapping level of accuracy when the gap of control points is about 8 seconds. The medium grade IMUs (HG1700 and HG1900) with NN-AUKS can maintain less than 10cm under the same conditions as above. Also, the neural network aiding can decrease the difference of position error between the straight and the curved section. Third, in the previous simulation test, the UPF performed better than the other filters. However since the UPF needs a large number of samples to represent the a posteriori statistics in high-dimensional space, the RBPF can be used as an alternative to avoid the inefficiency of particle filter. The RBPF is tailored to precise geolocation for UXO detection using IMU/GPS system and yielded improved estimation results with a small number of samples. The handheld geolocation system using HG1900 with a nonlinear filter-based smoother can achieve the discrimination level of accuracy if the update rate of control points is less than 0.5Hz and 1Hz for the sweep and swing respectively. Also, the sweep operation is more preferred than the swing motion because the position accuracy of the sweep test was better than that of the swing test.

Acknowledgments

I would like to give my deep gratitude to Professor Christopher Jekeli, my academic advisor, for reviewing my dissertation and providing priceless technical advice and having shown the role model. Special appreciation should be extended to Dr. Alan Saalfeld who carefully reviewed the dissertation and gave me lots of valuable recommendation. Dr. Burkkard Schaffrin gave me invaluable experience in both of the theoretical and technical aspects. Also, his statistical and mathematical review and comments made my dissertation a more valuable contribution. I'd like to thank my colleagues, Adem G Hayal, Tindi Abt, Ou Huang, and Dana Caccamise who always showed me the way to figure out problems (with excellent advice).
Finally, I would like to express my special appreciation to my wife Jin Hee Won for her patience and my lovely daughter for supporting me during my academic years.

Preface

This work was supported by a project funded by the US Army Corps of Engineers, Strategic Environment Research and Development Program, contract number W912HQ-08-C-0044. This report was also submitted to the Graduate School of the Ohio State University in partial fulfillment of the PhD degree in Geodetic Science.

Table of Contents

List of Tables

List of Figures

Acronyms

AEKF	Adaptive Extended Kalman Filter
AEKS	Adaptive Extended Kalman Smoother
AI	artificial intelligence
AKF	Adaptive Kalman Filter
ANFIS	Adaptive Neuro Fuzzy Inference System
APD	Asymmetric Probability Density
APD	asymmetric probability density
AUKF	Adaptive Unscented Kalman Filter
AUKS	Adaptive Unscented Kalman Smoother
CBGS	Cart-based Geolocation System
CLT	Central Limit Theorem
DGM	Digital Geophysical Mapping
DGPS	Differential GPS
DOD	Department of Defense
EKF	Extended Kalman Filter
EKS	Extended Kalman Smoother (EKS+RTS)
ESTCP	Environmental Security Technology Certification Program
FBS	forward-backward smoother
GPS	Global Positioning System
HGS	Handheld Geolocation System
IMU	Inertial Measurement Unit
INS	Inertial Navigation System
ISA	industry standard architecture
KF	Kalman Filter
MAP	maximum a posteriori
MEC	Munitions and Explosives of Concern
MEC	Munitions and Explosives of Concern
MEMS	Micro-Electro-Mechanical Sensor
MEMS	micro-electro-mechanical-sensor
MFNs	multi-layer feed forward networks
MMSE	minimum mean-square error
NN	Neural Network

NN-AEKS	Neural Network Adaptive Extended Kalman Smoother
NN-UKS	Neural Network Adaptive Unscented Kalman Smoother
PCMCIA	Personal Computer Memory Card International Association
PDF	probability density function
PF	Particle Filter
PSD	Power Spectral Density
RBPF	Rao-Blackwellized Particle Filter
RBPS	Rao-Blackwellized Particle Smoother
RNs	recurrent networks
RTK	Real-Time Kinematic
RTK	Real Time Kinematic
RTS	Rauch-Tung-Striebel
SERDP	Strategic Environmental Research and Development Program
SFNs	single-layer feed forward networks
SIR	sampling importance resampling
SIS	Sequential Importance Sampling
SIS	sequential importance sampling
SLAM	simultaneous localization and mapping
SPs	sigma points
TFS	two-filter smoother
UAV	Unmanned Airborne Vehicle
UKF	Unscented Kalman filter
UKS	Unscented Kalman Smoother (UKF+RTS)
UPF	Unscented Particle Filter
UPS	Unscented Particle Smoother (UPF+RTS)
US	United States
UT	Unscented Transformation
UXO	Unexploded Ordnance
VDLL	vector delay lock

CHAPTER 1: INTRODUCTION

1.1 Background

Unexploded ordnance (UXO) refers to explosive weapons such as mines, bombs, bullets, shells and grenades that failed to explode when they were employed. In North America, especially in the US, the UXO is the result of weapon system testing and troop training by the DOD (Department of Defense). However, the UXO problem is not limited to military training sites, fields of battle, and military bases. It has been reported that a beach in New Jersey had to be closed since UXO was found to be buried on the beach after an offshore dredging operation to restore the coastline (Capuzzo, 2007). According to the Defense Science Board Task Force on UXO, 15 million acres or more are potentially contaminated at over 1500 different sites (DSB, 1998).

The traditional UXO detection method employs metal detectors which measure distorted signals of local magnetic fields. Based on detected magnetic signals, holes are dug to remove buried UXO. However, the detection and remediation of UXO contaminated sites using the traditional methods are extremely inefficient in that it is difficult to distinguish the buried UXO from the noise of geologic magnetic sources or anthropogenic clutter items such as exploded ordnance fragments and agricultural or industrial artifacts (horseshoes, broken instruments, etc.) (Bell, 2001). Therefore, this traditional method produces high false-alarm rates which cause high (estimated) cost: $400/acre for surface UXO and $1.4 million/acre for buried UXO (Collins et al., 2001; Zhang, 2003). Thus, new UXO detection technologies which can improve discrimination performance for UXO are urgently needed.

Digital Geophysical Mapping (DGM) can provide an accurate characterization of UXO and has been employed for projects which are related to the investigation of UXO. DGM integrates digital output of multiple sensors which are chosen to obtain characteristics of the UXO. However, the use of standard position data integrated with high-quality geophysical sensors has been shown ineffective because the uncertainty of the positions at which data are collected can degrade the inversion performance and thus the subsequent classification (Tarokh et al., 2004; U.S. Army Corps of Engineers, 2006). For example, Bell (2005) argued that the centimeter level of position accuracy was required for successful detection and discrimination using EM61 Hand Held (EM61-HH) data. Billings et al. (2007) showed good discrimination performance given the order of 2 to 5 cm positional errors.

1.2 The Problem of High-Accuracy Geolocation

Geolocation, or determining coordinates of points on or above the Earth's surface, is one of the principal tasks in geodesy and has a history of over two thousand years. Modern methods are taking advantage increasingly of satellite-based radar navigation systems,

such as the Global Positioning System (GPS), which offer centimeter-level precision for static measurements and sub-decimeter precision for mobile systems. Indeed, GPS is the most common geolocation system of choice for any modern mobile navigation system due to its world-wide, all-weather capability combined with extensive user support and minimal cost (to the user). However, for specific local applications, such as in locating Munitions and Explosives of Concern (MEC) and detecting UXO, several other ranging techniques may be considered and, indeed, have been proposed and tested, including laser, radio, and acoustic ranging. Each system whether GPS or one of the other ranging systems, is based on the transmission of a signal from either a base station or the roving unit and the measurement of the travel time to a receiver (either the rover or the base station, respectively). Positioning of the rover relative to a number of base stations with known positions (the satellites in case of GPS) yields through simple geometry the coordinates of the rover. Thus, although much of the modern literature in navigation addresses problems in GPS application, one may consider all such ranging systems equivalent from the viewpoint of data processing and, to a large extent, of noise characterization, as well as environmental handicaps. That is, all such systems rely on an external (to the rover) source to achieve positioning, and that source must be seen (or heard in the case of ultrasonics) by the rover. Intervening obstructions cause a degradation or outright failure in the positioning solution. Some systems are limited in range (even GPS when operated in the real-time differential mode has limited range); others are affected by multipath or electrical interference. Temporal resolution of the positioning solution may be an issue for detection systems with higher velocity, and few if any of the ranging systems include a rover-orientation capability.

The requirements of position accuracy for MEC geolocation and characterization using typical state-of-the-art detection instrumentation are well established. They may be classified according to levels of accuracy outlined in (Simms and Carin, 2004) for the Ordnance and Explosive program:

i. Position tolerance of 0.5 m (as standard deviation) is needed at the *screening level* where areas of interest are determined using airborne or ground-based sensors.
ii. *Area mapping* should be performed with positioning tolerance of 0.05 m (standard deviation). Typically this is done using man-portable and towed array systems.
iii. Position tolerance of 0.02 m or better (standard deviation) is desired for *highly accurate*, *dense data* acquisition systems that are used to interrogate, characterize, and discriminate previously located targets.

The simplest solution to obtain the high position accuracy level for reliable discrimination and classification is to collect data on a fixed grid over the suspected target using a template (Figure 1.1). This method (also called the grid approach) is inexpensive and robust, but the integrated positioning system is much preferred in that the operator can sweep or swing the sensor around above the target in rougher terrain and confined locations.

Also, using the positioning system can facilitate the collection of a much higher density

of data over the target while the grid method can provide only a limited number of samples. Higher data density translates directly to improved signal-to-noise ratio at the processor output and, hence, to improved performance for deeper targets.

Figure 1.1. Collecting data on a grid over a suspected UXO (Bell and Collins, 2007)

The Global Positioning System (GPS) is a precise positioning system that has been used as a workhorse for the last two decades in the geodesy and navigation community. Laser-based ranging, radio, and acoustic ranging can be considered as its alternatives. Since each ranging solution system has the same basic property that a signal is transmitted and is received from either the base or rover station, GPS can be selected as the representative of all ranging solution systems. However, ranging solution systems have limitations such as the intervening obstruction, limited range in some systems, and "line-of-sight" of GPS in wooded or urban area. Also, they have low temporal resolution which diminishes the maximum efficiency when the UXO detection system passes over the estimated target at high speed (Bell, 2005). For high temporal resolution and autonomous navigation system without external signal, a system with an inertial measurement unit (IMU) could be the best option. Generally, the IMU sensor has better quality and performance for short time periods whereas the error of GPS has stationary characteristics in the long term. These complementary features of GPS and IMU can yield the optimal combination for seamless precise positioning under most environments. The three main steps of the integrated IMU/ranging system are data preprocessing, integration technique, and data post-processing with smoothing (Jekeli and Lee, 2007). First, this report focuses on the optimal system integration because the complementary nature of the aiding capability of IMU can be maximized and can produce improved position accuracy of UXO detection systems. The three main filtering techniques; the

(extended) Kalman filter, the nonlinear filters such as the unscented Kalman filter (UKF) and the unscented particle filter (UPF) are studied. The nonlinear filtering methods, which have recently been considered for the navigation problem, are especially applicable to the dynamics associated with UXO detection platforms that may experience rapid changes in orientation and acceleration.

Second, since detection system data are likely subjected to post-processing for characterization and discrimination of UXO, smoothing techniques, such as the Rauch-Tung-Striebel (RTS) backward smoother based on the extended Kalman filter (EKF), can be implemented to yield superior positioning results when there are ranging solution gaps. These types of smoothing are adapted to the nonlinear filters, yielding the EKF-based RTS smoothing, the UKF-RTS smoothing, and the UPF-RTS smoothing.

However, these filters and smoothers cannot overcome the natural accumulation of process errors as the ranging solution update interval increases, especially in dynamic environments. The artificial intelligence based adaptive methods, such as neural networks, have been proposed as alternative methods for adaptive filtering methods for bridging signal blockage. The neural networks aided adaptive filters are employed to bridge gaps in the ranging solution in quiescent and moderately dynamic environments.

Finally, these proposed filters/smoothers are integrated using Rao-Blackwellization. In Rao-Blackwellized filter, the states can be divided into two subspaces and estimated by the linear filter (Kalman filter) and a nonlinear (non-Gaussian) filter, respectively. Therefore, at first, the neural-network-based filtering method can be applied for the linear filter. Second, the (unscented) particle filter and smoother are tailored for the nonlinear (non-Gaussian) filter part.

1.3 SERDP and ESTCP Geolocation Projects

A number of geolocation and DGM related projects within ESTCP (Environmental Security Technology Certification Program) and SERDP (Strategic Environmental Research and Development Program) have been performed during the last several years. The GPS-based geolocation systems for UXO detection achieved a few decimeters of accuracy (initial screening accuracy level, but not area mapping and characterization level). Real-Time Kinematic (RTK) GPS, (Robotic) Total Station system, laser, radio, or acoustic systems have all been tested as ranging solution systems. However, each system has its own limitation such as gaps caused by signal occlusion by artificial structure, vegetation or terrains and in some cases low temporal resolution. It was concluded that all such geolocation systems could benefit from augmentation with inertial measurement unit. But, the ability to bridge gaps by the augmented system depends on the quality of IMU and the duration of the gaps. Therefore, the integrated IMU and ranging system is the target system of study for UXO detection and characterization.

A number of ESTCP and SERDP research and development projects have specifically addressed the geolocation and digital geophysical mapping problems for UXO detection and remediation (U.S. Army Corps of Engineers, 2006; Foley, 2006; Bell and Collins, 2007). The most systematic and comprehensive study involved a four-phase investigation, coordinated and funded principally by ESTCP, among other supporting agencies of the Army. Each successive phase of the project built on the previous results

of geolocation demonstrations by various participating vendors in controlled environments (test ranges) of different types of terrain and with likely obstructions of the transmitted signal (such as wooded areas). The participants represented the full range of navigation and digital geophysical mapping (DGM) technologies available today, and the demonstrations were designed to exercise each technology for potential subsequent enhancement and commercial development. The basic geolocation technologies may be grouped into GPS (including differential GPS, i.e., DGPS), which represents a global geolocation capability, and local laser/radar/ultrasonic tracking, with inertial aiding in each case. Since this report focuses on the integration with inertial measurement units, the following synopsis of ESTCP's four-phase project emphasizes the results associated with inertially aided systems.

Phase I was designed to test navigation equipment only, whereas subsequent phases of the project continued with selected navigation systems integrated with geophysical detection instruments. Eight participants tested different levels (of accuracy) of GPS, inertial measurement units, and laser/radio frequency tracking systems. Both open and obstructed (wooded) areas were used at the McKinley Range in Huntsville, Alabama. Performance of the systems was quantified by the average of the deviations of the indicated positions from values determined independently by standard civil surveying techniques with an accuracy of 0.003 m using total station electronic distance measurements.

In open, unobstructed areas, the GPS systems performed at the level of 0.04 m to 0.9 m accuracy, depending on the quality of the receiver and whether differential GPS was employed (generally yielding better accuracy, but limited in range due to the required radio link for real-time differential corrections). Inertial measurements did not improve these basic geolocation results in the case of unobstructed GPS coverage. The local laser tracking systems performed best (due to their higher frequency compared to the GPS signals), usually at the sub-centimeter level of accuracy.

In wooded areas, the IMU-aided navigation systems clearly demonstrated their ability to bridge GPS outages or loss of differential updates due to the obstructing vegetation. Accuracy was at the level of 0.6 m to 0.7 m for the aided systems compared to 2.1 m accuracy of the unaided (non-differential) GPS. It should be noted that this level of IMU aiding was achieved with the medium-accuracy (tactical grade) sensors (such as the Honeywell HG1700). One participant (Paper Pilot) used a low-cost (low-accuracy) IMU (the Crossbow IMU400CA) and achieved no improvement over unaided real-time GPS positioning (3.3 m). Table 1.1 summarizes the salient results of Phase I. The average accuracies refer to the radial horizontal deviations from the control values. Three-dimensional positioning apparently was possible for all systems, but was not assessed.

participant	systems	range [m]	average accuracy [m]
CEHNC[1]	Garmin GPS	100	2.19
Arinc, Inc.	GPS – similar to Garmin	100	25.93
Paper Pilot Research,Inc.	Garmin GPS, Crossbow IMU400CA	100	3.29
Ensco, Inc.	spread-spectrum radio navigation system	50	0.93
Shaw Environmental	Leica TPS1100 dual laser robotic total station	100	0.09
Arcsecond, Inc.	laser tracking system	45	0.08
Parsons	Trimble 4700 RTK GPS, Honeywell Talin INS	100	0.64
Blackhawk	Applanix GPS and IMU	100	0.67

[1] U.S. Army Engineering and Support Center (Corps of Engineers, Huntsville Center)

Table 1.1. Performance of navigation systems tested in a wooded area under Phase I.

In Phase II of the ESTCP project, the participants, in part, upgraded their navigation systems and integrated them with typical UXO detection instrumentation (EM-61 and G-858 geophysical sensors). Thus, two types of position indicators were evaluated: directly from the navigation system as the system was co-located with a surface point and indirectly from the geophysical sensor peak reading (as it located a potential object of detection). The latter is termed integrated positioning and its accuracy depends also on the quality of correlation between the navigation system output and the identification of a detected signal. The integrated positioning generally is somewhat poorer in quality than that derived from the direct surface point localization. A slightly different group of participants demonstrated their systems in this phase of the project, and some salient results are summarized in Table 1.2. The geolocation accuracy decreased noticeably in some cases when going from a direct surface point indication to a geophysical sensor indication. Also, there was no substantial difference between profile and area map geolocation capability. As before, the higher performance IMU of the Blackhawk system maintained the DGPS accuracy better than the low-accuracy unit used by Paper Pilot Research, even though the latter in these tests was augmented by an electronic compass to aid in bounding the gyro drifts.

participant	systems	average accuracy [m] [1]	average accuracy [m] [2]	average accuracy [m] [3]
CEHNC	NovAtel RTK DGPS	NA [4]	1.08	NA
CEHNC	Ultrasonic ranging system	NA	NA	0.48
Shaw Environmental	Leica TPS1100 dual laser robotic total station	0.10	0.42	0.42
Blackhawk	Applanix GPS and IMU	1.07	1.39	1.14
Where Co.	Ultrasonic ranging system	NA	NA	0.70
Ensco, Inc.	spread-spectrum radio navigation system	NA	0.98	0.82
Arcsecond, Inc.	laser tracking system	0.39	0.37	0.46
Paper Pilot Research, Inc.	Garmin GPS, Crossbow IMU400CA, Honeywell MMR 330 electronic compass	5.40	4.25	3.92
Gifford Integrated Sciences	NovAtel RTK DGPS, Hexamite ultrasonic ranging system	NA	1.19	NA

[1] navigation system only
[2] integrated positioning along a geophysical profile
[3] integrated positioning from a geophysical gridded map
[4] NA = not acquired

Table 1.2. Performance of navigation systems tested in wooded areas under Phase II.

Phase III of the ESTCP project further tested the navigation technology integrated with geophysical sensors in a variety of obstructed and sloped terrains, as well in the ability to conduct ultra-local positioning (within a one-meter square) to aid in the characterization of detected objects. Only four participants demonstrated their integrated navigation equipment that, however, covered the spectrum of geolocation technologies: DGPS, ultrasonic ranging, laser ranging, radio navigation, and inertial navigation. The laser systems operated at all resolutions, while the DGPS system was augmented by ultrasonic ranging and an electronic compass, and the radio navigation system was augmented by an inertial measurement unit. In essence, the IMU provided local area navigation enhancement at the 0.03 m to 0.05 m accuracy level, which was competitive with the laser ranging (0.01 m) and ultrasonic (0.10 m) capabilities under equal circumstances. Details of the many tests and demonstrations conducted at the Aberdeen Proving Grounds under Phase III of the project are provided in the final report (U.S. Army Corps of Engineers, 2006), which concluded that the IMU enhancement was “clearly better” than the ultrasonic ranging augmentation.

Phase IV of the project is continuing with further analysis using the collected data in Phase III demonstrations. For example, the ArcSecond Constellation system which provides *position-tracking* hardware and software was employed as an integrated detection system. The position of the ArcSecond system is stored at 40Hz for post-

processing. Also, the system is integrated with the hand-held dual Magnetic/EMI sensor by AETC Incorporated, the SQUID by Battelle, and the EM-61 MK II and G-858 by CEHNC (Figure 1.2). The controlled testing in a small local area shows 0.003~0.004 m position accuracy. However, 11 individual tests in the UXO contaminated test site yield 0.10 m accuracy when position was averaged from the magnetometer readings (U.S. Army Corps of Engineers, 2006).

Figure 1.2. ArcSecond Constellation System (U.S. Army Corps of Engineers, 2006)

Most other past ESTCP and SERDP projects concerned with UXO detection systems have incorporated positioning systems based on GPS. Only one included IMU aiding (Table 1.3) and two others considered additional orientation measurements using also GPS or tiltmeters. None of these projects specifically analyzed the positioning system capabilities to the extent of the ESTCP demonstrations at the McKinley Range and Aberdeen Proving Grounds. Limitations in GPS due to loss of signals were noted in many project reports; and, accuracies of the order of 5 cm - 15 cm were claimed when the system was functioning optimally; (however, details of the determination of these performances in positioning were not provided).
Ongoing projects (as of this writing) specifically or tangentially addressing geolocation analysis are supported by SERDP and partly also stem from the ESTCP demonstration tests at the McKinley Range and Aberdeen Proving Grounds (Table 1.4). Positioning accuracy claims range from mm to sub-meter levels.

Project #	Project title and organization	instruments	comments
MM - 9526	Multi-Sensor Towed Array Detection System (MTADS); *Naval Research Laboratory*	5 Hz RTK GPS, IMU, compass, odometer	20 cm – 30 cm; GPS was also used for orientation (1º)
MM - 0035	Geonics EM-63 Multi-Channel EM Data Processing Algorithms for Target Location and Ordnance Discrimination; *Geophysical Associates*	DGPS (1 Hz)	repeats are necessary if gaps occur in GPS positioning
MM - 0036	Development and Demonstration of a Handheld, Broadband Electromagnetic UXO Sensor; *Geophex, Ltd.*	DGPS (1 Hz)	reduced positioning accuracy under tree cover
MM - 0105	UXO Characterization With a Fast 4-D TEM System; *Zonge Engineering and Research*	Leica SR530 RTK GPS, compass, tiltmeter	positioning standard deviation:5 cm (static) 10 cm (dynamic)
MM - 0208	Combined Electromagnetic and Magnetometer Data Acquisition and Processing; *U.S. Army Corps of Engineers*	GPS (1 Hz)	cm-level GPS is affected by GPS outages
MM - 0418	Coaxial EMI Sensor for UXO Detection and Discrimination; *Geophex, Ltd.*	DGPS	tight integration of GPS with EMI
MM - 4003	Advanced MTADS Classification for Detection and Discrimination of UXO; *Naval Research Laboratory*	5 Hz RTK GPS (Trimble MS750); dual GPS for azimuth; IMU	positioning standard deviation: 15 cm (horizontal)
MM - 9812	Electromagnetic Induction and Magnetic Sensor Fusion for Enhanced UXO Target Classification; *Naval Research Laboratory*	see MM-4003	see MM-4003
MM - 9902	Ultra-Wideband, Fully Polarimetric Ground Penetrating Radar for UXO Discrimination; *U.S. Army Corps of Engineering, Ohio State University Electro-Science Laboratory*	GPS, digital compass	
MM - 1310	Sensor Orientation Effects on UXO Geophysical Target Discrimination; *Sky Research, Inc.*	Leica laser total robotic station (RTS), Crossbow AHRS400	3-D positions at the mm-level (10 Hz update rate)
MM - 1381	Handheld UXO Sensor Improvements to Facilitate MMO/Clutter Discrimination; *AETC, Inc.*	low-cost IMU	Integration of IMU with EMI using Hidden Markov Model
MM - 1565	Technical Assessment of IMU-Aided Geolocation Systems for UXO Detection and Characterization; *The Ohio State University*	GPS, IMUs	non-linear (and non-Gaussian) filters are tested and compared with traditional filters

Table 1.3. Recently completed UXO detection projects and their positioning methods.

Project #	Project title and organization	instruments	comments
MM - 1441	UXO Navigation Technology, Sky Research, Inc.	see MM-1310	see MM-1310
MM - 0029	UXO Precise Position Tracking Using Time-Modulated Ultra-Wideband Communications, U.S. Army Corps of Engineers	local radio transmitters	not available
MM - 0207	Long Range Ultrasonic Tracking System, U.S. Army Corps of Engineers	Acoustic ranging system	not available
MM - 0604	Inertial Navigation System Improvements for Target Characterization Using Small-Area Inertial Navigation Tracking (SAINT), U.S. Army Corps of Engineers, ENSCO		
MM - 0437	A Multisensor System for the Detection and Characterization of UXO, Lawrence Berkeley National Laboratory	GPS	not available
MM - 0608	Transportable Manned and Robotic Digital Geophysical Mapping Tow Vehicle, U.S. Army Corps of Engineers, Arcsecond, Inc.	laser ranging system	sub-meter accuracy
MM - 1564	High-Accuracy Multisensor Geolocation Technology to Support Geophysical Data Collection at MEC Sites, The Ohio State University, Department of Civil & Environmental Engineering	GPS, INS, RF, TLS	cm level accuracy
MM - 1565	Inertial/GPS Integrated Gelocation System for Detection and Recovery of Buried Munitions, The Ohio State University, School of Earth Sciences Division of Geodesy and Geospatial Science	GPS, INS	cm level accuracy

Table 1.4. Ongoing SERDP Geolocation Projects.

In summary, the problem of geolocation for UXO detection and remediation is being addressed with some type of ranging system, whether GPS, laser, radio, or acoustic system. Each system has limitations, including occultation of the signal by intervening structures, vegetation, or terrain. Some systems, particularly GPS, are more susceptible to local vegetation canopies; others are limited in range. All would benefit from augmentation by a system that does not rely on external signal sources. Such a system is the inertial measurement unit. However, its ability to bridge gaps in the ranging systems depends on the quality of the inertial sensors (hence their efficacy is correlated with cost) and the duration of the gaps, due to the accumulation of sensor error with time.
It is clear from the various geolocation demonstrations and detection experiments that the first level of accuracy, the screening level, is attainable with an appropriate ranging system under most circumstances, although this aspect of UXO detection and remediation can still offer a challenge. The other levels of accuracy, at few-centimeters, appear achievable, but the positioning system options are fewer. IMUs and laser ranging have been demonstrated to meet this accuracy. However, since laser ranging systems still require acquisition of a remote (potentially degraded or obstructed) signal, it seems prudent for the most general application to consider IMUs foremost and ideally aided by a laser ranging system, if not GPS. For this reason the integration of IMUs with GPS (although a laser ranging system could easily be substituted; the algorithms would not change) will be considered.

1.4 Outline

The brief overview of INS/GPS integration, especially the focus on data processing, is presented in chapter 2. This chapter aims to provide an overview of the concept of INS/GPS integration and studies integration modes and data processing steps of the INS/GPS integration.
In chapter 3, a detailed algorithm overview of different methods for nonlinear recursive estimation (filtering/smoothing) is provided. The nonlinear filter's ability to obtain precise position and orientation in an exemplified UXO geolocation environment (high dynamic and small area) is validated through designed simulation scenarios.
Chapter 4 explores the neural network (NN) method for adaptive filtering to overcome inaccurate a priori knowledge of the process noise of the system. It is compared with traditional adaptive filtering techniques by using laboratory tests (real data set). Furthermore, these developed NN-aided filtering methods are integrated with the smoothing method described in chapter 3. Results given in chapter 3 show that the nonlinear filters such as UKF and UPF perform better than traditional filters.
In chapter 4, adaptive filtering with neural-network-aiding improved the position accuracy as well as homogenizes the result of the integrated system over a range of relatively quiet to dynamic environment. Therefore, chapter 5 integrates these two advanced methods into one algorithm, an approach called Rao-Blackwellization. The Rao-Blackwellized particle filter is tailored for precise geolocation of an UXO detection system and was tested and analyzed using a hand-held geolocation system. Finally, Chapter 6 gives conclusion and recommendations.

CHAPTER 2: INS/GPS INTEGRATION

Since every ranging system requires some form of aiding (e.g., bridging signal gaps) in general application environments, INS/GPS integration has been discussed as a way to improve positioning resolution and accuracy, as well as to bridge GPS gaps including signal loss and degradation. As indicated in the previous chapter, GPS can be representative of all other ranging systems in the algorithmic development. Any ranging solution system essentially achieves long-term error stability, with possible short-term failure, degradation, and coarseness; whereas, IMU is characterized by its short-term reliability and high resolution, yet long-term error growth. These complementary features have encouraged the attempts to integrate IMU and GPS. The Kalman filter has been the most widely used algorithm to achieve the integration. Concepts, some basic trade-offs, and currently developed algorithms are introduced with various limitations in this chapter.

2.1 Integration Modes

Generally, integration of INS and GPS is classified according to the mechanization and architecture through which information is shared between an inertial navigation system and a GPS receiver. Over the last few decades, the terms such as loose, tight, ultra-tight and deep have been used in order to describe information shared between the two components through different architectures (Jekeli, 2000; Scherzinger, 2000). In addition, INS/GPS integration is categorized as centralized and decentralized according to the processing algorithm type. Table 2.1 summarizes the INS/GPS integration types according to the mechanization and processing type.

Mechanization	Processing Type
Uncoupled Integration	Decentralized
Loose Integration	
Tight Integration	Centralized
Deep or Ultra-Tight Integration	

Table 2.1. Classification of INS/GPS integration.

In uncoupled, decentralized INS/GPS integrated systems, data from the IMU and GPS receiver are processed independently, and then combined in some sub-optimal or optimal

manner (Figure 2.1). GPS-derived positions can be used to reset IMU outputs continually in case that IMU positions are needed in the absence of a GPS solution). In the figure, ϕ and λ refer to position coordinates, latitude and longitude, respectively. The inertial navigation system (INS), in order to calculate a position, uses incremental angles ($\Delta\theta$) derived from gyros and incremental velocities (Δv) derived from accelerometers. The GPS receiver uses measured range (s) and carrier signal phase (φ) in order to yield a position (Jekeli, 2000).

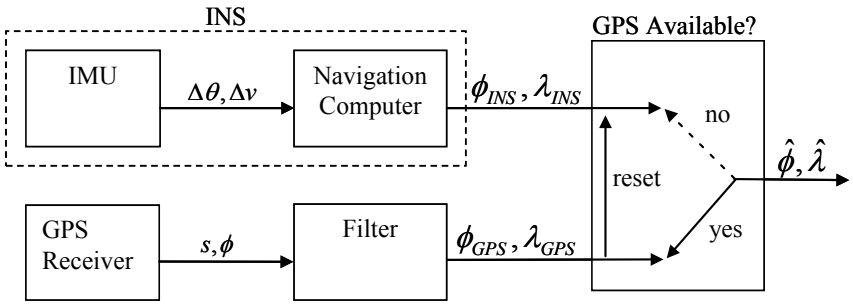

Figure 2.1. Uncoupled, decentralized INS/GPS integrated system.

The loosely coupled integration estimates systematic errors in the IMUs by external observations that are obtained by using pre-processed data (usually positions) from the GPS receivers (Figure 2.2). Optimal (least-squares) estimation accounting for random errors is implemented by adopting filtering techniques such as the Kalman Filter. Thus, in case of GPS outages, the IMU error estimates obtained with a Kalman filter based on the previously accumulated GPS information can compensate somewhat for inertial navigation errors during the outages.

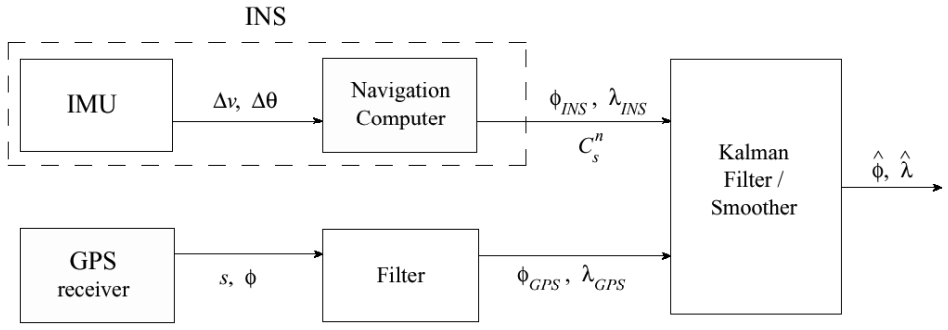

Figure 2.2. Loosely-coupled, decentralized INS/GPS integrated system. Same notations as in Figure 2.1; C_s^n is the rotation matrix from sensor to navigation frame.

Figure 2.3 illustrates centralized integration of IMU and GPS. The centralized integration is different from decentralized integration in that GPS (pseudo-range and phase information) and IMU (accelerometer and gyroscope) data are combined to generate a single blended navigation solution instead of determining individual position solutions. Generally, this configuration provides a more accurate solution than decentralized integration. It also has the advantage in so far as it can provide a more robust and reliable solutions even when fewer than four satellites are in sight (Petovello, 2003). However, it requires intensive computations and access to raw IMU and GPS data. Furthermore, since this architecture is not independent, the growing error of IMU can affect the accuracy of the blended solution as well as the GPS solution.

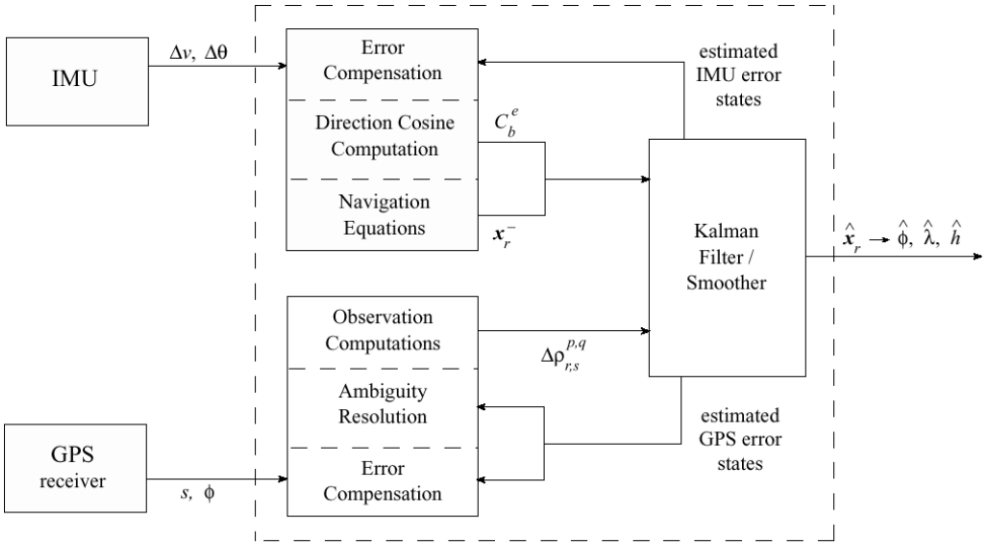

Figure 2.3. Centralized INS/GPS integrated system. Same notations as in Figures 2.1 and 2.2; x denotes the vector of all error states, C_b^e is the rotation matrix from the body frame to the Earth-fixed frame, and $\Delta\rho$ is the double-differenced range from GPS.

Deep integration (or ultra-tight integration) refers to the mechanization shown in Figure 2.4. The GPS receiver is different from the traditional GPS receiver which is used for decentralized and centralized integration. The traditional GPS receiver which has code and carrier tracking loops is replaced by a single vector delay lock (VDLL) receiver. Also, the information from the IMU is used as an integral part of the GPS receiver. Therefore, the deep integration architecture has the advantage that it enhances the robustness of the receiver to avoid interference and jamming. In the meantime, this approach is feasible only with the approximate firmware of the receiver and IMU sensors. Therefore, this strategy has been adopted only by hardware manufacturers or companies that have invested considerable resources toward INS/GPS applications.

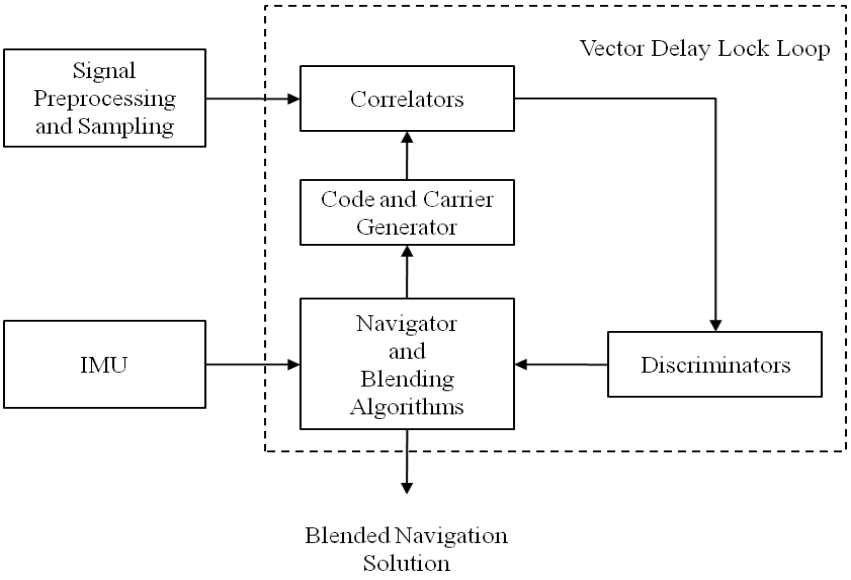

Figure 2.4. INS/GPS Deep Integration system (Petovello, 2003).

2.2 Data Processing

The INS/GPS integration generally involves three steps: data preprocessing, integration/filtering, and post processing/smoothing. In discussing methods available for each step, it is worth mentioning that the filter design has recently undergone remarkable evolution in the positioning and navigation applications. Behind the evolution it is recognized that most instrument error processes are clearly nonlinear while the typical filter follows linear state equations which basically assume linear error behavior; on the other hand, a particular (even nonlinear) error model is not necessarily an accurate characterization of the system.

Table 2.2 lists the approaches that have been considered for each step. Each approach is briefly reviewed in the rest of this chapter while more details of the algorithms employed in the various approaches will be discussed in Chapters 3, 4, and 5. It is noted that the cited applications center almost exclusively on vehicle navigation rather than local problems of Munitions and Explosives of Concern (MEC) detection and characterization. However, the concepts developed and tested for navigating and positioning a vehicle are relevant to the present focus of geolocation of, e.g., man-portable and towed array systems.

Steps			Approach
Data pre-processing			Wavelet De-Noising
Integration	Filtering	Linear	KF (Kalman Filter)
		Nonlinear	EKF (Extended Kalman Filter)
			UKF (Unscented Kalman Filter)
			UPF (Unscented Particle Filter)
		Adaptive	AEKF (Adaptive Extended Kalman Filter)
			AUKF(Adaptive Unscented Kalman Filter)
		Hybrid	RBPF (Rao-Blackwellized Particle Filter)
	Neural Network		NN-aided Filtering or Adaptive Filtering
	Fuzzy Logic		ANFIS (Adaptive Neuro-Fuzzy Inference System)
Data post-processing			RTS (Rauch-Tung-Striebel)

Table 2.2. A reference guide to approaches for each step of INS/GPS processing.

2.2.1 Data Preprocessing

Errors in the gyro and accelerometer outputs are generally a combination of correlated and uncorrelated noises. While simple averaging or weighted smoothing has been employed to reduce white noise components, stochastic error models have been introduced in order to model correlated components. It has been found that the performance of inertial sensor measurements improves when the white noise is removed by using a more specific separation of signal from noise. This de-noising technique is achieved by decomposing the output into signal and noise with wavelet transforms. Typical reductions in the subsequent positioning error range from 13% ~ 34% (integrated GPS/INS) to 60% (free-inertial navigation), as shown in Nassar (2003) in which the test data were obtained on a road vehicle with medium and high-grade IMUs (see also Skaloud (1995) and Osman et al. (2003)). El-Sheimy et al. (2004) reported similar results for orientation estimation. Also, Elhabiby et al. (2008) isolated or extracted systematic error (mainly multipath) from the GPS measurements by adopting wavelet multi-resolution analysis with a new trend detection method. Based on their findings, they concluded that wavelet de-noising proved to be an effective tool for reducing the white noise effect of IMUs on both free and integrated inertial navigation solutions. Further research on the data pre-processing step is primarily directed toward designing new wavelet transforms or searching for more effective wavelet transforms that improve the separation of noise from the dynamics of the sensed vehicle motion. For example, Guo et al. (2003) employed bi-orthogonal spline wavelets instead of the more complicated Debauchies wavelets, and found improved accuracy in orientation estimates from gyro data.

2.2.2 Filtering

Researchers have taken various estimation approaches in order to provide a more optimal combination of IMU and GPS in numerous applications. The approaches can generally be categorized into two main types: filtering and artificial intelligence (AI) methods.

Furthermore, filtering methods can be classified into linear/non-linear filters (KF vs. EKF, UKF, and PF) or Gaussian/Non-Gaussian filters (KF, EKF, and UKF vs. PF).
The Kalman Filter (or Extended Kalman Filter, EKF, for nonlinear systems) has been widely used for a long time and has built up its reputation as the "workhorse" in estimating positions for navigation applications, especially for integrated INS/GPS systems (Salychev and Schaffrin, 1992; Salychev, 1999; Rogers, 2000; Jekeli 2000; Titterton and Weston, 2004). The notion of EKF can be explained by two key assumptions: linearity and minimum mean-square error (MMSE). First, Taylor series expansions are applied both to the nonlinear system that describes the error dynamics state equations and to the (usually) nonlinear observation equations that relate external updates (i.e., observations) to the system errors. These series are truncated at the linear term, thus linear approximation models are created. Second, the minimum MSE criterion is employed as shown by Schaffrin (1995). For this optimality criterion, it is not necessary to assume that the probability density function (PDF) of the system error states is Gaussian (Gordon et al., 1993; Gelb, 1974; Grewal and Andrews, 2001). Based on these premises (linearity and MMSE), the optimal values of the error states are determined and propagated in time under the minimum Mean Squared Error criterion. The process can equivalently be explained as a sequential least-squares fit of a linearized dynamic model to given observations related to the states that are stochastically constrained to vary in time according to a particular dynamics model (for additional details, see the detailed derivations in Schaffrin, 1995 or in Jekeli, 2000).
In the meantime, the first premise of the filter introduces limitations or possible difficulties in its implementations. For example, Julier et al. (2000) contend that the EKF may fail to execute when the Jacobians are complicated and time-consuming expressions (requiring reevaluation at every prediction step of the filter). Also, in order for the EKF to execute, the error dynamics of the system must be describable in terms of small error increments. Therefore, when the system and/or observations are significantly nonlinear, the first-order approximations can cause instability such as biased solutions and inconsistency in or divergence of the propagated covariance, respectively MSE. Nevertheless, the EKF has enjoyed widespread applications in processing integrated INS/GPS systems among many other time-dependent systems. Recent investigations for various mobile applications include but are not limited to Shin (2001), Redmill et al. (2001), Petovello (2003), and Zhang (2006).
In order to address the problem of linearization under Gaussian error behavior, Julier and Uhlmann (1996) and Julier et al. (1995, 2000) developed the unscented Kalman filter (UKF), a recursive application of the unscented transformation of state variables through the non-linear state dynamics model. The major motivation behind the UKF was to retain the Gaussian character (statistics) of the system states better by directly applying the nonlinear propagation function on a suitably chosen sample of states rather than by applying a linear approximation on a single estimate of the states (Julier and Uhlmann, 1996). Thus, it still remains the same assumption that the states are to be Gaussian random variables. However, their statistics are now represented deterministically by using a minimal set of carefully chosen sample points, namely the sigma points (SPs) which accurately (to third order) capture the true mean and covariance of the random states and represent the transformed mean and covariance with the similar degree of

accuracy when propagated through the nonlinear system (van der Merwe and Wan, 2004). Various studies have pointed out the effectiveness of the unscented Kalman filter over the traditional extended Kalman filter in navigation applications. Van der Merwe et al. (2000) predicted an improvement by up to 30% on an unmanned airborne vehicle (UAV). Zhang et al. (2005) also obtained higher accuracy compared with the extended Kalman filter on a land vehicle equipped with IMU, GPS, and digital compass. On the other hand, St. Pierre and Gingras (2004) reported only slightly improved results, and Shin (2005) found mixed results based on the simulation and the land vehicle IMU analysis. Similarly, Yi and Grejner-Brzezinska (2006) obtained improvement with GPS blocked (free-inertial navigation), but no improvement during periods of GPS coverage. The research trend of UKF is mostly directed toward applying adaptive algorithms for better orientation (also position) estimation under different dynamic environments; see, e.g., Pourtakdoust and Ghanbarpour (2007), Song and Han (2008).

In addition to the UKF, the sequential Monte Carlo method, also known by the names, particle filter (PF), bootstrap filter, condensation algorithm, and survival of the fittest method, was developed as a nonlinear/non-Gaussian estimator based on Bayesian filtering theory (Gordon et al., 1993). PF is different from the UKF in that it randomly selects many samples in order to allow any (usually unknown) type of probabilistic distribution while the UKF requires a smaller sample to characterize the Gaussian nature of the variables. The sequential Monte Carlo method or PF, which had been already used by physicists in the 1950s (Andrieu et al., 2003), became more popular with the increase in computing power in the 1990s as a way to address practical problems such as radar target tracking, communications, econometrics, and computer vision (Godsill et al., 2000). Recently, they have been applied to the problems of integrated navigation systems (e.g., Hawkins et al., 2005; Nordlund and Gustafsson, 2001; Gustafsson et al., 2001). Since particle filters do not have to make any assumptions on the PDF and can deal with nonlinearities, they have yielded numerical accuracy superior to other filtering methods (Gordon et al., 1993; Doucet, 2000; Aggarwal et al., 2006).

Van der Merwe et al. (2000) combined the PF with other filters such as the UKF to refine the initially generated particles, and called it the unscented particle filter (UPF). Several studies documented that this approach yielded a better approximation for the conditional pdf of the states and improved accuracy in many positioning-related applications (Arulampalam et al., 2001; Grewal and Andrews, 2001; van der Merwe et al., 2000).

When it comes to the PF's drawback, it is that sampling in high-dimensional space can be inefficient because a large number of samples are required to represent the a posteriori statistics (Doucet, 2000). In some cases, the model can have a "tractable substructure", which can be analytically marginalized out (i.e., also, called Rao-Blackwellization). The analytical marginalization can be carried out by using standard algorithms such as the Kalman Filter; then, we only need to sample the remaining part by adopting a PF. In general, the Rao-Blackwellized Particle Filter (RBPF) yields more accurate estimates with small variation of state than the standard PF (Doucet, 2000). For example, the RBPF yielded the improved estimation results when applied to an integrated navigation system (Nordlund and Gustafsson, 2001). Giremus (2003) obtained similar results with the RBPF used for a tightly coupled INS/GPS integration (PF used for GPS, KF used for the INS part). Vernaza and Lee (2006) showed the superiority of RBPF over the

traditional KF in view of noisy sensors and high initial uncertainty in tracking simulations. Euston and Kim (2007) also applied RBPF for the inertial-based airborne simultaneous localization and mapping problem (SLAM) and showed a significant improvement in flight simulation.

The limitation, common across different navigation filters, is that they are adversely affected by potentially inaccurate system and measurement noise statistics. Particularly for highly dynamic trajectories (e.g., one that may be encountered by UXO detection equipment), the error statistics may vary in time, and it can lead to invalidating initially defined models. Adaptive methods are often employed in order to improve the filters under such circumstances and mitigate the adverse effects. One frequently used method that adapts to the potentially changing process and measurement noise characteristics is to estimate the corresponding covariances by using the Kalman filter innovations (Schaffrin, 1994; Salychev, 1999). Research in this area is mostly directed toward new adaptive algorithms that better characterize sensor errors under different dynamic environments; see, e.g., the studies by Salytcheva (2004), Hide et al. (2004), and Ding et al. (2006) that demonstrated significant improvements in navigation accuracy when adaptive methods are used.

AI is also considered a successful and effective solution to certain engineering and science problems which cannot be addressed by adopting conventional methods (Cawsey, 1998). AI-based filters are distinguished from other filters in that they do not employ a formal mathematical model for the system dynamics and measurements. Furthermore, there are no statistics associated with the output solution since they do not use any statistical information on the input (even though it usually has a random component). Therefore, this limitation may make AI-based methods less suitable for the present applications of high-accuracy geolocation. However, it has been pointed out that the AI-based methods may exhibit better performance when quite long measurement outages occur (e.g., see Wang et al., 2006).

Among various AI-based techniques, the neural network could be selected to aid adaptive filters because it learns input-output relationships without a priori knowledge of the dynamic models and noise statistics of the measurements. The neural network has already been employed with success for similar applications in many studies (e.g., Jwo and Huang, 2004, Wang et al., 2006, 2007, Kornuyenko et al., 2005, and Chiang, 2005). More specifically, Wang et al. (2006) proposed a hybrid neural network and Kalman filter approach to reduce KF drift during GPS outages. Also, Wang et al. (2007) used the neural-network-aided adaptive KF to account for vehicle dynamic variations and to improve the navigation solution. Zhan and Wan (2006) derived a multi-layer, neural-network-based unscented Kalman filter for nonlinear estimation, and showed that the simulation results indicated overall improvement in the filter performance.

2.2.3 Smoothing

The Rauch-Tung-Striebel (RTS) backward smoother is a fixed-interval smoothing algorithm that is commonly used for bridging GPS outages in the post-processing mode. Any postprocessing smoothing technique that employs endpoint calibration will yield results superior to simple forward estimation. (Jekeli, 2000; Haykin, 2001). Compared with other fixed-interval smoothers, the RTS algorithm has advantages including easy

and simple implementation (Meditch, 1969; Gelb, 1974; Brown and Hwang, 1992; Jansson, 1998). Although, in general, smoothing only applies to post-processing rather than real-time applications, it may be considered for *near* real-time estimation. In addition to the traditional Kalman filter smoothing, alternative algorithms have been developed for the unscented and particle filters (Shin, 2005) with only marginal, if any, improvement over the former in the final navigation errors. Apparently the strength of the endpoint calibrations can readily overcome deficiencies in the IMU error dynamics model. However, if post-processing is an option, all types of smoothing should be considered for optimal performance.

The Rauch-Tung-Striebel (RTS) fixed-interval smoother can be combined with any of the aforementioned adaptive forward filters. For example, such combinations have yielded the adaptive Extended Kalman Smoother (AEKS) and the adaptive Unscented Kalman Smoother (AUKS, also called Unscented RTS Smoother (Sarkka, 2008))

Since the INS/GPS integration can improve the position accuracy of the UXO detection system and has the ability to bridge gaps in the positioning of the detection system due to signal blockages and signal degradations, this report focuses on the INS/GPS system for the UXO detection applications. Specifically, the filters/smoother methods of the INS/GPS system are studied for the precise position of the INS/GPS system.

CHAPTER 3: NONLINEAR ESTIMATION

The dynamic equations for the inertial system errors are a set of differential equations which model the system error behavior with time (Jekeli, 2000). The system states represent the dynamic equations' variables such as position, velocity, orientation errors and IMU's errors which describe the physical state of the system. These systems states are estimated at any time with or without external information (observations of the system). Since the general theory of estimation is fully covered in many literatures (e.g., Gelb, 1974; Maybeck, 1979; Brown and Hwang, 1992), the estimation methods for precise INS/GPS will be presented in this chapter. The estimation is based on the Bayesian approach because it is the suitable approach for the probabilistic formulation. Also the Bayesian method provides an easy framework to develop a consistent and practical application for least-squares approximation or maximum likelihood estimation (Sakka, 2008). Usually, the estimation can be specialized into three extreme problems: filtering, prediction, and smoothing (Jekeli, 2000; van der Merwe et al., 2000). Filtering is the problem of estimating the state of a system based on available measurements up to this time. Prediction is the estimation of states based on the state equations after the last available observation. Smoothing consists in estimating states, based on all available observations before and after a specific time.

There are various possible filtering approaches for INS/GPS integration that have been proposed over the last few decades, such as the wave estimator (Salychev and Schaffrin, 1992; Salychev, 1999), the (Extended) Kalman filter (Anderson and Moore, 1979; Haykin, 2001), the unscented Kalman filter (Julier and Uhlmann ,1996), the particle filter (Gordon et al., 1993; Doucet et al., 2001), various adaptive filters (Schwarz, 1999; Hide et al., 2004), and methods of artificial intelligence (Chiang, 2004; Wang et al., 2006). Some of the more recent nonlinear filters, mostly investigated for navigation of ground vehicles or aircraft, are studied in this chapter with particular application to high precision geolocation required for MEC characterization. Indeed, the nonlinear filtering methods may be even more applicable to the dynamics associated with UXO detection platforms that must traverse rough terrain and experience frequent changes in heading, which is a significantly different environment than encountered in typical navigation and positioning applications. Finally, these nonlinear filtering methods are applied to the smoothing method as post-processing technique.

3.1. Bayesian Estimation

To estimate the optimal state of the dynamic system, the system and measurement equations are required, as well as an initial condition. The system model defines the propagation of error states with time and the measurement model updates the error states with noisy measurements. Let a fairly general nonlinear system model be described by

system and measurement equations as follows:

$$x_{k+1} = f_k(x_k, w_{k+1}) \tag{3.1}$$
$$y_k = h_k(x_k, v_k) \tag{3.2}$$

where x_k is the state vector at time step k, w_k is the process noise vector, y_k is the measurement vector, and v_k is the measurement noise vector. The functions $f_k(\cdot)$ and $h_k(\cdot)$ are time-varying nonlinear vector function that define system and measurement equations. The noise sequences are assumed to be independent and white with or without known density function.
If the process and measurement noises are assumed to be additive, the above general nonlinear model can be written as

$$x_{k+1} = f_k(x_k) + w_{k+1} \tag{3.3}$$
$$y_k = h_k(x_k) + v_k \tag{3.4}$$

The Bayesian approach considers all quantities as random variables that could be described by a probability density function. Therefore, the primary goal of Bayesian filtering is to estimate the posterior density function of the states based on all available observations and previous state estimates,

$$p(x_k \mid y_{1:k}) \tag{3.5}$$

The dynamic system equations of the state provide the conditional transition density of the current state, $p(x_k \mid x_{k-1}, y_{1:k-1})$ based on the previous state and all previous available observations. The measurement equation specifies the likelihood function of the current observations given the current states, $p(y_k \mid x_k)$.

Forward Prediction: If the previous posterior density function $p(x_{k-1} \mid y_{1:k-1})$ exists; the prior density function $p(x_k \mid y_{1:k-1})$ of the state x_k can be obtained based on the Chapman-Kolmogorov equation,

$$p(x_k \mid y_{1:k-1}) = \int p(x_k \mid x_{k-1}, y_{1:k-1}) \cdot p(x_{k-1} \mid y_{1:k-1}) dx_{k-1} \tag{3.6}$$

Forward Update: Following Bayes' Theory the posterior density function $p(x_k \mid y_{1:k})$ will be proportional to the product of the likelihood function and the prior density distribution,

$$p(x_k \mid y_{1:k}) = \frac{p(y_k \mid x_k) \cdot p(x_k \mid y_{1:k-1})}{\int p(y_k \mid x_k) p(x_k \mid y_{1:k-1}) dx_k} \tag{3.7}$$

where $p(y_k \mid x_k)$ is the likelihood function and $\int p(y_k \mid x_k)p(x_k \mid y_{1:k-1})dx_k$ is usually considered as a normalization constant.
These integrals can be solved in analytic form if the dynamic and measurement models are linear and Gaussian. The solution is then also Gaussian and commonly calculated by the Kalman Filter equations. If the models are non-linear but still Gaussian, the solution is approximated with Gaussians by using the Extended Kalman Filter or the Unscented Kalman Filter. In case of nonlinear and non-Gaussian models, particle filtering is an effective estimation method.
For the smoothed state estimation, given all available measurements, the following marginal posterior distribution is computed

$$p(x_k \mid y_{1:T}) \qquad \text{with T > k.} \tag{3.8}$$

This Bayesian estimation is used for the formulation of the filters/smoothers in this study. Every filter employed the general nonlinear model in equation (3.3) and the measurement model in equation (3.4). Also, the goal of each filter is to estimate the posterior density function of the states (3.5).

3.2 Filtering Methods

3.2.1 Extended Kalman Filter (EKF)

The (discrete) Kalman filter is the recursive estimation of the system states as time progresses on the basis of external observations (Kalman, 1960). It provides a closed form of the solution (analytic solution) for the filtering problem where the system and measurement models are linear. In general, the Kalman filter does not per se assume any distribution. Only in a Bayesian setting, the posterior density should be Gaussian, in which case the two parameters (mean and covariance) can characterize the posterior density in equation (3.5) completely.
The full and formal derivation of the Kalman Filter is well written in several articles (Kalman, 1960; Maybeck 1979; Brown and Hwang, 1992; Welch and Bishop, 2001; Haykin, 2001). Here only a summary of the Kalman filter is presented:
Let the linear dynamics of the system be modeled according to

$$x_k = F(t_k, t_{k-1})x_{k-1} + G_k w_k \tag{3.9}$$

where x_k is the $(m \times 1)$ state variable vector with the Markov process. The Markovian property means that x_k given x_{k-1} is independent from any states in the past and can be formulated in probabilistic terms

$$p(x_k \mid x_{k-1}, x_{k-2}, \ldots, x_k) = p(x_k \mid x_{k-1}) \tag{3.10}$$

$F(t_k, t_{k-1})$ is the state transition matrix that especially transforms the states from time *k*-1

to *k*. The system is assumed to be driven or excited by a random component $G_k w_k$, where G_k $(m \times l)$ is a constant over the interval $\Delta t = t_k - t_{k-1}$ and w_k $(l \times 1)$ is a Gaussian, zero-mean, white noise process vector with a given covariance matrix at the time t_k, defined by (Brown and Hwang, 1992, p.219)

$$E\left[w_j w_k^T\right] = \begin{cases} Q_k & \text{for j = k} \\ 0 & \text{for j} \neq \text{k} \end{cases} \tag{3.11}$$

The observations are linearly related to the state variables through the measurement matrix H_k $(n \times m)$

$$y_k = H_k x_k + v_k \tag{3.12}$$

where v_k is the measurement noise in the form of a Gaussian vector of a zero-mean, white noise processes and with a covariance matrix defined by

$$E\left[v_j v_k^T\right] = \begin{cases} R_k & \text{for j = k} \\ 0 & \text{for j} \neq \text{k} \end{cases} \tag{3.13}$$

Furthermore, the process noise is uncorrelated with the measurement noise at all epochs. The parameters of the Gaussian distribution (mean and covariance of the states) of the Kalman filter can be computed with the prediction and update steps. In the prediction step of the Kalman filter, the state estimate and its covariance propagate according to:

$$\hat{x}_k^- = F(t_k, t_{k-1})\hat{x}_{k-1}, \tag{3.14}$$

$$P_k^- = F(t_k, t_{k-1})P_{k-1}F^T(t_k, t_{k-1}) + G_k Q_k G_k^T, \tag{3.15}$$

where $\hat{x}_{k-1}$ is the estimated state vector at time k-1, $\hat{x}_k^-$ is the so-called predicted state vector for the next epoch, P_{k-1} is the state covariance matrix of $\left(\hat{x}_{k-1} - x_{k-1}\right)$ at time k-1, and P_k^- is the state covariance matrix of $\left(\hat{x}_k^- - x_k + G_k w_k\right)$.
The measurement update of the Kalman Filter is

$$\hat{x}_k = \hat{x}_k^- + K_k\left(y_k - H_k \hat{x}_k^-\right), \tag{3.16}$$

$$P_k = \left(I - K_k H_k\right)P_k^-\left(I - K_k H_k\right)^T + K_k R_k K_k^T, \tag{3.17}$$

where the Kalman gain matrix K_k which uses the weighted difference between measurements and predictions ("innovations") to update the system dynamics model solution, if it is given by

$$K_k = P_k^- H_k^T \left(H_k P_k^- H_k^T + R_k \right)^{-1} \tag{3.18}$$

The innovation vector in equation (3.16) can be defined as

$$\upsilon_k = y_k - H_k \hat{x}_k^- \tag{3.19}$$

In actuality, the system and observation models of the inertial navigation system are nonlinear and the Kalman filter should be "extended" using linearized models. Thus, the Taylor series expansion of the nonlinear functions $f(\cdot)$ and $h(\cdot)$ around the state estimates $\hat{x}_{k-1}$ is required (Anderson and Moore, 1979). These equations use only the first term of linearized equations based on the assumption that the errors are small enough to be represented by differential perturbations of the navigation equation. The second or higher order terms of the taylorized equations, are neglected. Thus, if the system errors grow too large, the linear perturbation development may no longer yield an adequate model, thus requiring iteration with new approximations. For example, let the Taylor series be

$$f(x_k) = f(\hat{x}_{k-1}) + \left. \frac{\partial f(x_k)}{\partial x_k} \right|_{x_t = \hat{x}_{k-1}} (x_k - \hat{x}_{k-1}) + \cdots \tag{3.20}$$

Using only the linear expansion terms, it is easy to derive the precise update equations, for the mean and covariance of the Gaussian approximation to the posterior distribution of the states, where

$$F_k \cong \left. \frac{\partial f(x_k)}{\partial x_k} \right|_{x_t = \hat{x}_{k-1}} \text{ and } \; H_k \cong \left. \frac{\partial h(x_k)}{\partial x_k} \right|_{x_t = \hat{x}_{k-1}} \tag{3.21}$$

are the Jacobians of the process model and the measurement model respectively respectively, but where their randomness is also supposed.
Since a higher-order EKF has a limited usage because of its complexity and little improvement (Nassar, 2003), the EKF which uses only the first term in a Taylor expansion of the non-linear function was employed through without iteration.

3.2.2 Unscented Kalman Filter (UKF)

The UKF is a recursive application of the unscented transformation (UT) of state variables through the nonlinear state dynamics model (Julier and Uhlmann, 1996). This also results in a Gaussian approximation to the posteriori density function, $p(x_k \mid y_1, \ldots, y_k)$. The unscented Kalman filter is different from the EKF in that it propagates various sample states – not just the "predicted state" - directly to approximate the mean and its covariance for the posteriori density function in equation (3.5) through the nonlinear models without the linearization (Julier et al., 1995). Thus, it avoids the

formulation and computation of derivatives of the system model. Because the EKF only uses the first-order terms of the Taylor series expansion of the nonlinear functions, it often introduces large errors in the estimated statistics of the posterior distributions of the states, especially when the models are highly nonlinear and the local linearity assumption breaks down, i.e., the effects of the higher order terms of the Taylor series expansion become significant.

The unscented transformation (UT) propagates a suitably chosen set of sample points (so-called sigma points) in the state space through the (nonlinear) system dynamics such that they accurately capture the transformed mean and covariance matrix of the state vector. It is noted that although the UT resembles Monte Carlo Simulation (section 3.3) it is different because the UT selects the sigma points deterministically (Julier et al., 2000). The general scaled version of the UT is summarized here (Julier et al., 2000; Wan and van der Merwe, 2001).

For the n_x dimensional random variable x with mean $\bar{x}$, and covariance P_x, $2n_x+1$ sigma points, $S_i = \{W_i, \chi_i\}$, are generated as follows

$$\begin{aligned}
\chi_0 &= \bar{x} \\
\chi_i &= \bar{x} + \alpha\left(\sqrt{(n_x+\kappa)P_x}\right)_i \quad , \quad i = 1,...,n_x \\
\chi_i &= \bar{x} - \alpha\left(\sqrt{(n_x+\kappa)P_x}\right)_{i-L} , \quad i = n_x+1,...,2n_x
\end{aligned} \tag{3.22}$$

where α and κ are scaling parameters and $\left(\sqrt{(n_x+\kappa)P_x}\right)_i$ is the i^{th} row or column of the matrix square root of $\sqrt{(n_x+\kappa)P_x}$. Given a nonlinear function, $g(x)$, it can be shown that the following weighted combinations of $y_i = g(\chi_i)$ $i = 0,\ldots,2n_x$ estimate the first two statistical moments (mean and covariance) of g very well at least up to second order in the non-linearities:

$$\bar{y} = \sum_{i=0}^{2n_c} W_i^{(m)} y_i \,, \tag{3.23}$$

$$P_y = \sum_{i=0}^{2n_c} W_i^{(c)} \left(y_i - \bar{y}\right)\left(y_i - \bar{y}\right)^T \tag{3.24}$$

with weights given by

$$W_0^{(m)} = 1 - \frac{n_x}{\alpha^2 (n_x + \kappa)},$$

$$W_0^{(c)} = 1 - \frac{n_x}{\alpha^2 (n_x + \kappa)} + (1 - \alpha^2 + \beta) \qquad (3.25)$$

$$W_i^{(m)} = W_i^{(c)} = \frac{1}{2\alpha^2 (n_x + \kappa)}, \quad i = 1, \ldots, 2n_x$$

The weights for the mean sum up to unity, while for the covariance they sum up to $\left(1 - \alpha^2 + \beta\right)$. The scaling parameter, α $\left(10^{-4} \le \alpha \le 1\right)$, controls the spread of the sigma points around $\bar{x}$ and serves to maintain the positive semi-definiteness of the covariance (van der Merwe et al., 2000). For Gaussian state vectors, *x*, the estimation of the mean and covariance of $g(x)$ is accurate up to third order. The parameter β is used to increase the accuracy of the higher-order moments ($\beta = 2$ is optimal for Gaussian variables) (Julier et al., 1995).

In comparison, the EKF only calculates the posterior mean and covariance accurately to the first order, and all high order terms are simply truncated (For a more detailed proof, see Julier and Uhlmann, 1996).

The UKF proceeds with the usual two-step, prediction and measurement update formalism, but the mean and covariance are determined using all the sigma points. The following Table 3.1 summarizes the prediction and measurement steps of the UKF.

Initialize with

$$\bar{x}_0 = E[x_0], \;\; P_0 = E\left[(x_0 - \bar{x}_0)(x_0 - \bar{x}_0)^T\right]$$

The sigma points are calculated and the time update equations are

$$\chi_{k-1} = \left[\bar{x}_{k-1} \quad \bar{x}_{k-1} \pm \alpha\sqrt{(n_x + \kappa)P_{k-1}}\right]$$

$$\chi_k^- = f(\chi_{k-1})$$

$$\hat{x}_k^- = \sum_{i=0}^{2n_x} W_i^{(m)} \chi_{i,k}^-$$

$$P_k^- = \sum_{i=0}^{2n_x} W_i^{(c)} \left(\chi_{i,k}^- - \hat{x}_k^-\right)\left(\chi_{i,k}^- - \hat{x}_k^-\right)^T + Q$$

The measurement update equations are

$$\mathrm{Y}_k^- = h\left(\chi_k^-\right)$$

$$\hat{y}_k^- = \sum_{i=0}^{2n_x} W_i^{(m)} \mathrm{Y}_{i,k}^-$$

$$P_{\tilde{y}_k\tilde{y}_k} = \sum_{i=0}^{2n_x} W_i^{(c)} \left(Y_{i,k}^- - \hat{y}_k^-\right)\left(Y_{i,k}^- - \hat{y}_k^-\right)^T + R$$

$$P_{x_k y_k} = \sum_{i=0}^{2n_x} W_i^{(c)} \left(\chi_{i,k}^- - \hat{x}_k^-\right)\left(Y_{i,k}^- - \hat{y}_k^-\right)^T$$

The state and covariance update is performed in the same way as for the Kalman filter equations (3.16) ~ (3.18).

$$\hat{x}_k = \hat{x}_k^- + \kappa_k\left(y_k - \hat{y}_k^-\right)$$

$$P_k = P_k^- - \kappa_k P_{\tilde{y}_k\tilde{y}_k} \kappa_k^T$$

$$\kappa_k = P_{x_k y_k} P_{\tilde{y}_k\tilde{y}_k}^{-1}$$

Table 3.1. Unscented Kalman Filter (zero-mean) noise case.

Since there is no explicit calculation of any Jacobians or Hessians necessary to implement this algorithm, the UKF requires the computation of a matrix square root which can be implemented directly using a Cholesky factorization in order $n_x^3 / 6$ operations.
However, the covariance matrices can be expressed recursively, and thus the square-root can be computed in order n_x^2 by performing a recursive version of the Cholesky factorization. So, not only does the UKF outperform the EKF in accuracy, it does not require any additional computational costs.

3.2.3 Unscented Particle Filter (UPF)

The particle filter which has been introduced by Gordon et al. (1993) fifteen years ago became one of the most popular numerical methods to solve nonlinear (and non-Gaussian) estimation problems with the advent of modern computational capabilities (Doucet, 2008). The particle filter can represent the state distribution by using sequential importance sampling and resampling, and does not need any Gaussian approximation compared to the two aforementioned nonlinear filtering strategies (EKF and UKF). In theory, any system model can be handled to a desired accuracy using a sufficient number of particles, but practically it is limited by a given computational resource (Sarkka, 2006). In this section, the UKF is used to improve the generic particle filter. Before presenting the particle filtering algorithms, the fundamental background for the particle filter, usually the perfect Monte Carlo simulation, (sequential) importance sampling and resampling will be reviewed briefly.

Perfect Monte Carlo Simulation and Sequential importance sampling: The particle filter is built upon the Monte Carlo simulation with sequential importance sampling (SIS) (Haykin, 1999). The goal is to estimate the posterior density function, $p(x_{0:k} \mid y_{1:k})$, with expectations recursively

$$E(g_k(x_{0:k})) = \int g_k(x_{0:k}) p(x_{0:k} \mid y_{1:k}) dx_{0:k} \tag{3.26}$$

where g_k is some arbitrary function to be specified.

Let $x_{0:k}$ be the unknown, x, let $y_{1:k}$ be the available data (measurements in the filter), y, and let $dx_{0:k}$ be dx, then the equation (3.26) can be simplified as

$$E(g(x)) = \int g(x) p(x \mid y) dx \tag{3.27}$$

We simulate the number of samples $x^{(i)}, i = 1, \cdots, N$ (N is the total number of samples) from $p(x \mid y)$. The relative frequency of samples corresponds to the area of the pdf near a particular value x, say x_j, $j = 1, \ldots, J$ (J is the total number of discrete intervals). Let $N_j = N \cdot p(x_j \mid y) dx$, where dx is the length of the interval near x_j and $p(x_j \mid y)$ is the density value (Figure 3.1). Then the samples for x_j are given by N_j values from an Uniform random generation in the interval $[\, x_j - dx/2, x_j + dx/2 \,]$. Finally, we can replace the integral in equation (3.27) into the simple sum of samples.

$$\overline{E(g(x))} \approx \frac{1}{N} \sum_{j=1}^{J} \sum_{i=1}^{N_j} g(x_j^{(i)}) N_j \tag{3.28}$$

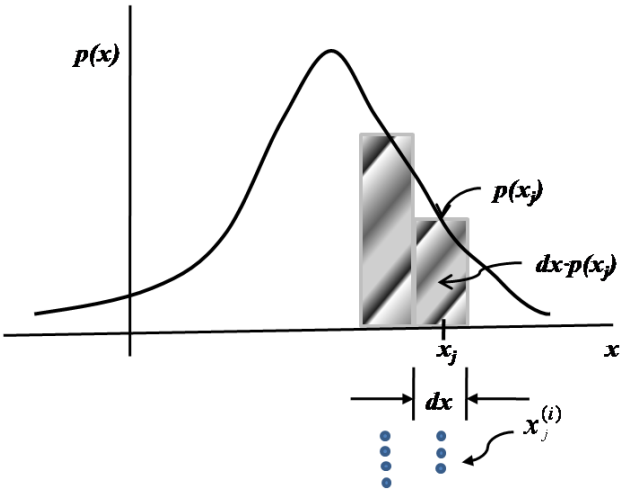

Figure 3.1. The basic idea of the Monte Carlo integration using the discrete sum of samples, $x_j^{(i)}$.

Therefore, any (given) expectations of the integrals (3.26) can be approximated by the tractable sum of particles

$$\overline{E\left(g_k\left(x_{0:k}\right)\right)} \approx \frac{1}{N}\sum_{j=1}^{J}\sum_{i=1}^{N_j} g_k\left(x_{0:k,j}^{(i)}\right)N_j \tag{3.29}$$

As N goes to infinity, one can say $\overline{E\left(g_k\left(x_{0:k}\right)\right)} \xrightarrow[N\to\infty]{a.s.} E\left(g_k\left(x_{0:k}\right)\right)$, where $\xrightarrow[N\to\infty]{a.s.}$ denotes almost surely convergence. The convergence of Monte Carlo approximation is based on the Central Limit Theorem (CLT) (Liu and Chen, 1998). Since it is impossible to directly draw samples from the posterior density function, the proposal distribution $q\left(x_{0:k} \mid y_{1:k}\right)$ should be substituted in equation (3.26) (van der Merwe et al., 2000)

$$\begin{aligned} E\left(g_k\left(x_{0:k}\right)\right) &= \int g_k\left(x_{0:k}\right)p\left(x_{0:k} \mid y_{1:k}\right)dx_{0:k} \\ &= \int g_k\left(x_{0:k}\right)\frac{p\left(x_{0:k} \mid y_{1:k}\right)}{q\left(x_{0:k} \mid y_{1:k}\right)}q\left(x_{0:k} \mid y_{1:k}\right)dx_{0:k} \\ &= \int g_k\left(x_{0:k}\right)\frac{p\left(y_{1:k} \mid x_{0:k}\right)p\left(x_{0:k}\right)}{p\left(y_{1:k}\right)q\left(x_{0:k} \mid y_{1:k}\right)}q\left(x_{0:k} \mid y_{1:k}\right)dx_{0:k} \\ &= \int g_k\left(x_{0:k}\right)\underbrace{\frac{p\left(y_{1:k} \mid x_{0:k}\right)p\left(x_{0:k}\right)}{q\left(x_{0:k} \mid y_{1:k}\right)}}_{\text{unnormalized importance weight}}\frac{1}{p\left(y_{1:k}\right)}q\left(x_{0:k} \mid y_{1:k}\right)dx_{0:k} \end{aligned} \tag{3.30}$$

The unnormalized importance weights are

$$\omega_k = \frac{p(y_{1:k} \mid x_{0:k})p(x_{0:k})}{q(x_{0:k} \mid y_{1:k})} \tag{3.31}$$

The importance weight ω_k is a measure of the skewness of $q(x_{0:k} \mid y_{1:k})$ relative to $p(x_{0:k} \mid y_{1:k})$ (Nordlund, 2002). The unknown normalizing density $p(y_{1:k})$ is eliminated as follows.

$$\begin{aligned} E(g_k(x_{0:k})) &= \frac{1}{p(y_{1:k})} \int g_k(x_{0:k})\omega_k(x_{0:k})q(x_{0:k} \mid y_{1:k})dx_{0:k} \\ &= \frac{\int g_k(x_{0:k})\omega_k(x_{0:k})q(x_{0:k} \mid y_{1:k})dx_{0:k}}{\int p(y_{1:k} \mid x_{0:k})p(x_{0:k})\frac{q(x_{0:k} \mid y_{1:k})}{q(x_{0:k} \mid y_{1:k})}dx_{0:k}} \\ &= \frac{\int g_k(x_{0:k})\omega_k(x_{0:k})q(x_{0:k} \mid y_{1:k})dx_{0:k}}{\int \omega_k(x_{0:k})q(x_{0:k} \mid y_{1:k})dx_{0:k}} \\ &= \frac{E_{q(\cdot \mid y_{1:k})}(\omega_k(x_{0:k})g_k(x_{0:k}))}{E_{q(\cdot \mid y_{1:k})}(\omega_k(x_{0:k}))} \end{aligned} \tag{3.32}$$

where $E_{q(\cdot \mid y_{1:k})}$ has been used to emphasize the expectations are taken over the proposal distribution $q(\cdot \mid y_{1:t})$. Thus, we can approximate the expectations of interest by drawing samples from proposal distribution $q(\cdot \mid y_{1:k})$.

$$\begin{aligned} \overline{E(g_k(x_{0:k}))} &= \frac{\frac{1}{N}\sum_{i=1}^{N} \omega_k(x_{0:k}^{(i)})g_k(x_{0:k}^{(i)})}{\frac{1}{N}\sum_{i=1}^{N} \omega_k(x_{0:k}^{(i)})} \\ &= \sum_{i=1}^{N} \tilde{\omega}_k(x_{0:k}^{(i)})g_k(x_{0:k}^{(i)}) \end{aligned} \tag{3.33}$$

where the normalized importance weights are

$$\tilde{\omega}_k(x_{0:k}^{(i)}) = \frac{\omega_k(x_{0:k}^{(i)})}{\sum_{i=1}^{N} \omega_k(x_{0:k}^{(i)})} \tag{3.34}$$

Sequential importance sampling (SIS) is a sequential version of importance sampling (Doucet et al., 2001). In order to compute the sequential importance weights, the proposal distribution is expanded as

$$q(x_{0:k} \mid y_{1:k}) = q(x_{0:k-1} \mid y_{1:k-1}) q(x_k \mid x_{0:k-1}, y_{1:k}) \tag{3.35}$$

with the assumption that the current state is independent of future observations (not smoothing). Since the states follow the Markov property and the observations are conditionally independent given the states, we have

$$p(x_{0:k}) = p(x_0) \prod_{j=1}^{k} p(x_j \mid x_{j-1}) \quad \text{and} \quad p(y_{1:k} \mid x_{0:k}) = \prod_{j=1}^{k} p(y_j \mid x_j) \tag{3.36}$$

By substituting equation (3.35) into equation (3.31) and using (3.36), a recursive estimate for the importance weights, given an approximate choice of proposal distribution, $q(x_k \mid x_{0:k-1}, y_{1:k})$ can be derived as follows

$$\begin{aligned}
\omega_k &= \frac{p(y_{1:k} \mid x_{0:k}) p(x_{0:k})}{q(x_{0:k-1} \mid y_{1:k-1}) q(x_k \mid x_{0:k-1}, y_{1:k})} \\
&= \underbrace{\frac{p(y_{1:k-1} \mid x_{0:k-1}) p(x_{0:k-1})}{q(x_{0:k-1} \mid y_{1:k-1})}}_{=\omega_{k-1},\, see\, Eq.(3.30)} \frac{p(y_{1:k} \mid x_{0:k}) p(x_{0:k})}{p(y_{1:k-1} \mid x_{0:k-1}) p(x_{0:k-1})} \frac{1}{q(x_k \mid x_{0:k-1}, y_{1:k})} \\
&= \omega_{k-1} \frac{p(y_{1:k} \mid x_{0:k}) p(x_{0:k})}{p(y_{1:k-1} \mid x_{0:k-1}) p(x_{0:k-1})} \frac{1}{q(x_k \mid x_{0:k-1}, y_{1:k})} \\
&= \omega_{k-1} \frac{p(y_k \mid x_k) p(x_k \mid x_{k-1})}{q(x_k \mid x_{0:k-1}, y_{1:k})}
\end{aligned} \tag{3.37}$$

One of the most critical issues in importance sampling is the choice of the proposal distribution. Generally, the transition prior, $p(x_k \mid x_{k-1})$ is chosen as ($\doteq$) proposal function (Avitzour, 1995; Beadle and Djuric, 1997; Gorden et al., 1993; Kitagawa, 1996)

$$q(x_k \mid x_{0:k-1}, y_{1:k}) \doteq p(x_k \mid x_{k-1}) \tag{3.38}$$

It shows higher Monte Carlo variation than the optimal proposal distribution $p(x_k \mid x_{0:k-1}, y_{1:k})$ but it is usually easier to implement (Doucet, 1999, Liu and Chen, 1998). For example, if an additive Gaussian process noise model is employed, the transition prior is

$$p(x_k \mid x_{k-1}) = N(f(x_{k-1}), Q_{k-1}) \tag{3.39}$$

where $f(x_{k-1}) = f(x_{k-1}, 0)$ from equation (3.1).
If the proposal distribution is not sufficiently close to the actual posterior distribution, this approximation is not effective and only a few particles will have significant importance weights when their likelihood is evaluated (van der Merwe et al., 2000; Doucet et al., 2001, Arulampalam et al., 2001). Therefore, to move the particles close to the measurement (Figure 3.2), the EKF or UKF has been used before applying particle filter steps (Haykin, 2001).

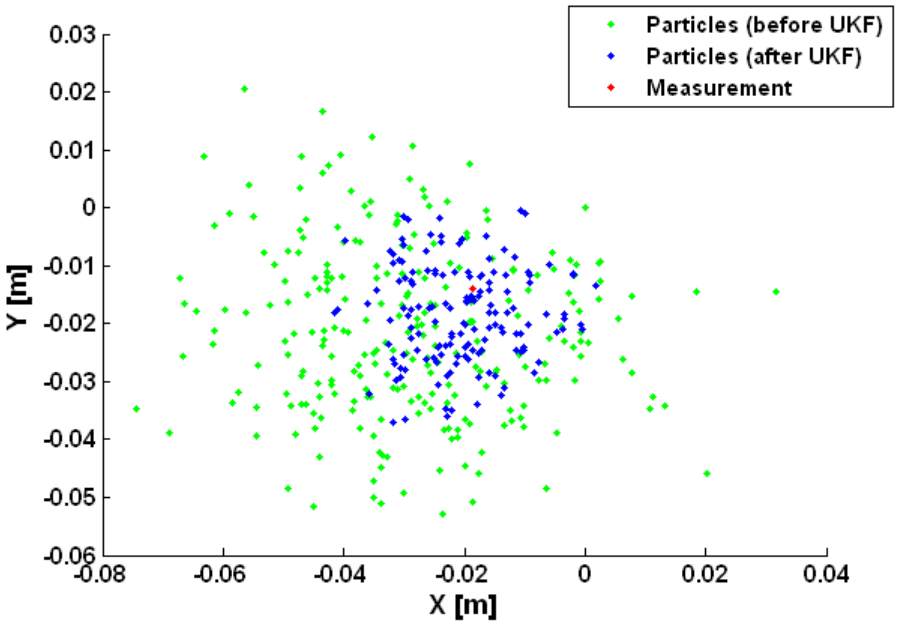

Figure 3.2. The UKF moves the samples (particles) close to the measurement (The Position of Measurement is X: -0.19m, Y: -0.11m).

Resampling: The SIS is limited in that the variance of the importance weights increases stochastically over time (known as Degeneracy of the SIS algorithm, for details see Kong et al., 1994; Doucet, 1999). To avoid Degeneracy of the SIS algorithm, a resampling method is used to eliminate samples which have low importance weights and to multiply samples with high importance weights (i.e., the number of high importance weights are increased). A resampling scheme associates to each particle $x_{0:t}^{(i)}$ a number of "children", say $n_i < N$, such that $\sum_{i=1}^{N} n_i = N$. Several resampling schemes have been proposed such as sampling importance resampling (SIR) (Efron, 1982; Rubin, 1988; Smith and Gelfaud, 1992), residual resampling (Mackay, 1992; Higuchi, 1997) and minimum variance sampling (Doucet, 2000).
The adaptive sampling which is used in this report estimates the effective number of particles from the variance of the particle weights (Liu and Chen, 1998). The estimate

of the effective number of particles is

$$n_{eff} \approx \frac{1}{\sum_{i=1}^{N} \left(\omega_k^{(i)}\right)^2} \tag{3.40}$$

where $\omega_k^{(i)}$ is the normalized weight of particle *i* at the time *k*. Thus, the resampling is performed when the effective number of particles is less than the total number of particles (pre-defined by the filter designer). For the simulation, $n_{eff} < N/10$ (N is the number of particle) is used.

Particle filtering: The object of the particle filter is to determine the probability density $p(x_t \mid y_{1:k})$ of the state at time, t_k, conditioned on the measurements up to that time, according to Bayes' Rule (Simon, 2006)

$$p(x_t \mid y_{1:k}) = \frac{p(y_k \mid x_k) p(x_k \mid y_{1:k-1})}{p(y_k \mid y_{1:k-1})} \tag{3.41}$$

where the conditional density, $p(y_k \mid x_k)$, is presumed known (for example, but not necessarily Gaussian), and the other conditional densities on the right side can, in principle, be determined from the previous steps in the recursive algorithm.

In practice, the particle filter starts with the randomly generated particles, $x_{0,i}$ $i = 1,\ldots,N$ using their a priori mean and covariance, and propagates them through the equation:

$$x_{k,i} = f(x_{k-1,i}) + G_k w_{k,i} \tag{3.42}$$

where $w_{k,i}$ is the noise realized according to its pre-defined pdf.

The generic PF algorithm could be summarized in four main steps: First, as an initialization step, generate *N* samples x_0^i, $i = 1,\ldots,N$ from the prior distribution (initial distribution) $p(x_0)$ at $k = 0$ and initialize the importance weights $\omega_0^{(i)} = 1/N$, $i = 1,\ldots,N$.

Second, for $k = 1,2,\ldots$, sample $x_k^i \sim q(x_k \mid x_{0:k-1}^i, y_{1:k})$ where $i = 1,\ldots,N$ and compute the importance weight (Equation 3.31)

$$\omega_k^i = \omega_{k-1}^i \frac{p(y_k \mid x_k^i) p(x_k^i \mid x_{k-1}^i)}{q(x_k^i \mid x_{0:k-1}^i, y_{1:k})} \tag{3.43}$$

then normalize the importance weights

$$\tilde{\omega}_k^i = \omega_{k-1}^i \left(\sum_{j=1}^{N} \omega_k^j \right)^{-1} \tag{3.44}$$

Third, if the effective sample size is less than a threshold ($n_{eff} < N$, N is the pre-defined threshold), a selection step (resampling) is performed. In case of resampling, re-generate a new set of samples, x_k^i, $i = 1,\ldots,N$, by multiplying samples x_k^i with importance weights $\tilde{\omega}_k^i$, respectively. If the particles have high importance weights, the number of that particle is increased according to its weight. Otherwise, the particles that have small importance weights will be eliminated. At the end, we have the same number of particles and then set $\omega_k^i = \tilde{\omega}_k^i = (N)^{-1}$ for $i = 1,...,N$.
Fourth, the minimum mean square (MMS) estimate of x_k and its covariance are estimated according to

$$\hat{x}_k = E[x_k] \approx \sum_{i=1}^{N} \tilde{\omega}_k^{(i)} \cdot x_k^i \tag{3.45}$$

$$P_k = E\left[(x_k - \hat{x}_k)^2 \right] \approx \sum_{i=1}^{N} \tilde{\omega}_k^i \left(x_k^i - \hat{x}_k \right)\left(x_k^i - \hat{x}_k \right)^T \tag{3.46}$$

Unscented Particle Filter: Van der Merwe et al. (2000) combined the PF with other filters such as UKF in order to refine the initially generated particles, and called it the unscented particle filter (UPF). Each randomly generated initial particle is propagated and updated by using the UKF (where the sigma points are computed relative to each particle). Then, the likelihood values are determined using these a posteriori particles and the measurement pdf, as before, followed by the re-sampling procedure (Haykin, 2001; Simon, 2006). This approach can yield a better approximation for the conditional pdf of the states and has yielded improved accuracy for various positioning-related applications (Arulampalam et al., 2001; Grewal and Andrews, 2001; van der Merwe et al., 2000).
The importance sampling step of the generic particle filter is replaced with the following UKF prediction and update steps and all other steps are same as for the particle filter. For $i = 1,\ldots,N$, each particle is updated using the UKF. First, initialize each particles and then sigma points are calculated as follows

$$\bar{x}_0^{(i)} = E\left[\; x_0^{(i)} \; \right], \quad P_0^{(i)} = E\left[\; \left(x_0^{(i)} - \bar{x}_0^{(i)} \right)\left(x_0^{(i)} - \bar{x}_0^{(i)} \right)^T \; \right] \tag{3.47}$$

$$\chi_{k-1}^{(i)} = \left[\; \bar{x}_{k-1}^{(i)} \quad \bar{x}_{k-1}^{(i)} \pm \alpha \sqrt{(n_x + \kappa) P_{k-1}^{(i)}} \; \right], \; P_{k-1}^{(i)} = E\left[\; \left(x_{k-1}^{(i)} - \bar{x}_{k-1}^{(i)} \right)\left(x_{k-1}^{(i)} - \bar{x}_{k-1}^{(i)} \right)^T \; \right] \tag{3.48}$$

Second, the particles are propagated (time update)

$$\chi_{k|}^{-,(i)} = f\left(\chi_{k-1}^{(i)}\right) \tag{3.49}$$

$$\hat{x}_k^{-,(i)} = \sum_{j=0}^{2n_x} W_j^{(m)} \chi_{j,k}^{-,(i)} \tag{3.50}$$

$$P_k^{-,(i)} = \sum_{j=0}^{2n_x} W_j^{(c)} \left(\chi_{j,k}^{-,(i)} - \hat{x}_k^{-,(i)}\right)\left(\chi_{j,k}^{-,(i)} - \hat{x}_k^{-,(i)}\right)^T + Q \tag{3.51}$$

Third, the measurement update with any new observations is

$$\mathrm{Y}_k^{-,(i)} = h\left(\chi_k^{-,(i)}\right) \tag{3.52}$$

$$\hat{y}_{k|}^{-,(i)} = \sum_{j=0}^{2n_x} W_j^{(m)} \mathrm{Y}_{j,k}^{-,(i)} \tag{3.53}$$

$$P_{\tilde{y}_k \tilde{y}_k} = \sum_{j=0}^{2n_x} W_j^{(c)} \left(Y_{j,k}^{-,(i)} - \hat{y}_k^{-,(i)}\right)\left(Y_{j,k}^{-,(i)} - \hat{y}_k^{-,(i)}\right)^T + R \tag{3.54}$$

$$P_{x_k y_k} = \sum_{j=0}^{2n_x} W_j^{(c)} \left(\chi_{j,k}^{-,(i)} - \hat{x}_{k|}^{-,(i)}\right)\left(Y_{j,k}^{-,(i)} - \hat{y}_k^{-,(i)}\right)^T \tag{3.55}$$

Finally, the state and covariance update are performed

$$\hat{x}_k^{(i)} = \hat{x}_k^{-,(i)} + \kappa_k \left(y_k - \hat{y}_k^{-,(i)}\right) \tag{3.56}$$

$$P_k^{(i)} = P_k^{-,(i)} - \kappa_k P_{\tilde{y}_k \tilde{y}_k} \kappa_k^T \tag{3.57}$$

Then one goes to the sampling step, $x_k^{(i)} \sim q\left(x_k^{(i)} \mid x_{0:k-1}^{(i)}, Y_0^k\right)$, which is the second step of the generic particle filter. All other generic particle steps are the same.

3.3 Smoothing

The filtering as described above is a recursive algorithm based on the conditional expectation of the state given all observations and states up to the current time step *k*. In contrast, smoothing does estimate states by using the all available observations. The Rauch-Tung-Striebel (RTS) fixed-interval smoother was applied to the aforementioned forward filters (EKF, UKF, and UPF), yielding the Extended Kalman Smoother (EKS), the Unscented Kalman Smoother (UKS, also called the unscented RTS smoother), and the Unscented Particle Smoother (UPS).

3.3.1 Extended Kalman Smoother (EKS)

From given observations over the interval $0 < k \leq N$ for fixed N, if the forward and backward estimate ($\hat{x}_k^f$ and $\hat{x}_k^b$) and their error covariances (P_k^f and P_k^b) are available, the smoothed estimate, $\hat{x}_k^s$, and its covariance, P_k^s, are obtained. That is, the smoothed estimate is computed by combining the forward Kalman filter estimation and its error covariance up to epoch *k* and the backward filter estimates just after epoch *k* performed

using initial estimates of the state vector and its error covariance at time N.
Since it is assumed that the process noise w_k and measurement noise v_k are independent (Section 3.2.1), we may formulate the error covariance matrix of the a posteriori smoothed estimate as

$$P_k^s = \left[\left[P_k^f\right]^{-1} + \left[P_k^b\right]^{-1}\right]^{-1} \tag{3.58}$$

Using the matrix inversion lemma (Koch, 1987), the equation (3.58) is

$$P_k^s = P_k^f - P_k^f\left[P_k^b + P_k^f\right]^{-1} P_k^f \tag{3.59}$$

The a posteriori smoothed estimate of the state is

$$\hat{x}_k^s = P_k\left(\left[P_k^f\right]^{-1}\hat{x}_k^f + \left[P_k^b\right]^{-1}\hat{x}_k^b\right) \tag{3.60}$$

Using the equation (3.59) and (3.60), after simplifications, we obtain

$$\hat{x}_k^s = \hat{x}_k^f + \left(P_k^s\left[P_k^b\right]^{-1}\hat{x}_k^b - G_k\hat{x}_k^f\right) \tag{3.61}$$

where the smoother gain matrix is

$$G_k = P_k^f\left[P_k^b\right]^{-1}\left[I + P_k^f\left[P_k^b\right]^{-1}\right]^{-1} \tag{3.62}$$

This smoother (three-part smoother) has three components; a forward filter, a backward filter, and a separate smoother which combines results embodied in the forward and backward filters (Haykin, 2001). However, The Rauch-Tung-Striebel (RTS) smoother differs from this smoother in that the measurements are processed by the forward filter and then a separate backward smoothing pass is used to obtain the smoothing solution (Sarkka, 2008). Also, the Rauch-Tung-Striebel smoother is more efficient than the three-part smoother in that a single entity can perform smoothing by incorporating the backward filter and separate smoother (Rauch et al., 1965).
The initial conditions of the smoother for $k = N$ are

$$\hat{x}_N^s = \hat{x}_N^f \quad \text{and} \quad P_N^s = P_N^f \tag{3.63}$$

$\hat{x}_k^f$ is defined from

$$\hat{x}_k^f = \hat{x}_k^{f-} + G_k^f\left(y_k - H_k\hat{x}_k^{f-}\right) \tag{3.64}$$

where

$$G_k^f = P_k^{f-} H_k^T \left[H_k P_k^{f-} H_k + R_k \right]^{-1}, \tag{3.65}$$

$$P_k^{f-} = F(t_k, t_{k-1}) P_{k-1}^f F(t_k, t_{k-1})^T + Q_k \tag{3.66}$$

R_k is the covariance matrix of the measurement noise, and Q_k is the covariance matrix of the system noise.

For $k = N-1, N-2, \ldots$ the time update is defined by

$$\hat{x}_k^s = \hat{x}_k^f + A_k \left(\hat{x}_{k+1}^s - \hat{x}_{k+1}^{f-} \right) \tag{3.67}$$

where A_k is the new gain matrix

$$A_k = P_k^f F(t_{k+1}, t_k)^T \left[P_{k+1}^{f-} \right]^{-1} \tag{3.68}$$

The measurement update of the Rauch-Tung-Striebel smoother yields the covariance of the error of the smoothed estimate (i.e., MSE matrix)

$$P_k^s = P_k^f - A_k \left(P_{k+1}^{f-} - P_{k+1}^s \right) A_k^T \tag{3.69}$$

3.3.2 Unscented Kalman Smoother (UKS)

The Unscented Kalman Smoother is based on the application of the Rauch-Tung-Striebel (RTS) smoothing algorithm to the UKF. Wan and van der Merwe (2001) presented the unscented Kalman smoother which is based on the general two-filter smoothing equations (a linear combination of two filters, which are run in forward and backward directions). Shin (2005) has applied this two-filter based unscented Kalman filter to an INS/GPS system.

The unscented Kalman Smoother is usually based on the combination of forward and backward filters or the RTS-based smoother (Haykin, 2001; Shin, 2005). However, Klass et al. (2006) and Sarkka (2008) showed quite comparable results between the forward and backward filters and the RTS using simple simulations. Therefore, the RTS based smoother was employed and tested hereafter.

A summary of the UKS starts with the propagation of the sigma points through the dynamic model (see Sarkka (2008) for more detailed derivations)

$$\chi_{i,k+1}^- = f\left(\chi_{i,k}^- \right) \quad , \; i = 1, \ldots, 2n+1, \tag{3.70}$$

where $\chi_{i,k}^-$ denotes the sigma point *i*, which corresponds to x_k.

For the next step, compute the predicted mean, the predicted covariance and the cross-covariance

$$\hat{x}_{k+1}^{-} = \sum_i W_{i-1}^{(m)} \chi_{i,k+1}^{-} \tag{3.71}$$

$$P_{k+1}^{-} = \sum_i W_{i-1}^{(c)} \left(\chi_{i,k+1}^{-} - \hat{x}_{k+1}^{-}\right)\left(\chi_{i,k+1}^{-} - \hat{x}_{k+1}^{-}\right)^T \tag{3.72}$$

$$C_{k+1} = \sum_i W_{i-1}^{(c)} \left(Y_{i,k} - \hat{x}_k\right)\left(\chi_{i,k+1}^{-} - \hat{x}_{k+1}^{-}\right)^T \tag{3.73}$$

where the definitions of the weights are the same as for equation (3.25)
Finally, compute the smoother gain, the smoothed mean and the covariance

$$D_k = C_{k+1}\left[P_{k+1}^{-}\right]^{-1} \tag{3.74}$$

$$\hat{x}_k^s = \hat{x}_k + D_k\left[\hat{x}_{k+1}^s - \hat{x}_{k+1}^{-}\right] \tag{3.75}$$

$$P_k^s = P_k + D_k\left[P_{k+1}^s - P_{k+1}^{-}\right]D_k^T . \tag{3.76}$$

This is a recursive procedure. It can be used for calculating the smoothing distribution of step k from the smoothing distribution of time step k+1. The initial conditions for k=N are

$$\hat{x}_N^s = \hat{x}_N \tag{3.77}$$

$$P_N^s = P_N \tag{3.78}$$

3.3.3 Particle Filter Smoothing

In a literature review on particle smoothing or Monte Carlo Smoothing, it is (interestingly) noticed that although particle filter theory and applications are frequently treated, there are only few published papers on particle filter smoothing because the smoothing algorithms such as the two-filter smoother (TFS), the forward-backward smoother (FBS), and a maximum a posteriori (MAP) smoother typically incur high computational costs, namely at the order of $O\left(N^2\right)$, compared to the PF which has costs of the order of $O(N)$ (Klass et al., 2006). In this report, the basic idea of particle smoothing is that the particle filter can provide a smoothed result automatically if the whole history of each particle of states is stored (Kitagawa, 1996; personal communication with Simo Sarkka, 19 June 2009). That is, from the filtered particles of the UPF, each particle is smoothed by using the unscented RTS (see section 3.3.2). From equation (3.75) each smoothed particle can be defined as $\hat{x}_k^{s(i)}$, $i = 1,\ldots,N$ (N is the number of particles) and then is averaged the mean value of the estimate (smoothed estimate) can be found (Kitagawa, 1996; Sarkka, 2008):

$$\hat{x}_{k\,mean}^s \approx \frac{1}{N}\sum_{i=1}^{N} \hat{x}_k^{s(i)} \tag{3.79}$$

3.4 Simulation Study

3.4.1 Test description

In order to assess the integrated IMU/ranging system (e.g., GPS) for precise geolocation of MEC detection and characterization systems, the performance of the three filters and smoothers described above were tested, and the results were compared. The system and environment factors that were considered include the IMU sensor quality, the dynamics of the detector platform (typical for either hand-held or cart-mounted deployment), and the ranging solution quality (concerning precision and environmental degradation as well as longer outages). The analysis addressed how the quality of the IMU sensors influences the aiding capability during short periods of GPS (or other ranging system) loss of signal. Without loss in generality, the loosely coupled INS/GPS integration scheme based on the decentralized filters architecture was employed.

Three accuracy levels of IMU were selected for simulation: the commercial grade (e.g., Crossbow IMU400C), the medium-quality or tactical grade (e.g., Honeywell HG1700), and the commercially available navigation grade (e.g., Litton LN100). While one may think of a possibility to adopt future ultra-high accuracy sensors that are currently being tested in the laboratory (e.g., the cold atom interferometer sensors, as shown in Jekeli, 2004), these devices would only be practically operational (at a reasonable cost) in the more distant future. The essential error parameters of the three IMUs are summarized in Table 3.2.

		Bias	Scale Factor	Random walk
IMU400C	Accelerometer	8.5 mg	1 %	0.05 (m/s)/$\sqrt{hr}$
	Gyroscope	1 deg/s	1 %	0.85 deg/$\sqrt{hr}$
HG1700	Accelerometer	1.0 mg	300 ppm	0.09 (m/s)/$\sqrt{hr}$
	Gyroscope	1 deg/hr	150ppm	0.125 deg/$\sqrt{hr}$
LN100	Accelerometer	20 μg	40 ppm	0.003 (m/s)/$\sqrt{hr}$
	Gyroscope	0.01 deg/hr	1 ppm	0.001 deg/$\sqrt{hr}$

Table 3.2. The specifications of IMUs.

The two levels of ranging precision that were considered are associated with either radar or laser ranging, exemplified by real-time kinematic (RTK), geodetic quality, differential GPS (e.g., Trimble 4700 receiver), and the geodetic total station (e.g., Leica TPS1100 total station). The precision levels are affected by the distance from the detection system to the fixed GPS base station and to the total station, respectively (Clynch, 2001; Grejner-Brzezinska, 2001; Kim et al., 2004).

Table 3.3 lists typical precision levels considered in the simulation analysis. The degradation of the ranging solution system often is expressed in terms of the distance

between the base and rover receivers. For example, if the distance between the base and rover is 10 kilometers, then the horizontal precision of your GPS system by distance is specified as 10mm + 10mm (= 10km $\times$ 10^{-6}) = 20mm (2cm). The vertical accuracy is also obtained as 20mm + 10mm (= 10km $\times$ 10^{-6}) = 30mm (3cm). The primary degradation factor in the ranging solution is signal occlusion, although other factors including tropospheric/ionospheric delays and the geometric configuration of the transmitters affected the signal and solution quality. It is noted that signal outages can occur due to intervening manmade structures or natural objects (e.g., a foliage canopy in case of GPS and rugged terrain in case of the total station). Thus, relatively short-lived outages in the order of several to tens of seconds were assumed. It is worth pointing out that while our analyses addressed primarily the inertial sensor capability to aid the ranging solution in an operational setting, the ranging solution system was also considered as a means to estimate inertial sensor errors.

	Performance (σ_r)
RTK-DGPS	Horizontal: 10mm + d * 10^{-6} Vertical: 20mm + d * 10^{-6}
Total Station	Horizontal & Vertical: 2mm + 2 d * 10^{-6}

Table 3.3. The assumed precision of ranging solutions (*d*: distance between Base and Rover station in unit of km).

Three estimation algorithms were adopted in the simulated test as mentioned above. They were the extended Kalman filter/smoother (EKF / EKS), the unscented Kalman filter/smoother (UKF / UKS), and the unscented particle filter/smoother (UPF / UPS). Every estimation method employed a simplified model for the navigation equations with the assumption that the target system experiences not too large velocities (usually, less than 10m/sec, see Appendix A. for more detail).

The integrated navigation solution was based on the simulated IMU data with periodic updates from the ranging system solution. The time interval between the updates provided a simulation of signal loss periods or solution unavailability for the ranging solution system. Short periods, typical in open survey areas, were as short as the temporal resolution of the ranging system (e.g., one second). On the other hand, longer periods would be experienced in wooded or other obstructed areas (e.g., more than 5 seconds).

The state vector for the IMU/ranging system comprised 21 states: three position (latitude, longitude, and height) errors ($\delta\phi, \delta\lambda, \delta h$, respectively); three velocity errors ($\delta\dot{\phi}, \delta\dot{\lambda}, \delta\dot{h}$, where $\delta\dot{\phi} = \delta v_N / (M + h)$, $\delta\dot{\lambda} = \delta v_E / (N + h)\cos\phi$, M is the radius of curvature in the meridian, and N is the radius of curvature of the ellipsoid in the prime vertical; three

orientation errors in a local north-east-down frame (ψ_N, ψ_E, ψ_D); and, a bias and scale factor error for each of the three accelerometers and three gyros. After the final position solutions are obtained, the coordinates of position are converted from geodetic to Global XYZ coordinate system to compare with control points (The Matlab INSToolkit provide control points on the Global XYZ coordinate system (See Rogers (2000) for the equations of coordinate transformations) as well as relative local XYZ coordinate system). In the case of the UKF and UPF, the position error, velocity error and the four corresponding quaternions were employed instead of the three orientation angle errors since the UT operates best by avoiding the transcendental functions (Kraft, 2003; Shin, 2005).

The system trajectory was created to simulate particular surveying and target characterization patterns. The speed of the sensor system along the trajectory was assumed to be about 1 m/s, and the total length of the trajectory was about 1000 m (Figure 3.3). A similar pattern over a smaller (few square meters) area was created to simulate a local target characterization survey (see Figure 3.3). In this case, the velocity of the sensor was assumed to be about 0.2 m/s and the total length of the trajectory was about 4.2 m.

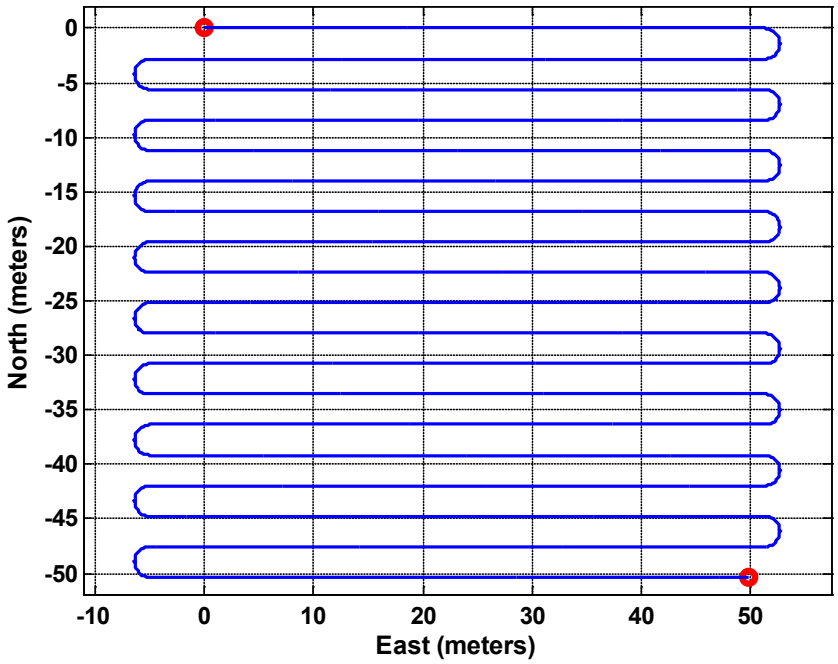

Figure 3.3. The generated control path, total length = 1000m.

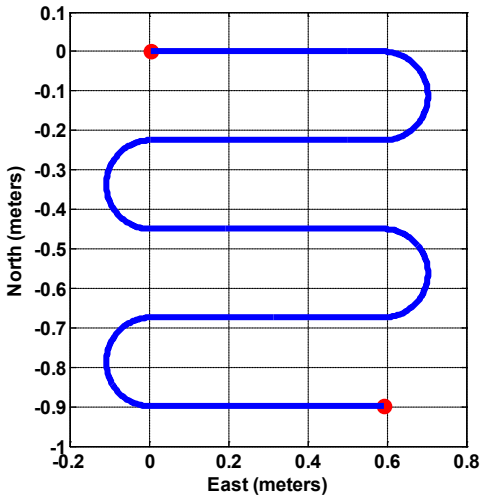

Figure 3.4. Simulated survey pattern for local MEC characterization, total length = 4.2m.

3.4.2 Data Generation

The Matlab INSToolkit® was used as the simulation software for generating raw IMU data. Both the input and output of the computer program are provided in Table 3.4. Only the incremental velocities, Δv (from the simulated accelerometers) and the incremental angles, $\Delta\theta$ (from the simulated gyros) were used for the purpose of creating the GPS and IMU trajectories (Matlab INStoolkit function (*progen*: profile generator) was used to generate the profile of the $\Delta\theta$ and Δv using the initial position, initial velocity, initial direct cosine matrix, and segment information (see Table 3.4 for input parameters for *progen* function)). The initial point (ϕ_0, λ_0, h_0) of GPS and INS trajectory is set as 40°, -83°, and 50m. The GPS trajectory was simply the result of integrating these errorless data according to the navigation equation (see Appendix A. for the navigation equation). The IMU trajectory was obtained similarly by adding simulated IMU sensor errors to the incremental velocity and angle data. The models for the corrupted data were:

$$\Delta\tilde{\theta} = (1+\kappa_G)\Delta\theta + d + \sum_{i=0}^{k} \sigma_{w_G}^{i} \cdot \Delta t \qquad (3.80)$$

$$\Delta\tilde{v} = (1+\kappa_A)\Delta v + b + \sum_{i=0}^{k} \sigma_{w_A}^{i} \cdot \Delta t \qquad (3.81)$$

Note that d refers to the gyro bias, b to the accelerometer bias, σ_{w_G} and σ_{w_G} are the standard deviation of the gyro and accelerometer white noise, κ_A and κ_G to the corresponding scale factor errors, k is the current epoch t_k, and $\Delta t = t_{k+1} - t_k$ to the time interval of the sensor data (1/50s).

The gyro and accelerometer white noise are generated by multiplying a standardized Gaussian random number which has the standard deviation of ± 1 (no unit) to the standard deviation of the gyro and accelerometer white noise giving random number $\sigma^i_{w_G}$ and $\sigma^i_{w_A}$. For example, the standard deviation of gyro white noise of the HG1700 is computed as $\sigma_w = \sqrt{\frac{q}{\Delta t}}$ (where q is the Power Spectral Density (PSD) of the gyro white noise and it can be obtained from the random walk of the gyro and accelerometer of the HG1700 $0.125\frac{\deg}{\sqrt{hr}} = \frac{0.0022rad}{60\sqrt{s}} = 0.0000367\frac{\text{rad}}{\sqrt{s}}$ or $0.0000367\frac{\text{rad}}{s}\Big/\sqrt{Hz}$ and $\frac{0.09m/s}{\sqrt{hr}} = \frac{0.09m/s}{\sqrt{3600\cdot s}} = \frac{0.0015m/s}{\sqrt{s}}$, see Table 3.2 for the random walk of HG1700)

	parameters	Contents	
Input	initpos	initial position of vehicle (n-frame) (meters) $[0 \quad 0 \quad 0]$	
	initvel	initial velocity vector (n-frame) (m/s) $[0 \quad 0 \quad 0]$	
	Initaccel	Initial acceleration (m/s^2) $[0.05 \quad 0.05 \quad 0.05]$	
	initdcm	initial direction cosine matrix (n-frame to b-frame) $\begin{bmatrix} 1 & 0 & 0 \\ 0 & 1 & 0 \\ 0 & 0 & 1 \end{bmatrix}$	
	Segparam (9 segment parameters)	1	segment type identifier
		2	duration (in seconds)
		3	total acceleration
		4	amount of turn (degrees)
		5 ~8	used for transitions only
		9	time step (seconds)
Output	profile(i,1:3)	generated path (n-frame)	
	profile(i,4:6)*	velocity (n-frame)	
	profile(i,7:9)	acceleration (b-frame)	
	profile(i,10:18)*	elements of the direction cosine matrix(DCM) from b-frame to n-frame	
	profile(i,19)	simulation run time (seconds)	

Table 3.4. Input and Output Profiles of the Matlab INSToolkit.

In addition, the ranging solution for the trajectory was determined by adding random noise to the actual coordinates (The latitude and longitude are converted into the Global XYZ coordinate system to add GPS random noise in table 3.3). That is, it was assumed that the ranging system would be free from all systematic errors, and the final solution would be corrupted only by white noise:

$$\tilde{\phi}_r = \phi_r + \nu \cdot \sigma_r \tag{3.82}$$

$$\tilde{\lambda}_r = \lambda_r + \nu \cdot \sigma_r \tag{3.83}$$

$$\tilde{h}_r = h_r + \nu \cdot \sigma_r \tag{3.84}$$

Here, ν refers to a standardized random variable following the zero-mean, unit-variance Gaussian distribution (see Table 3.3 for σ_r). The ranging solution coordinates were used in the filter to update the IMU position errors and to estimate the systematic errors in the inertial sensors. To simulate prolonged interruptions in the ranging solution, GPS updates were intentionally removed from the Kalman filter process at longer intervals. Figure 3.5 illustrates the general simulation and analysis process.

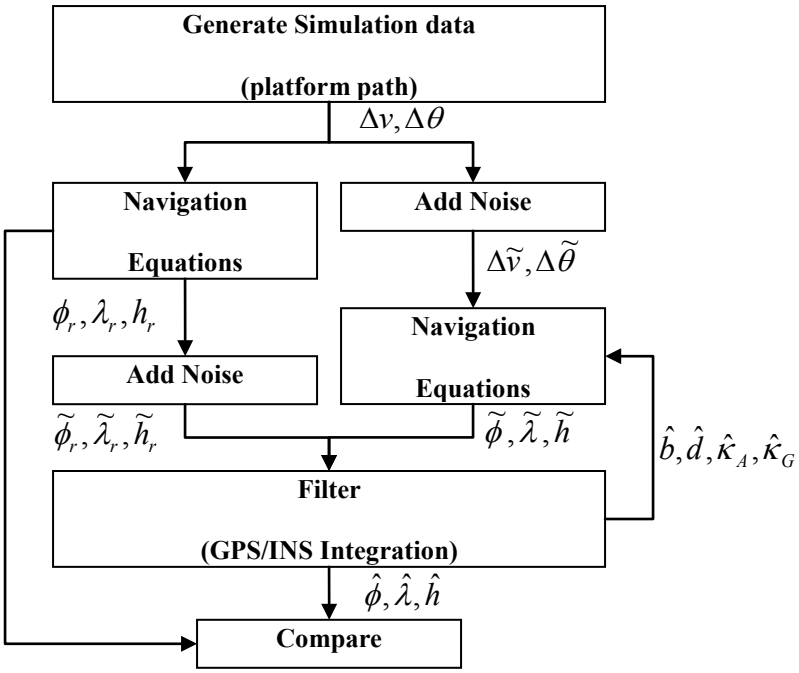

Figure 3.5. Loosely coupled, decentralized INS/GPS integration and simulation analysis procedure.

3.4.3 Test Results

The free-inertial navigation solutions just before each external measurement update, determined using the EKF, UKF, and UPF with update intervals of 1 s, 10 s, and 30 s, were compared with those of the control trajectory. The ranging solution updates were either GPS or total station observations, and all of the three types of inertial sensors were tested. Within each set of sensor/update tests, the true position errors also indicated how well the filter could estimate the systematic errors of the inertial sensor in the particular non-linear environment. The comparison against the control trajectory was conducted by computing the position errors vector ($z = \begin{bmatrix} z_\phi, z_\lambda, z_h \end{bmatrix}$) from the three coordinate errors.

$$z_\phi = \left[\phi_{INS} - \phi_{GPS},\right],\ z_\lambda = \left[\lambda_{INS} - \lambda_{GPS}\right],\ z_h = \left[h_{INS} - h_{GPS}\right] \tag{3.85}$$

In addition, the standard deviations of position error (z_σ , equation (3.86)) for each of the curved and straight sections of the test trajectory (see Figure 3.3) were computed as follow.

$$z_\sigma = \sqrt{z_{\phi,\sigma}^2 + z_{\lambda,\sigma}^2 + z_{h,\sigma}^2} \tag{3.86}$$

where $z_{\phi,\sigma} = \sqrt{\sum_{i=1}^{N}\left(z_\phi^i - \bar{z}_\phi\right)^2 \Big/ N}$, $z_{\lambda,\sigma} = \sqrt{\sum_{i=1}^{N}\left(z_\lambda^i - \bar{z}_\lambda\right)^2 \Big/ N}$, and $z_{h,\sigma} = \sqrt{\sum_{i=1}^{N}\left(z_h^i - \bar{z}_h\right)^2 \Big/ N}$ and $\bar{z}_\phi$, $\bar{z}_\lambda$, and $\bar{z}_h$ is the mean of z_ϕ , z_λ , and z_h , respectively.

As shown in Figure 3.6 (for 1 s updates only), more precise updates (total station vs. GPS) yielded more accurate free-inertial solutions because the integration with the inertial sensor outputs began with a smaller error. More interestingly, in this particular simulation, there was little difference between the high-end and the medium quality inertial sensors, and this indicated that either one could offer similar interpolation capability within 1 second. Clearly, the EKF did not perform as well as the UT-based filters (UKF and UPF), particularly for the curved segments of the trajectory. The UPF demonstrated only slightly better performance than the UKF in the tests since the simulated noise processes for the inertial sensors and the observation updates were Gaussian. As the interval before the next update increased, the inertial sensor errors accumulated, but the UKF and UPF still out-performed the EKF, as shown in Figure 3.7. It is noted that the position accuracy of the filters was useful only for the screening purposes of MEC detection when the GPS outage reached 10 s.

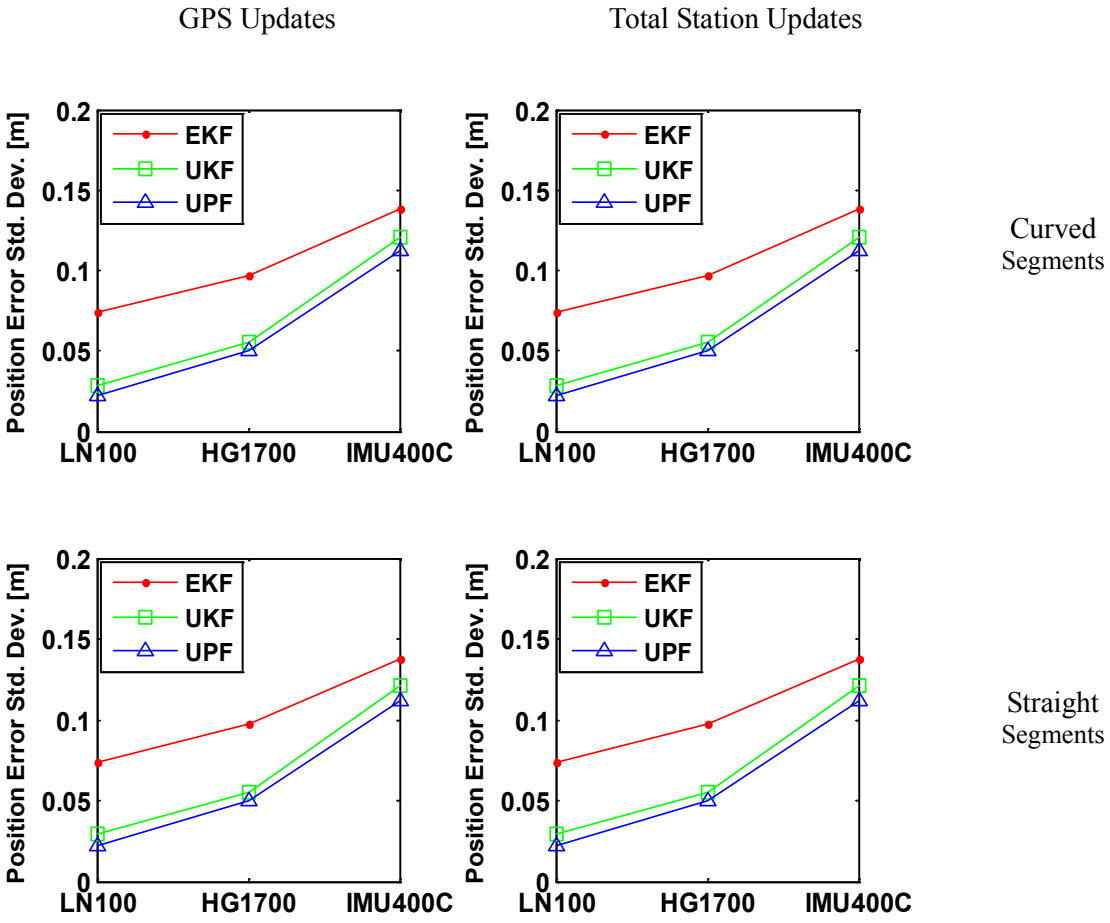

Figure 3.6. Standard deviation of errors with different IMU grades with the 1 s ranging system updates using different filters (first row: curved segments, second row: straight segments, first column: GPS, second column: Total Station) (units: cm).

In addition to the outright interruptions in the ranging solution, it was thought that it might also be degraded during several seconds of the survey. In relation to this point, only differential GPS solutions were considered, and it was assumed that such degradation was a function of the baseline length between the rover and the fixed base station. Using the corresponding increased observation noise (see Table 3.3) Figure 3.8 compares the EKF and UKF performances with respect to the medium-grade IMU, free-inertial positioning accuracy at the end of 1 s and 5 s prior to the degraded GPS updates. Again, the UKF demonstrated improved results over the EKF, especially when both the degradation and the update interval increased.

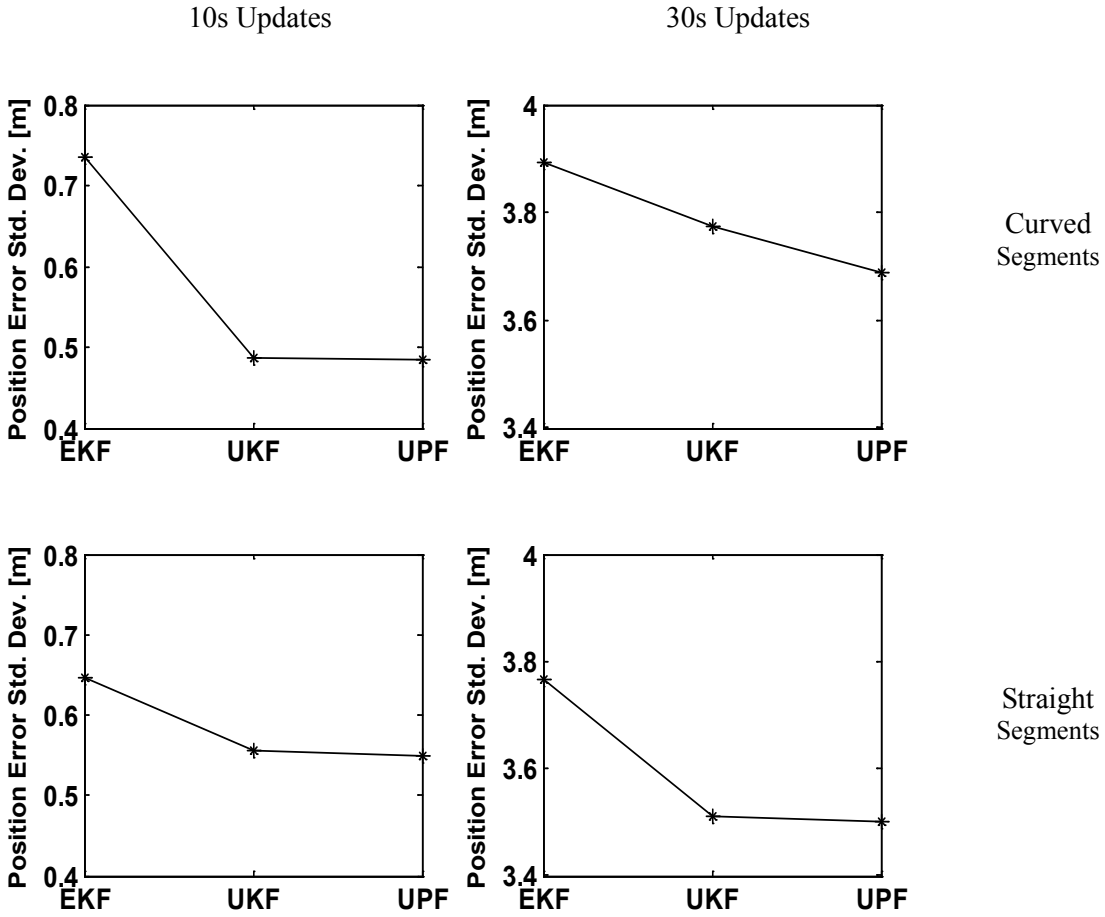

Figure 3.7. Standard deviation of errors for different filtering methods (first row: curved segments, second row: straight segments, first column: 10 s, second column: 30 s GPS updates of the medium-grade IMU) (units: cm).

It is worth mentioning that the superiority of the UKF can be realized only with an appropriate tuning of the scaling parameter, α. In this regard, the optimal value $\beta = 2$ was used for these tests since the error states were excited by Gaussian noise. Note that the results shown in Figure 3.6 and 3.7 were obtained with $\alpha = 0.15$ that corresponds to sigma points within a range of $\pm 1\sigma$. While expanding the range did not improve the estimation, significantly smaller α values (i.e., $\alpha = 0.0001, \alpha = 0.001$, and $\alpha = 0.01$) degraded the UKF performance as shown in Figure 3.8.

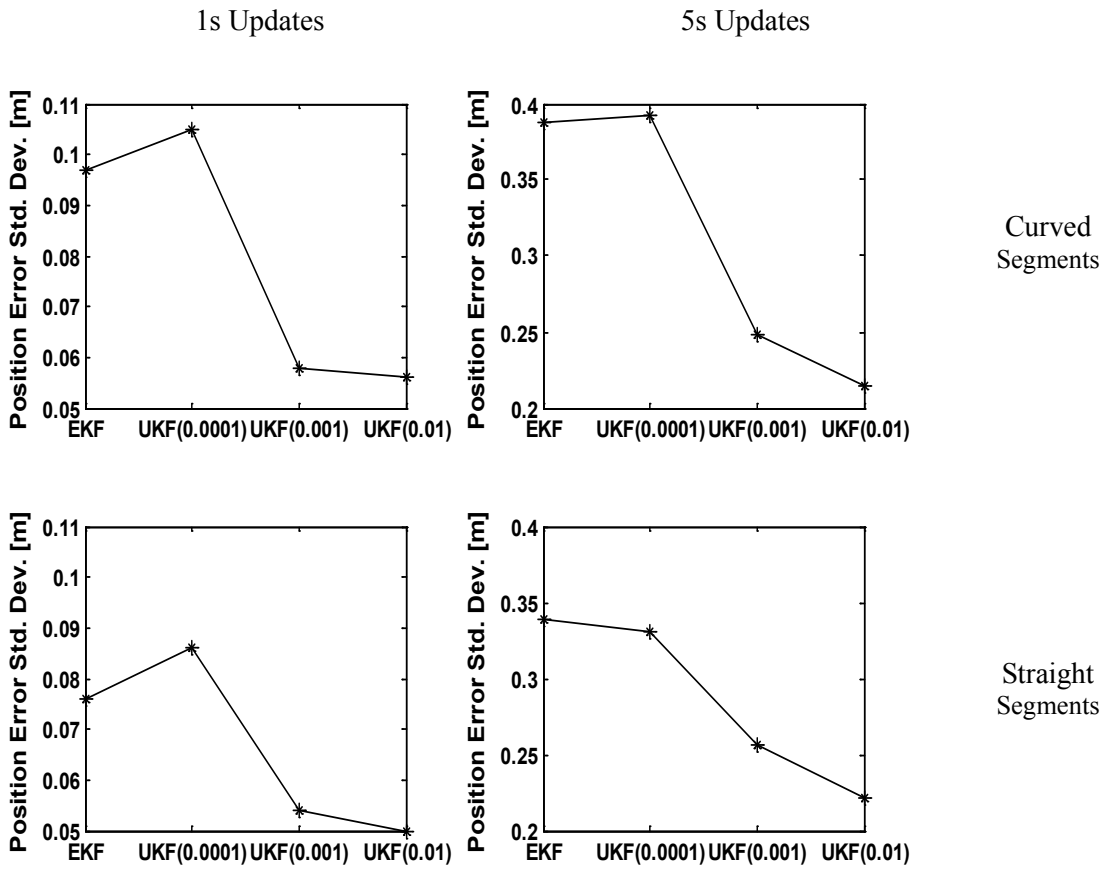

Figure 3.8. Standard deviation of errors with medium-grade IMU and degraded GPS updates and with different scales in the UT (first row: curved segments, second row: straight segments, first column: GPS 1 s updates, second column: GPS 5 s updates).

The simulation tests being discussed assumed a system driven by Gaussian noise. Thus, one may expect similar results with other symmetrically distributed processes, and the UKF could also be tuned to deal with non-Gaussian, symmetric distributions using the parameter, β. However, dynamic systems, besides being generally non-linear, may also be excited by *non-symmetric* processes (Kushner, 1967). Indeed, Reddy and Herr (2006) investigated the skewness of IMU sensor errors. Julier (1998) and Naveaua et al. (2005) also proposed modeling the process noise with asymmetric probability densities. Therefore, both symmetric non-Gaussian and asymmetric distributions were considered to determine the particle filter's performance.

In one test, sensor errors were generated from a uniform distribution with the same variance as in the Gaussian case. As shown in Table 3.5, the 3D position error standard deviations were slightly lower in value with the particle filter in 1 sec and 5 sec updates.

		1s Updates	5s Updates
Curved segments	UKF	0.056	0.214
	UPF	0.055	0.211
Straight segments	UKF	0.048	0.221
	UPF	0.049	0.202

Table 3.5. Statistics of errors (std. dev.) using nonlinear filters on data from a medium-grade IMU with uniformly distributed errors (units: cm).

In addition, the following asymmetric probability density (APD) was considered (Komunjer, 2007):

$$f(u)=\begin{cases} \dfrac{\delta_{\alpha,\lambda}^{1/\lambda}}{\Gamma(1+1/\lambda)}\exp\left[-\dfrac{\delta_{\alpha,\lambda}}{\alpha^{\lambda}}|u|^{\lambda}\right], & \text{if } u\le 0, \\ \dfrac{\delta_{\alpha,\lambda}^{1/\lambda}}{\Gamma(1+1/\lambda)}\exp\left[-\dfrac{\delta_{\alpha,\lambda}}{(1-\alpha)^{\lambda}}|u|^{\lambda}\right], & \text{if } u>0, \end{cases} \tag{3.87}$$

where

$0\le\alpha\le 1$, $\lambda>0$ and $\delta_{\alpha,\lambda}=\dfrac{2\alpha^{\lambda}(1-\alpha)^{\lambda}}{\alpha^{\lambda}+(1-\alpha)^{\lambda}}$.

Note that when $\alpha=0.5$, the density is symmetric, and when also $\lambda=2$, the APD is the Gaussian density. For the tests, λ was selected as 2, and two values, $\alpha=0.25$ and $\alpha=0.75$ was chosen, the latter for the gyro noise and the former for the accelerometer noise (Figure 3.9). Figure 3.10 compares the statistics of the position errors as a function of update rates and GPS degradation with and without the asymmetry in the IMU sensor noises as shown in Figure 3.9. It is noted that both the UKF and EKF performances were significantly degraded in the presence of the IMU noise asymmetry. Furthermore, it was found that the UKF failed to be consistently superior to the EKF, especially in the straight sections of the trajectory. Even in the curved sections, the advantage of the UKF discussed earlier was compromised in case of the longer ranging gaps and the degraded GPS solutions.

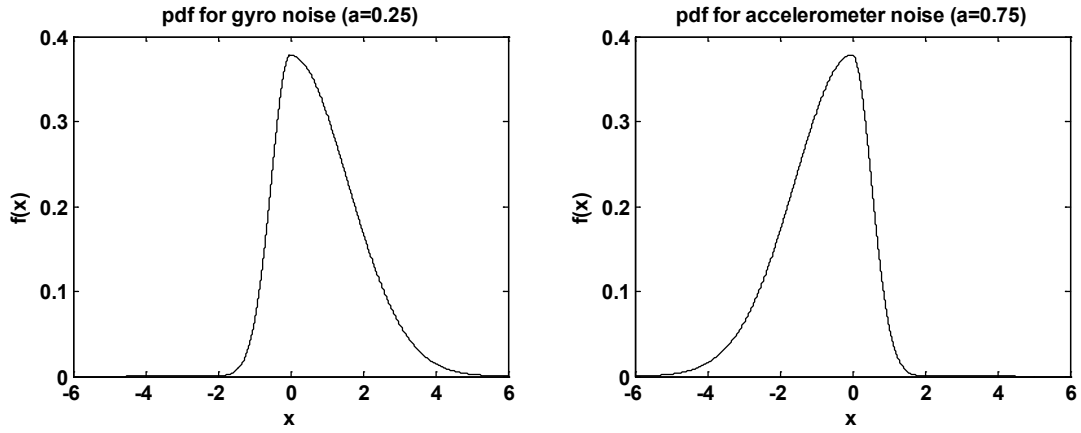

Figure 3.9. Asymmetric pdf's used for gyro noise ($\lambda = 2$, $\alpha = 0.25$) and accelerometer noise ($\lambda = 2$, $\alpha = 0.75$).

In the meantime, since the particle filter was designed to operate with non-Gaussian error sources, the UPF was applied to the IMU data corrupted by the asymmetric noise, and the position errors were compared with those of the UKF and EKF for the same degraded GPS updates as in Figure 3.10. Figure 3.11 shows that the performance of the UPF was superior to the other filters, for both curved and straight segments of the trajectory. This was an interesting finding because the UPF yield better results than the UKF alone although it still used the unscented Kalman filter before the re-sampling of the particles. Moreover, as Figure 3.11 shows, increasing the number of particles did not yield significant improvements in the UPF. The overall positioning accuracy deteriorated as the GPS update interval increased (e.g., 5 s). For example, the standard deviation in position using the UPF with asymmetric error distribution was worse than that with the UKF with symmetrically distributed errors. However, the UPF still performed better than the other filters when the sensor noise was asymmetric.

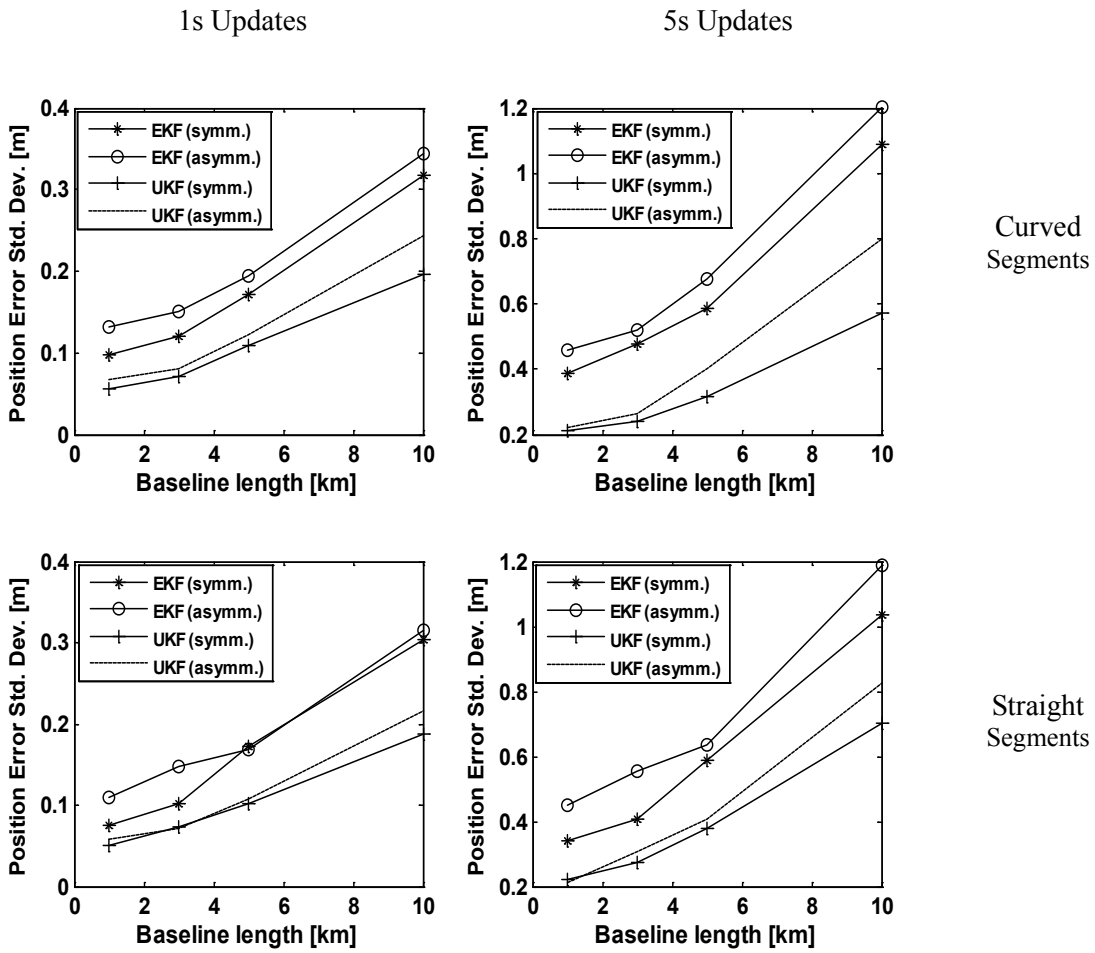

Figure 3.10. Standard deviation of medium-grade IMU position errors with asymmetric sensor error distributions, for baseline-degraded GPS updates (first row: curved segments, second row: straight segments, first column: 1 s updates, second column: 5 s updates).

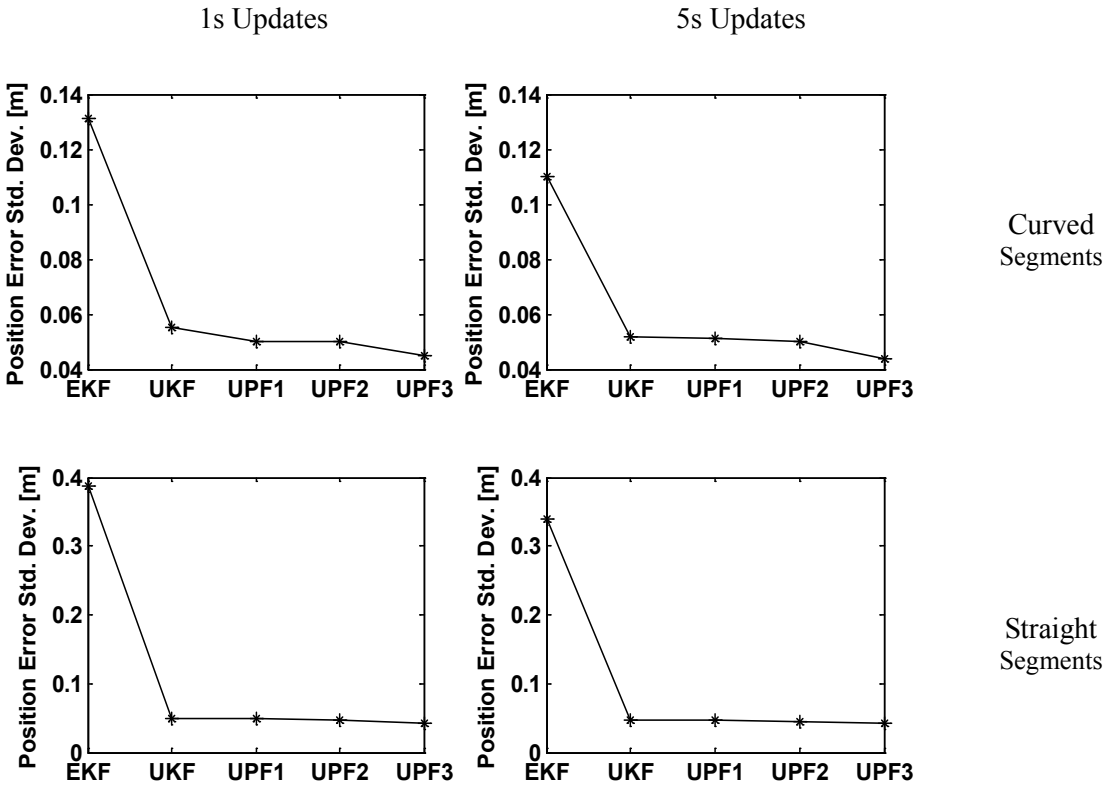

Figure 3.11. Standard deviations of medium-grade IMU position errors (first row: curved segments, second row: straight segments) for EKF, UKF, UPF[1](200), UPF[2](400), UPF[3](600) with 1 s GPS updates (first column) and with 5 s updates (second column). The number in parenthesis is the number of particles. GPS update accuracy is for the 1 km baseline (Table 3.3), and the IMU sensor noise was assumed to be asymmetric as in Figure 3.10 (units: cm).

The simulated data from the target characterization survey over the small (1 square meter) patch (Figure 3.4) were subjected to the RTS-smoother applied to each of the filters discussed here. In the trajectory, there were only two control points (beginning and end), and the tactical-grade IMU was considered to have the highest precision among IMUs available for practical deployment (hand-held sensor). The errors starting from the initial control point generally increased along the trajectory, typically reaching a maximum close to its along-track center, and decreased to zero at the other control point. Table 3.6 presents the maximum true error (not necessarily at the center) from a single simulation and the standard deviation predicted by the smoother at the along-track center (where it is maximum). It was evident that the post-survey smoothing is a powerful technique to reduce free-inertial geolocation errors between the control points. Therefore, it can be concluded that the tactical- grade IMUs have the potential to meet the geolocation requirements for target characterization.

		Before Smoothing		After Smoothing	
methods	coordinates	simul. abs. max	max. pred. st.dev.	simul. abs. max	max. pred. st.dev.
EKS	North	79.1	24.0	9.7	4.2
	East	63.2	22.1	14.9	5.3
UKS	North	59.8	22.9	9.1	4.8
	East	51.1	20.8	9.7	4.2
UPS	North	57.8	24.8	8.6	4.9
	East	48.9	18.4	9.2	4.0

Table 3.6. Position error statistics of free-inertial navigation along the trajectory (Figure 3.4), using the tactical-grade IMU and Gaussian distribution for IMU error (unit: cm).

Similar to the previous filtering tests which employed data from a medium-grade IMU with uniformly distributed errors, the smoothing results by the UKS and UPS were compared when the uniform distribution was employed to generate the disturbed IMU data. The nonlinear filter based smoothing (UKS and UPS) show the similar or better performance than the EKS (see Table 3.7).

		Before Smoothing		After Smoothing	
methods	Coordinates	simul. abs. max	max. pred. st.dev.	simul. abs. max	max. pred. st.dev.
EKS	North	65.2	16.4	9.6	5.1
	East	29.1	9.3	13.2	4.2
UKS	North	63.2	15.1	13.8	5.4
	East	25.9	9.2	8.0	2.8
UPS	North	59.1	13.9	10.2	4.9
	East	28.5	9.3	9.8	3.1

Table 3.7. Position error statistics of free-inertial navigation along the trajectory as shown in Figure 3.4, tactical-grade IMU and uniform distribution for IMU error (Unit: cm).

These three smoothers were also compared with each other in the case of asymmetric probability densities. Table 3.8 shows that the UPS performs better than slightly the other smoothing methods.

		Before Smoothing		After Smoothing	
methods	Coordinates	simul. abs. max	max. pred. st.dev.	simul. abs. max	max. pred. st.dev.
EKS	North	222.1	72.6	32.4	9.6
	East	314.8	89.8	30.4	8.6
UKS	North	248.7	69.3	27.8	10.4
	East	272.4	89.6	20.2	5.1
UPS	North	226.7	73.0	24.6	9.4
	East	292.8	92.2	18.0	6.7

Table 3.8. Position error statistics of free-inertial navigation along the trajectory as shown in Figure 3.4, tactical-grade IMU and asymmetric distribution for IMU error (Unit: cm).

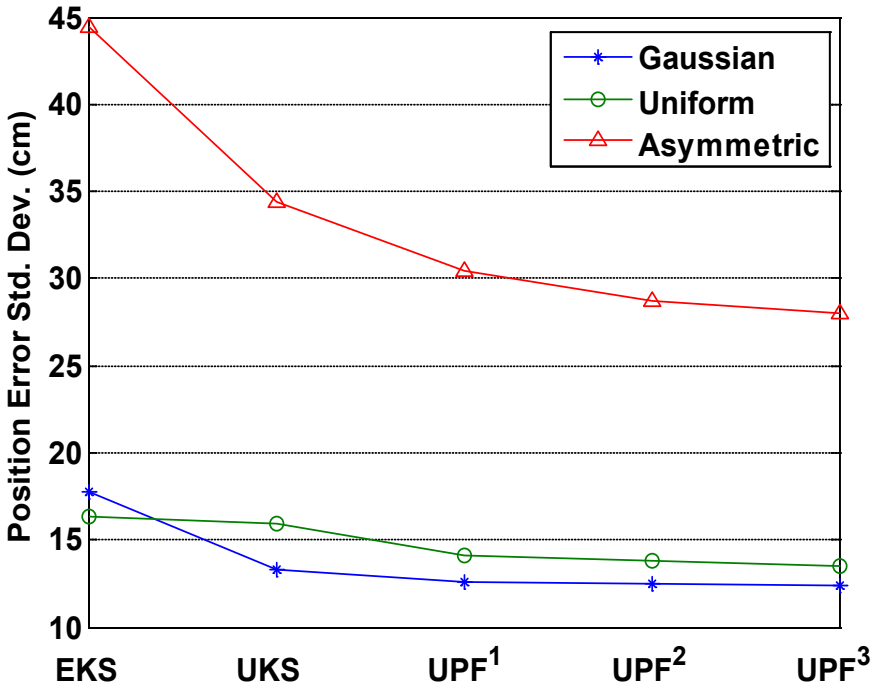

Figure 3.12. Absolute maximum error of medium-grade IMU position after smoothing for EKS, UKS, UPS[1](10), UPS[2](50), UPS[3](100) when Gaussian, uniform, and asymmetric probability density function were applied to generate raw IMU data. The number in parenthesis refers to the number of the particles.

Similarly to the results shown in Figure 3.11, Figure 3.12 shows that the increasing number of particles beyond 10 did not significantly improve the smoothing results.

3.4.4 Summary

An integrated ranging/IMU geolocation system has been proposed for the purpose of satisfying the precise positioning requirements for MEC detection and characterization (U.S. Army Corps of Engineers, 2006). This chapter, reviewed the currently available filtering/smoothing techniques, and showed the results of tests conducted on a simulated ranging system integrated with inertial sensors of different levels of accuracy. More specifically, based on simulated trajectories that were typical in MEC ground surveys, potential position improvement was analyzed with alternative filters that avoid the linearization of an inherently non-linear dynamics system. Moreover, it was pointed out that the Gaussianity assumption in the driving noise assumed for the Bayesian interpretation the Kalman filters could also be circumvented by other filters, based on more general Bayesian statistical propagation.

Simulation results showed that the unscented Kalman filter and the unscented particle filter performed consistently better than the standard extended Kalman filter (without iteration), particularly along the curved trajectories. These improvements in filter strategy were demonstrated especially when the interval of the ranging solution update was several seconds (simulating an outage due to signal occlusions) and when the ranging solution was degraded (simulating various possible causes).

The tests showed that particle filters, which avoid the Gaussianity assumption, are particularly useful when the driving noise of the system has an asymmetric distribution. More specifically, while the UKF and EKF performed comparably, in this case, the UPF yielded significantly improved position accuracy. The UPF results were generally insensitive to the number of particles.

From the results of the tests with different filters, it was concluded that achieving a few centimeters of positioning accuracy in dynamic environments requires non-linear filters such as the UKF and UPF. However, these filters cannot overcome the natural accumulation of IMU errors as the ranging solution update interval increases. Nevertheless, in every case, the new non-linear filters performed better than the standard EKF that does not involve iteration. With iteration, however, it may become a truly nonlinear filter and certainly wave of a competitor to both UKF and UPF.

It was also shown that tactical-grade IMUs have the potential to provide free-inertial positioning for sensors passing over local (1 square meter) patches for target characterization and discrimination. This was achieved with the minimal number of control points and the use of a post-survey optimal smoothing algorithm. Similar to the filtering results, the simulation showed that the nonlinear based smoothing methods (UKS and UPS) performed better than the linear-filter based smoother (EKS). Again, if would be interesting to see how the EKS performs when based on the nonlinear EKF, involving iterations.

CHAPTER 4: NEURAL NETWORK AIDED ADAPTIVE FILTERING

Potential difficulties of the EKF and UKF are the need for accurate statistics of the system and measurement errors. There may be are overcome by the adaptive filtering method. The a priori information of the system and measurement noise (as represented by the covariance matrices, Q and R) can be adjusted according to the accuracy of estimation (Salychev and Schaffrin, 1992; Schaffrin, 1994; Salychev, 1999) Originally developed for the EKF by Salychev and Schaffrin (1992) this technique has also been applied to the UKF.

The traditional adaptive filtering method may be further aided by a neural network trained on a given set of platform dynamics. The Kalman filter estimates the navigation errors in position, velocity and attitude using external control. At the same time, the neural network is trained to map a relationship between the platform dynamics (the input) and the Kalman filter estimations (the desired output) when measurements (external control points) are available. If measurements are not available (GPS outage), the trained output of the neural network is used to aid in the estimation of the process noise covariance.

In this chapter, the improvement in the geolocation accuracy was studied when the neural network approach is applied to aid the adaptive versions of the extended Kalman filter (EKF) and the unscented Kalman filter (UKF).

4.1 Adaptive Filtering

One potential difficulty with any of the previously discussed navigation filters is the requirement for accurate a priori description of the system and measurement errors (noise). Also, these errors are assumed to be piecewise constant in the filtering process. However, the errors in the navigation system may not be suitably described by the chosen statistics, especially in a highly dynamic environment, which is typically encountered by UXO detection equipment.

Various adaptive methods have been studied and proposed in many scientific publications. Most adaptive algorithms employ the innovation sequence of the system and measurement noise covariance (Q and R) because the innovations of the Kalman filter are reliable indicators of the filter performance. Q and R affect the weight that the filter applies between the existing process information and the latest measurements. Thus they have a significant impact on the filtering performance (Grewal and Andrews, 1993; Grewal and Weil, 2001). Since these methods use a window function applied to the most recent innovations, it is also required to correctly identify the window size.

4.1.1 Adaptive Extended Kalman Filter (AEKF)

The main idea of the Adaptive Extended Kalman filter (AEKF) is to make the Kalman

filter residuals consistent with the random errors as defined by their theoretical covariances (Mehra, 1972). In the adaptive Kalman filter (AKF), the a priori information of the system and measurement noise (Q and R) can be adjusted according to the accuracy of estimation (Schaffrin, 1994; Salychev, 1999).
If the covariance matrix, R_k, is unknown or inaccurate, it can be estimated from the covariance matrix of the innovation sequence (υ_k, equation (3.19)). Let

$$C_k = E\left(\upsilon_k \upsilon_k^T\right) = HP_k^- H^T + R_k \tag{4.1}$$

where an estimate of this covariance is

$$\hat{C}_k = \frac{1}{m}\sum_{i=0}^{m-1} \upsilon_{k-i}\upsilon_{k-i}^T \tag{4.2}$$

and where m is the estimation window size. Also, the estimate $\hat{C}_k$ satisfies the following recursion

$$\hat{C}_k = \frac{k-1}{k} C_{k-1} + \frac{1}{k}\upsilon_k \upsilon_k^T \tag{4.3}$$

Therefore, an estimate of the measurement covariance matrix is obtained using $\hat{C}_k$ and (4.1) via

$$\hat{R}_k = \hat{C}_k - HP_k^- H^T \tag{4.4}$$

In case that the covariance of the system noise is unknown; the following identities can be obtained from equations (3.14) and (3.19):

$$\begin{aligned} G_k E\left(w_k\right) &= E\left(x_k\right) - F\left(t_k, t_{k-1}\right)E\left(x_{k-1}\right) \\ &= \hat{x}_k - F\left(t_k, t_{k-1}\right)\hat{x}_{k-1} \\ &= K_k \upsilon_k \end{aligned} \tag{4.5}$$

and hence

$$GE\left(\hat{w}_k \hat{w}_k^T\right)G^T = K_k E\left(\upsilon_k \upsilon_k^T\right)K_k^T \approx K_k \hat{C}_k K_k^T \tag{4.6}$$

4.1.2 Adaptive Unscented Kalman Filter (AUKF)
Since the nonlinear filters such as UKF are affected by potentially inaccurately modeled noise statistics, particularly during intervals of GPS outages and highly dynamic trajectories, the adaptive methods should be employed to mitigate these effects and

improve the filter performance.
Of the six components of the UKF (the initial states and their error variance, the variances of process noise (Q) and measurement noise (R), and the two unscented transformation parameters (α and β)), the Q and R matrices can cause the most significant influence on the performance and stability of the UKF. The initial states and their error variance have negligible influence on the filter process data. The UT parameters only affect higher order terms of the nonlinear functions and yield comparable results if α is not too small (Lee and Jekeli, 2009). Therefore, usually the innovation-based covariance matching algorithm is employed to tune the Q and R matrices, which is the adaptive method also used for the unscented Kalman filter (Song and Han 2008). In this chapter, the adaptive estimation of the process noise covariance Q is considered.
The goal of the innovation-based covariance matching algorithm is to minimize the difference (cost function, equation (4.9) below) between the time-averaged innovation covariance and the filter-computed innovation covariance (Garcia, 1997). The time-averaged innovation covariance (from equation (4.2)) is

$$S_k = \frac{1}{m}\sum_{i=0}^{m-1} \upsilon_{k-i}\upsilon_{k-i}^T \tag{4.7}$$

where *m* is the size of the estimation window and υ_k is the innovation sequence, equation (3.19).
The filter-computed innovation covariance can be written as (from Table 3.1)

$$\hat{S}_k = \sum_{i=0}^{2n_x} W_i^{(c)} \left(Y_{i,k}^- - \hat{y}_k^-\right)\left(Y_{i,k}^- - \hat{y}_k^-\right)^T + R \tag{4.8}$$

Then, the following cost function for the adaptive UKF is to be minimized

$$V_k = tr\left[\left(\Delta S_k^2\right)\right] = tr\left[\left(S_k - \hat{S}_k\right)^2\right] \tag{4.9}$$

The m-th diagonal element of the process noise matrix, Q, at time k, q_k^m, is adjusted using

$$\dot{q}_k^m = -\eta \frac{\partial V_k}{\partial q_k^m} \tag{4.10}$$

where η is the adjustment rate for the convergence speed. The adjustment is done recursively using equation (4.10) is

$$q_k^m = q_{k-1}^m - \eta \frac{\partial V_k}{\partial q_k^m} \cdot \Delta t \tag{4.11}$$

where Δt is the sampling (constant) time.
From equation (4.9) the derivative of V_k is calculated as follows

$$\frac{\partial V_k}{\partial q_k^m} = \frac{\partial}{\partial q_k^m}\left[tr\left(\Delta S_k^2\right)\right] = tr\left(\frac{\partial \Delta S_k^2}{\partial q_k^m}\right) = tr\left(\frac{\partial \Delta S_k}{\partial q_k^m}\Delta S_k + \Delta S_k \frac{\partial \Delta S_k}{\partial q_k^m}\right) \tag{4.12}$$

where

$$\frac{\partial \Delta S_k}{\partial q_k^m} = \frac{\partial}{\partial q_k^m}\left(S_k - \hat{S}_k\right) = \frac{\partial S_k}{\partial q_k^m} - \frac{\partial \hat{S}_k}{\partial q_k^m} \tag{4.13}$$

and

$$\begin{aligned}\frac{\partial S_k}{\partial q_k^m} &= \frac{1}{N}\sum_{i=k-N+1}^{k}\left(\frac{\partial \upsilon_k}{\partial q_k^m}\upsilon_k^T + \upsilon_k\frac{\partial \upsilon_k^T}{\partial q_k^m}\right) \\ &= \frac{1}{N}\sum_{i=k-N+1}^{k}\left(-\frac{\partial \hat{y}_k^-}{\partial q_k^m}(y_k - \hat{y}_k^-)^T - (y_k - \hat{y}_k^-)\frac{\partial \hat{y}_k^-}{\partial q_k^m}\right)\end{aligned} \tag{4.14}$$

$$\frac{\partial \hat{S}_k}{\partial q_k^m} = \sum_{i=0}^{2n} W_i^{(c)}\left(-\frac{\partial \hat{y}_k^-}{\partial q_k^m}(Y_{i,k}^- - \hat{y}_k^-)^T - (Y_{i,k}^- - \hat{y}_k^-)\frac{\partial \hat{y}_k^{-,T}}{\partial q_k^m}\right) \tag{4.15}$$

For more detailed derivations and equations see Song and Han (2008).

4.2 Neural Network

Artificial intelligence has provided a successful and effective solution to certain engineering and science problems that could not be solved easily by using conventional methods (Cawsey, 1998). It is claimed that the various artificial intelligence approaches such as neural network, fuzzy logic, evolutionary computing, probabilistic computing, expert programming, and genetic programming can provide the intelligence and robustness in complex and uncertain systems similar to those seen in natural biological species (Honavar and Uhr, 1994).

A neural network is a machine learning algorithm which is designed to mimic the current perception of the human brain mechanism (Haykin, 1999). First, the network acquires (accumulates) information through a pre-designed learning process. Second, interneuron connection strengths (also known as synaptic weights) are used to store the acquired knowledge (Aleksander and Morton, 1990). The neural network has demonstrated to provide a successful alternative solution to many engineering problems such as pattern recognition, nonlinear functional mapping, and applications associated with classification, speech, vision and control (Mendel and McLaren, 1970; Barto et al., 1983).

In this chapter, a neural network is used to aid the adaptive forward filtering applied to the IMU/GPS integrated systems because it can learn input-output relationships without a priori knowledge of the dynamic models and noise statistics of the measurements (Jwo and Huang, 2004; Wang et al., 2006 and 2007).

4.2.1 Introduction

Neuron: An artificial neuron consists of the three elements, a synaptic weight (weight), an adder (somatic) and a transfer (activation) function. It is the basic information-processing unit of any neural network (Haykin, 1999). The synaptic weight is used for weighting the input signal. An input signal x_i is multiplied by the synaptic weight w_{ji} and connected to neuron j. An adder sums up the weighted input signals (simply, $v_j = \sum_{i=1}^{n} w_{ji} x_i$). Also, the neuron model has a bias (b_j, also called the external threshold) which is used to increase or lower the input of the transfer function. The transfer function limits the amplitude range of the output signal to a finite value.

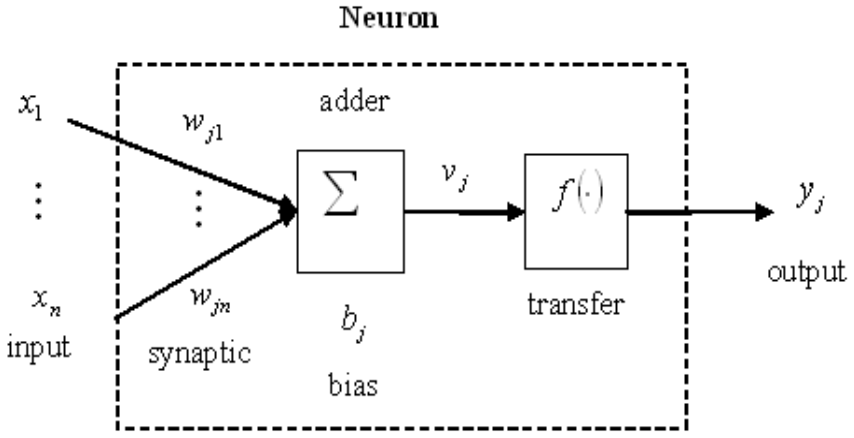

Figure 4.1. The neuron with three basic elements.

Therefore, the simple model of a j th neuron is

$$y_j = f\left(\sum_{i=1}^{n} w_{ji} x_i - b_j\right) \tag{4.16}$$

where f is a certain transfer function, $b_j \in R$ is a bias, w_{ji} are synaptic weights, x_i are inputs ($i = 1,2,\ldots,n$), n is the number of inputs, and y_j represents the output. The four most common transfer functions, including the "hard limiter" (a binary or bipolar) function, the linear function, the saturating (or piecewise) linear function, and the sigmoid (s-shaped) nonlinear function, are used according to the application.

One type of sigmoid function is the binary sigmoid function (f_{bs}) which has an output in the range (0, 1):

$$y = f_{bs}(v) = \frac{1}{1+e^{-av}} \tag{4.17}$$

where α is the slope parameter of the binary sigmoid function.
A second type of sigmoid function is called the hyperbolic tangent sigmoid, given by

$$y = f_{hts}(v) = \tanh(\alpha v) \tag{4.18}$$

where α is also the slope parameter.

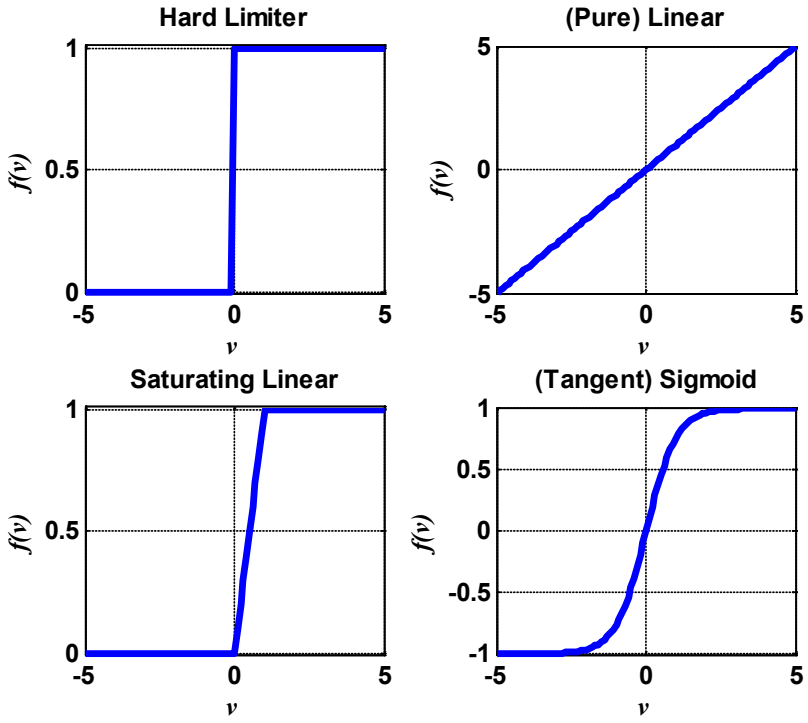

Figure 4.2. Transfer functions (Hard-limit, Linear, Saturating Linear and (Tangent) Sigmoid).

Neural Network: Multiple neurons are used to form a layer to build a neural network. According to Haykin (1999), layers can be combined into single-layer feed forward networks (one input and one output layer, SFNs), multi-layer feed forward networks (multiple hidden and multiple output layers, MFNs), and recurrent networks (at least one feedback loop based on SFNS or MFNs, RNs).

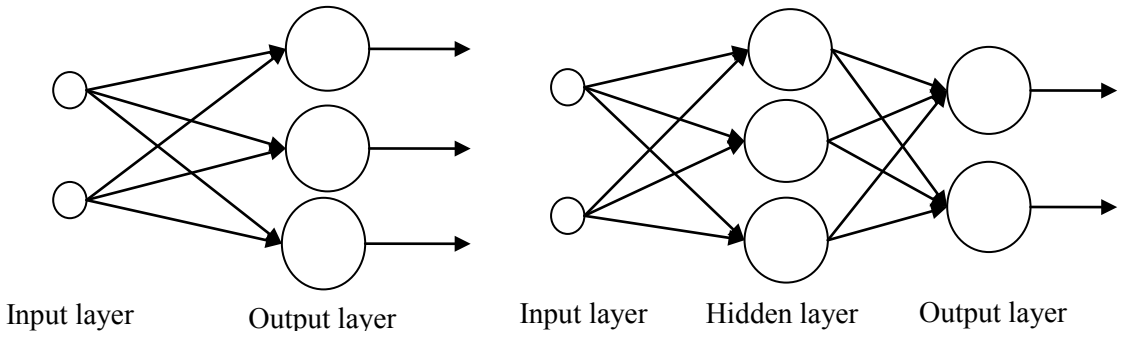

Figure 4.3. Single-layer feed-forward networks and multi-layer feed-forward networks.

Demuth and Beale (2004) show that the two-layer feed-forward networks (where the first layer has the sigmoid transfer function and the second has the linear function) can be trained to approximate any arbitrary nonlinear function. Golden (1996) also shows a MFN which has an *appropriate number* of hidden neurons and hidden layers that can provide the best approximation accuracy to the unknown model. The number of hidden neuron and number of hidden layer is determined by a rule-of-thumb. For example, if the (dynamic) system has simple (linear) structure, one hidden layer and one output layer are usually selected. If the system has complicated structure, more than two hidden layers and one output layer are chosen.

Learning: The goal of learning is to adapt the neural network to desired conditions by adjusting the synaptic weight and bias parameters. According to Anthony and Bartlett (1999) the learning procedures of the neural network can be classified into four categories: supervised learning, unsupervised learning, reinforcement learning and hybrid learning. In supervised learning, a supervisor (or a teacher, e.g., filter designer) who has knowledge of the input-output relationship of the neural network can provide a neural network with the desired output (or response) for learning. In this chapter, the supervised learning is considered because the filter designer can see the input and output relationship of the filters.

The MFNs can be trained by a nonlinear mapping between many inputs and outputs through the supervised learning method. The most popular learning algorithm of MFNs is the back propagation algorithm developed by Rumelhart et al. (1986). The back propagation algorithm for training the designed neural network is repeated until the network reaches a certain pre-defined threshold by minimizing the difference between the neural network outputs and the desired outputs (see Appendix B for the detailed derivation of the back propagation algorithm).

4.2.2 Neural Network Aided Adaptive Filtering

Among the many environmental factors affecting the performance of the IMU such as temperature, air pressure, noise of platform (engine vibration) and platform maneuver, it is noted that the platform maneuver is the dominant factor to the performance of IMU (Wang et al, 2006; Wang et al., 2007). In the proposed neural network (NN)-aided

adaptive filtering method for INS/GPS integration, an effort is made to adaptively adjust the filter according to the platform maneuvers.

The principal idea of this section is the hybrid method of the traditional adaptive covariance estimation aided by a neural network trained on given platform dynamics. The Kalman filter estimates the navigation errors in position, velocity and attitude using external control. At the same time, the neural network is trained to map a relationship between the platform dynamics (the input) and the Kalman filter estimations (the desired output). The key to neural network aiding is the design of the network. The three basic components for the neural network design are architecture, input and output and neural network training.

Neural Network Architecture: The multi-layered feed-forward neural network (three layers) is applied to aid the adaptive version of filters (AEKF and AUKF) for the INS/GPS system. The usual way to decide on the appropriate number of hidden neurons is empirical; however, see also Bishop (1995); and Haykin (1999). This means that, many candidate networks having different numbers of hidden neurons should be tested to determine the one with the best performance.

In other words, there is no unique solution to a given data set and there is always a chance to obtain a better solution (Haykin, 1999; Wang, 2006; Li, 2008). Our laboratory tests indicate that optimal geolocation results are obtained with 16, 24, and 15 neurons, respectively, in the three layers, where sigmoid transfer functions are used in the first and second layers and the third layer is linear.

Neural Network Input and Output: The input comprises changes in velocity ($\Delta v_N, \Delta v_E, \Delta v_D$) in a local north-east-down coordinate frame, and Euler angles, ϕ, θ, ψ, for the platform attitude, and their changes, $\Delta\phi, \Delta\theta, \Delta\psi$. These input parameters of the neural network are selected to represent the platform dynamic variation. The Euler angles are determined from the gyro data and the changes in these and in the velocity are calculated from the *last* measurement update to the *current* measurement update:

$$\Delta v_N = v_{N,k+1} - v_{N,k}, \Delta v_E = v_{E,k+1} - v_{E,k}, \Delta v_N = v_{D,k+1} - v_{D,k}, \tag{4.19}$$

$$\Delta\phi = \phi_{k+1} - \phi_k, \quad \Delta\theta = \theta_{k+1} - \theta_k, \quad \Delta\psi = \psi_{k+1} - \psi_k, \tag{4.20}$$

where k is the measurement update index.

Wang et al. (2006 and 2007) suggested that rapid changes in the heading angle can disturb the training of the neural network. However, in our laboratory test, training including the heading angle produced better results than training without the heading angle because this angle clearly identifies the dynamic maneuvering of the platform. Figure 4.5 shows the training result with considering of heading angle in the NN input. Figure 4.4 show the high correlation between change of heading angle and the turning segment of the trajectory.

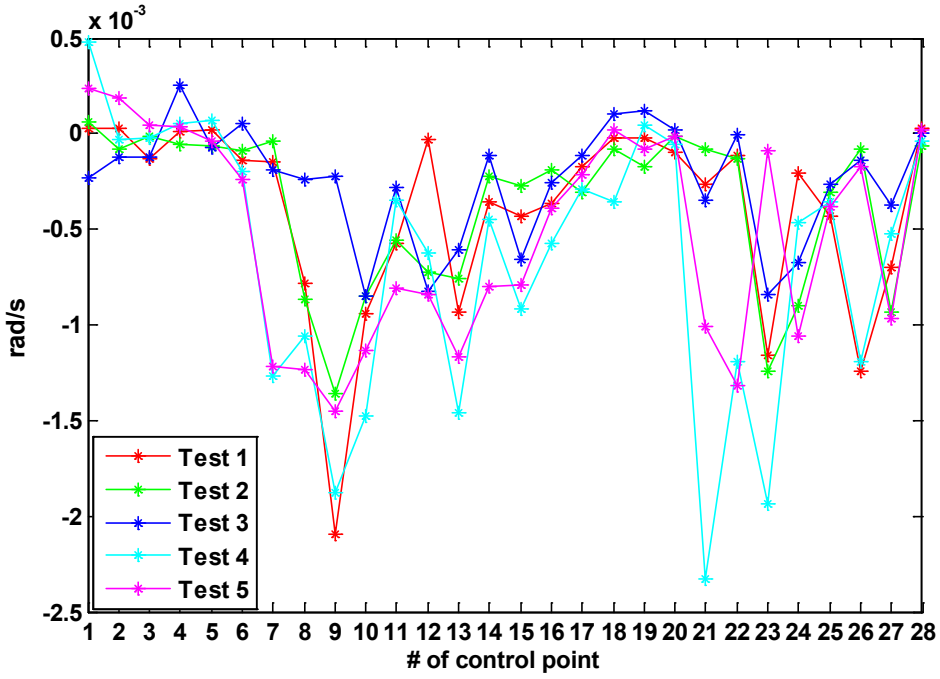

Figure 4.4. The change of heading angle in five laboratory test (The control point in the turning segment are 8,9,10, 13,14,15, 22,23,24, 27,28,1, see Figure 4.8).

For the neural network's desired outputs, we select the innovations of the Kalman filter, given by equation (3.19). For the unscented Kalman filter the desired output of the neural network is $y_k - \hat{y}_k^-$ (innovation which is difference between measurement and its expected value where y_k is the measurement and $\hat{y}_k^-$ is the expected value see table (3. 1)).

Neural Network Training Strategy: If measurements (external control points) are available, the neural network is trained at the control update rate using all available input and desired output values until it reaches a certain pre-defined error (threshold). The weights and biases of the network were adjusted iteratively using the Levenberg-Marquardt algorithm to minimize the differences between the *computed* output (by neural network) and the *desired* output (innovations of filters is selected in this test) (Chiang, 2004; Wang et al., 2006).

When measurements are not available (during a GPS outage), the computed output of the neural network (the estimated innovations) is used (or aided) to determine the process noise covariance (GQG^T) according to equations (4.5) and (4.6).

In the laboratory tests, the neural network does not have enough training data from the first few control points, and the process noise (Q) is estimated initially by the traditional adaptive filtering method (equation (4.6)). However, after four or five control points NN is able to learn from the filter output.

Neural Network Training Results: The neural network was trained using the batch training method because it has been shown to be more accurate and have better convergence. A set of neural network inputs is used to train the multi layer neural network by changing its weights and biases using the combination of trial-and-error method and the least square methods of model in equation (4.10). That is, the parameters of neural network are changed if the individual neural network input set is available at an epoch.

Figure 4.5 shows an example of the training results for a multi-layered neural network using the HG1700 in a laboratory test (first of five tests). The horizontal axis shows the number of control points in the trajectory (Figure 4.8). First, the innovation sequence of the Kalman filter (target of the neural network) was computed at eight control points. Second, the neural network was trained using *six* neural network input sets and then simulated at the seventh and eighth innovation sequence (estimated output by trained network). Figure 4.5 shows that the neural network output is close to its target up to the sixth control point (see Figure 4.4), but it starts to diverge after the seventh control point, showing a higher difference between KF estimated and NN output at the eighth control point. Thus, the neural network training can provide accurate prediction only for one or (at a maximum) two control points during GPS outages.

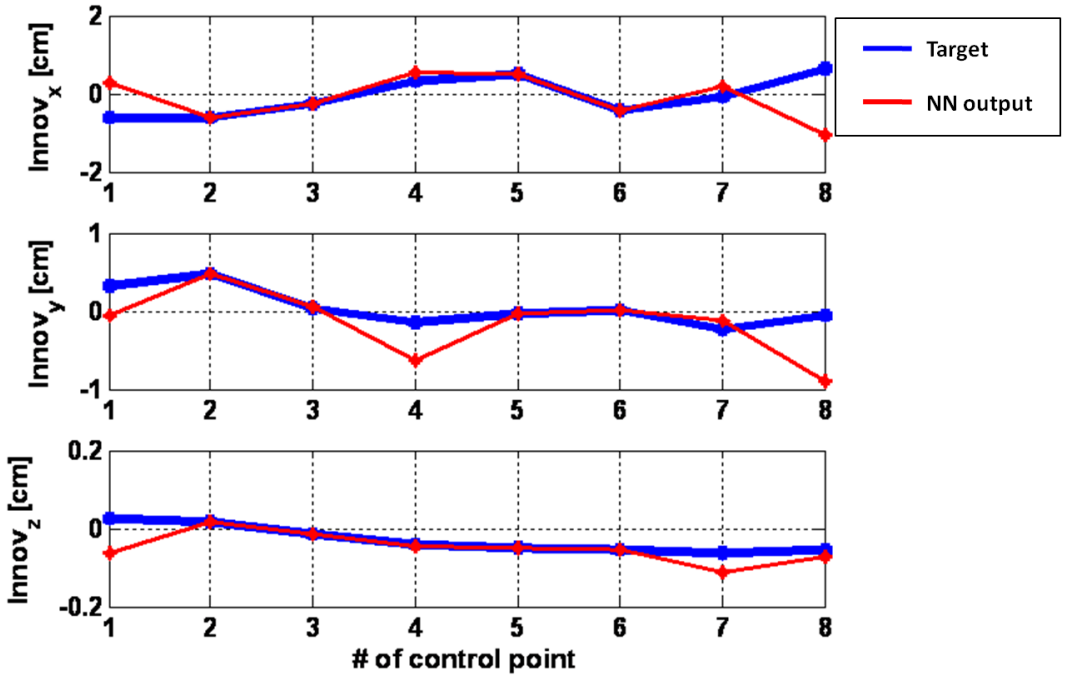

Figure 4.5. The example of the neural network training results (Control points refer to that of Figure 4.4.).

4.2.3 Neural Network Aided Adaptive Smoothing

The Rauch-Tung-Striebel (RTS) fixed-interval smoother was combined with the aforementioned adaptive forward filters, yielding the adaptive Extended Kalman Smoother (AEKS), the adaptive Unscented Kalman Smoother (AUKS, also called as Unscented RTS Smoother, (Sarkka, 2008)), the neural network aided adaptive EKS (NN-AEKS) and neural network aided adaptive UKS (NN-AUKS). Figure 4.6 shows the flow of the neural network aided adaptive filtering and smoothing.

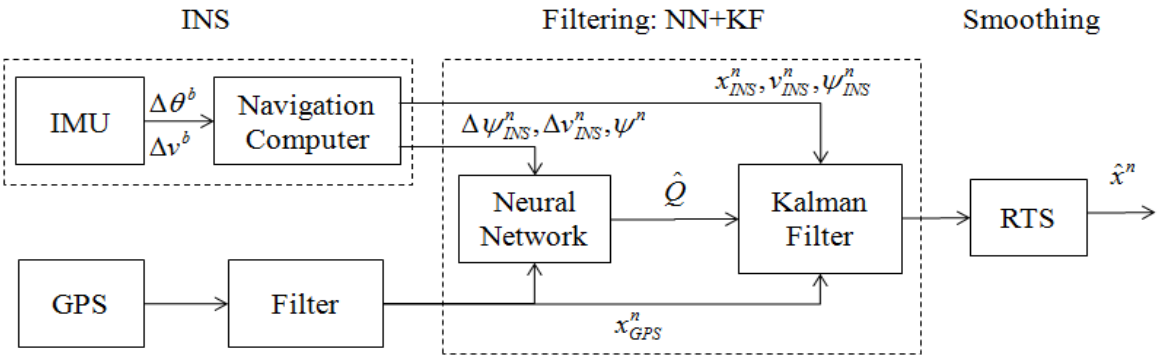

Figure 4.6. Loosely-coupled, decentralized INS/GPS integration.

4.3 LABORATORY TESTS

4.3.1. Cart Based Geolocation System (CBGS)

The adaptive filter/smoothers (AEKF and AUKF), and the neural-network aided adaptive filter/smoothers (NN-AEKS and NN-UKS) were tested in the laboratory using IMUs mounted on a cart. The state vectors for the filters are the same as these for the simulation test in chapter 3.

This cart-based system contains three Honeywell IMUs (the H764G navigation-grade IMU, and two tactical-grade IMUs, the HG1700 and the HG1900), along with IMU data collection computer hardware and a physical pointer used to identify the cart's passing or occupation of a control point (Figure 4.7). This pointer served a function similar to an external position observation (such as from GPS). The error specifications of the three IMUs as provided by the manufacturer are described in Table 4.1. These specified error parameter values are employed to generate the initial covariance matrix of the measurement noise (P_0) and the initial covariance matrix of the system noise (Q). The constant accelerometer bias of the H764G is about 50 times smaller than for the medium-grade units and its constant gyro biases are similarly much smaller. The HG1700 gyros are more accurate than those of the HG1900 in terms of bias uncertainty (HG1700 and HG1900 have the same accelerometers). The HG1900 is also known as a MEMS (micro-electro-mechanical-sensor) IMU, incorporating fiber-optic gyros, whereas the other two IMUs use more expensive (and accurate) ring-laser gyros. Note, however, that although the HG1900 is called MEMS, it is much more accurate than the commercial grade MEMS IMUs.

		H764G	HG1700	HG1900
Accel Error	Bias	20 μg	1 mg	1 mg
	Scale Factor	40 ppm	300 ppm	300 ppm
	Random Walk	0.003 $(m/s)/\sqrt{hr}$	0.09 $(m/s)/\sqrt{hr}$	0.09 $(m/s)/\sqrt{hr}$
Gyro Error	Bias	0.01 deg/hr	1 deg/hr	<7 deg/hr
	Scale Factor	1 ppm	150 ppm	150 ppm
	Random Walk	0.001 deg/$\sqrt{hr}$	0.125 deg/$\sqrt{hr}$	0.09 deg/$\sqrt{hr}$

Table 4.1. The error specification of three IMUs.

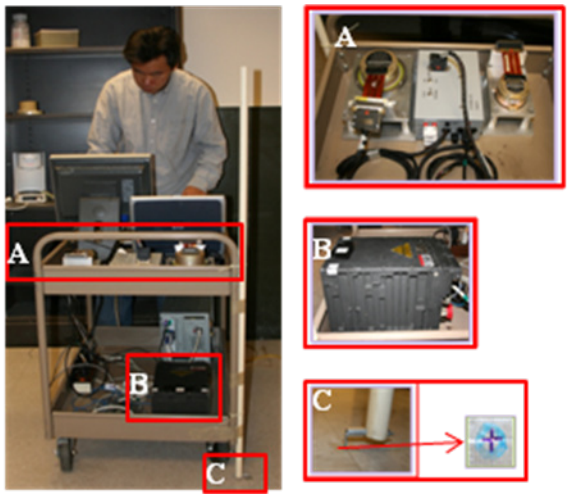

Figure 4.7. Cart Based Geolocation System, Front (A: HG1700 and HG1900 with Run-Box, B H764G, C: Pin Point Indicator with Mark).

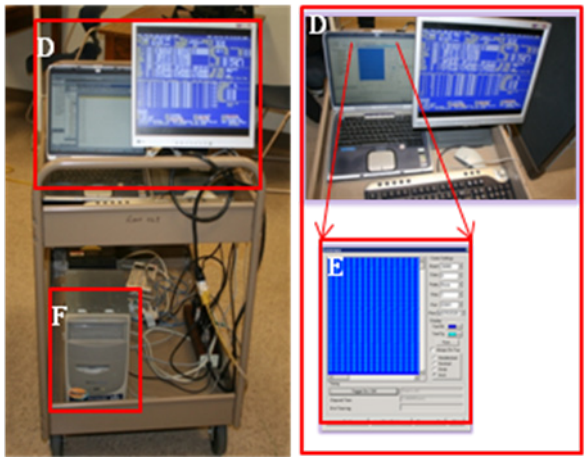

Figure 4.8. Cart Based Geolocation System, Back (D: Data collection software, E: Time tagging software, F: IMU data collection computer).

In the laboratory tests, simulated position updates are used as a manual coordinate registration system instead of integrating the IMU with a ranging system such as GPS. The cart was pushed along a trajectory with pre-defined waypoints that have known coordinates. Whenever the cart passed a particular waypoint, the event was recorded with a timing mark from the computer clock that also time-tagged the collection of data from the IMU. The imperfect recording of the passage of the cart pointer (Figure 4.7 C) over the ground marker could be considered an error in the control point coordinates, although it is a personal error and not as large in magnitude as a kinematic GPS position error. The magnitude of this error is estimated to be less than 1 cm per control point; however, the variance of the measurement error (diagonal matrix, R) was conservatively set to $(1cm)^2$. The test trajectory had four straight lines and four curved sections (Figure 4.9). Twenty-eight (28) ground marks were used as "measured" control points for the filtering/smoothing. The distance between points is 12 inches and the CBGS needed about 4 seconds to move from one control point to another. Therefore, the speed of the cart is about 0.076 m/s.

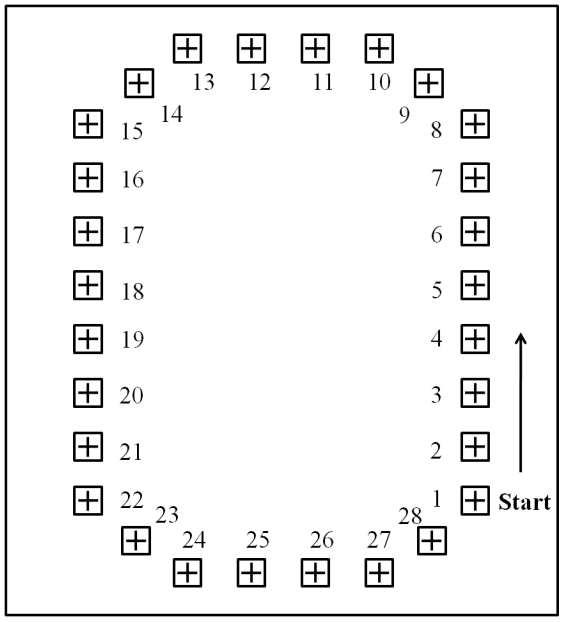

Figure 4.9. Laboratory test trajectory.

4.3.2. Test Result and Analysis

The CBGS was tested by comparing positioning solutions at control points not used in the integration. In the first case, every other point was used to update the system and the filtered/smoothed position estimate was compared to the skipped control. The total duration of inertial positioning between control updates is about 8 seconds in this test. In the second case, every third point served as update and the estimated positions were compared to the coordinates of the two skipped points. The total simulated GPS outage

in this case is about 12 seconds.

The filtered/smoothed position errors with or without neural-network aiding were analyzed along the straight and curved sections, respectively, in terms of the standard deviation of the total 3-D position error computed from 5 separate tests along the same trajectory. In the first case, there are 8 (6) comparison points in the straight (curved) segments, hence 40 (30) comparisons contribute to the standard deviation of the error. In the second case, the corresponding number of comparisons is 45 for both straight and curved segments.

Figures 4.10 and 4.12 show the standard deviations of position errors (see Equation (3.86), N is 8 (6) in the straight (curved) segments) of five separate tests according to the different IMUs, the various filtering/smoothing methods, and the interval between control updates. Figures 4.11 and Figure 4.13 show the standard deviation of five tests (see Equation (3.86), N is 40 (30) in the straight (curved) segments) with two control point updates (Figure 4.10) and three control point updates (Figure 4.12). Figures 4.14 and 4.16 show the corresponding standard deviations of five different tests when the neural-network-aided-adaptive filter/smoothers were applied. Figures 4.15 and Figure 4.17 show the standard deviation of Figure 4.14 and Figure 4.16. As expected, the navigation-grade IMU (HG764G) performs best. Also, the non-linear based smoothing method (AUKS) yields better results than the EKF-based smoothing method, especially in the turning segments. The HG1900 performs only slightly worse than the HG1700. The relative difference in performance between the tactical or medium grade IMUs (HG1700 and HG1900) and the navigation-grade IMU in these tests decreased significantly using the non-linear filtering techniques. The position error of the HG764 with the nonlinear filter/smoother (control updates every 2 points) decreased 42% in the straight section and 31% in the turning section. In the HG1700 and HG1900 case, the position error decreased 54% in the straight and 52% and 49% in the turning section.

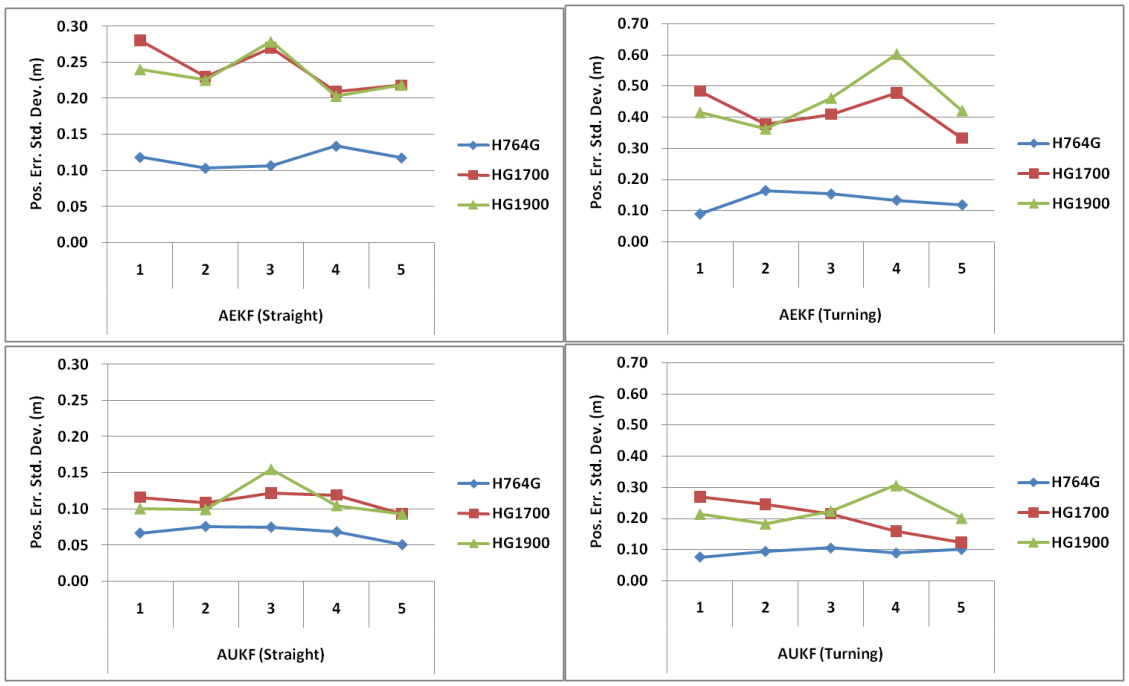

Figure 4.10. The Standard Deviation of Position Error of five separate tests according to different IMUs and Adaptive Filtering/Smoothing methods (control updates every 2 points).

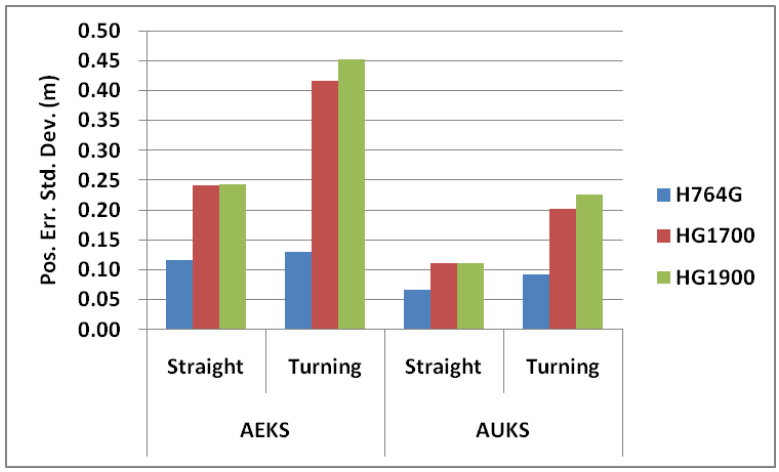

Figure 4.11. The Average Standard Deviation of Position Errors according to different IMUs and filtering/smoothing methods (control updates every 2 points).

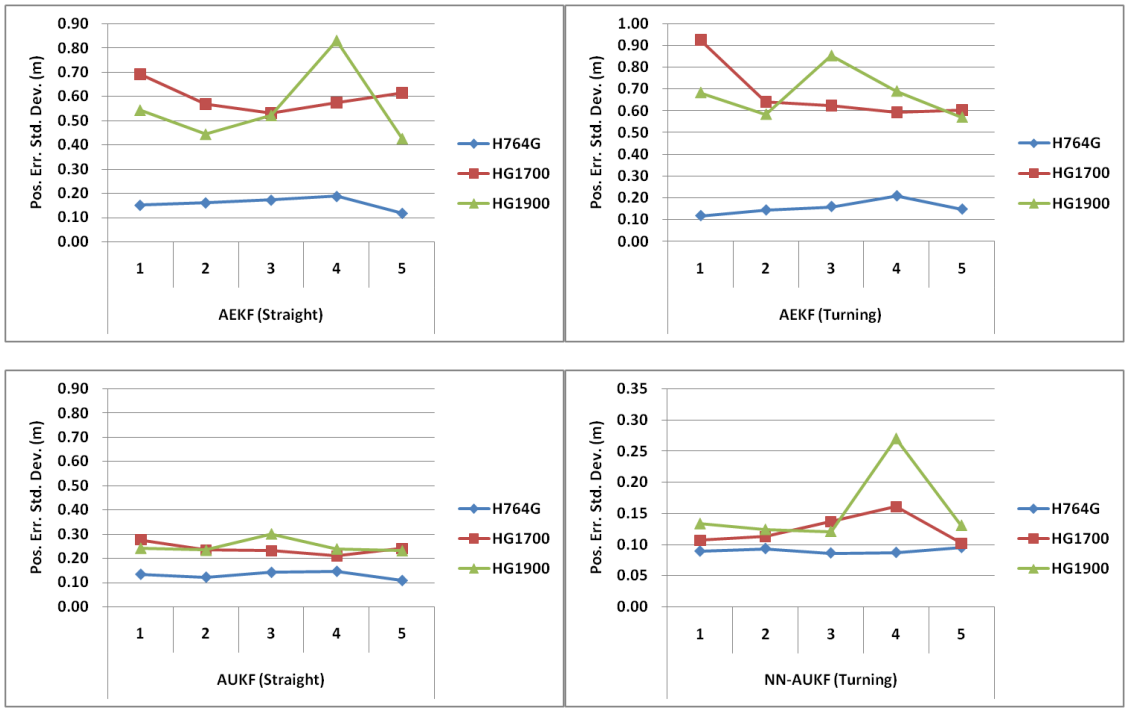

Figure 4.12. The Standard Deviation of Position Error of five separate tests according to different IMUs and Adaptive Filtering/Smoothing methods (control updates every 3 points).

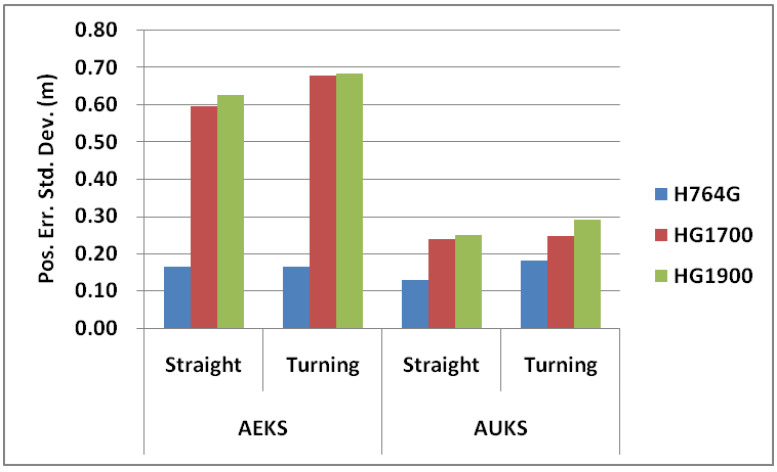

Figure 4.13. The Average Standard Deviation of Position errors according to different IMUs and filtering/smoothing methods (control updates every third point).

Similar to the two-point update case, in every three-point update case the H764G achieved the best position accuracy; and, the nonlinear, adaptive filter/smoothing techniques demonstrated better performance than the AEKS. However, compared to the first case, there was less difference with both method (AEKS and AUKS) between the straight and turning segments because the accumulation of IMU errors overwhelmed the superiority of the nonlinear filter in a dynamic environment. On the other hand, the non-linear filter still achieves better estimates of states in an essentially non-linear system. The overall position accuracy was improved by including the neural network aiding, and the disparity in performance between straight and turning sections was reduced. It is noted that the position error of the NN-AEKS decreased dramatically compared to the AEKS in both straight and curved section (e.g. HG764 case; position error is decreased 50% in straight section and 44% in turning section, HG1700 case; 40% in straight and 44% in turning section, , HG1900 case; 44% in straight and 34% in turning section). The H764G with NN-aided, adaptive filtering/smoothing can achieve the area-mapping position requirement (5 cm) along straight sections with 8 seconds between updates. The position error (st. dev.) of the H764G is less than 10 cm in this case, but in particular, the HG1700 and HG1900 yielded only slightly worse results (1~3cm more in standard deviation). With the increased interval between control points the NN-aided, adaptive filter/smoother was able to maintain the position accuracy better than the unaided adaptive filter/smoother.

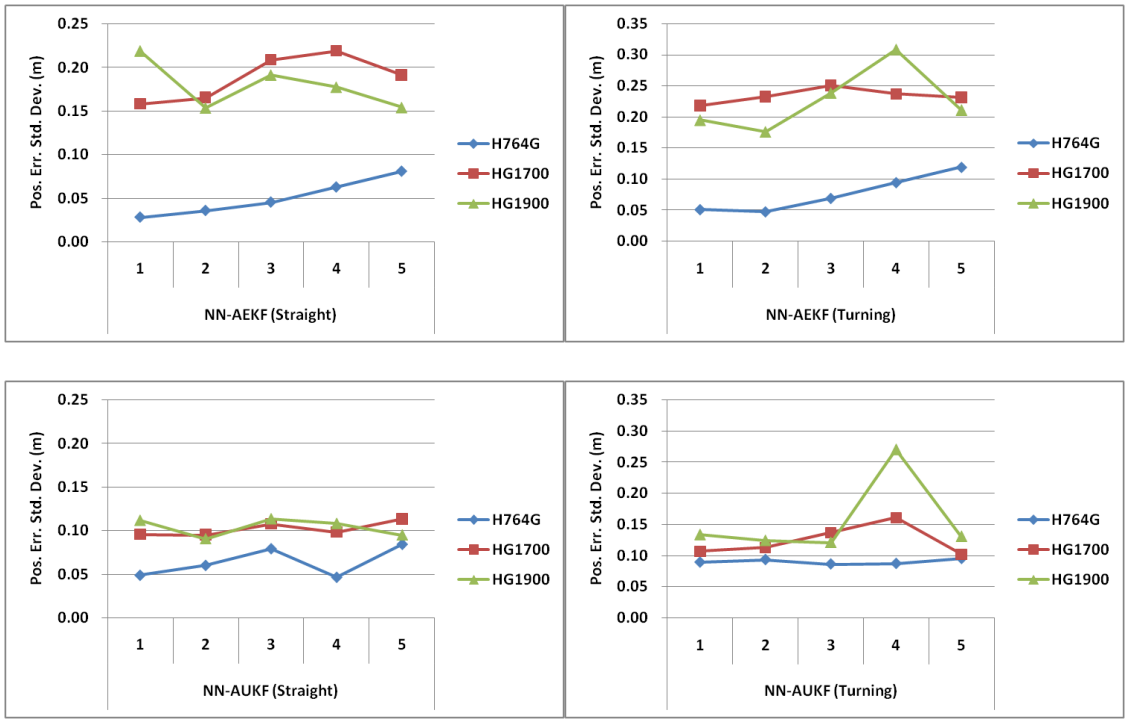

Figure 4.14. The Standard Deviation of Position Error of five separate tests according to different IMUs and Neural Network Aided Adaptive Filtering/Smoothing methods (control updates every 2 points).

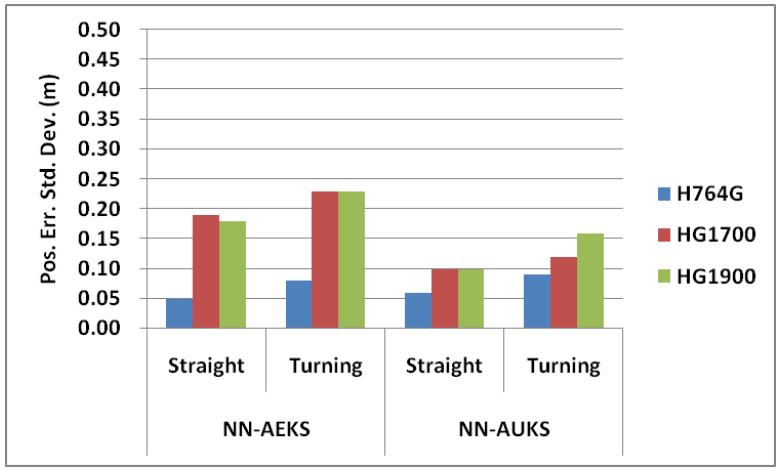

Figure 4.15. The Standard Deviation of Position Error according to different IMUs and NN aided filtering/smoothing method (control updates every 2 points).

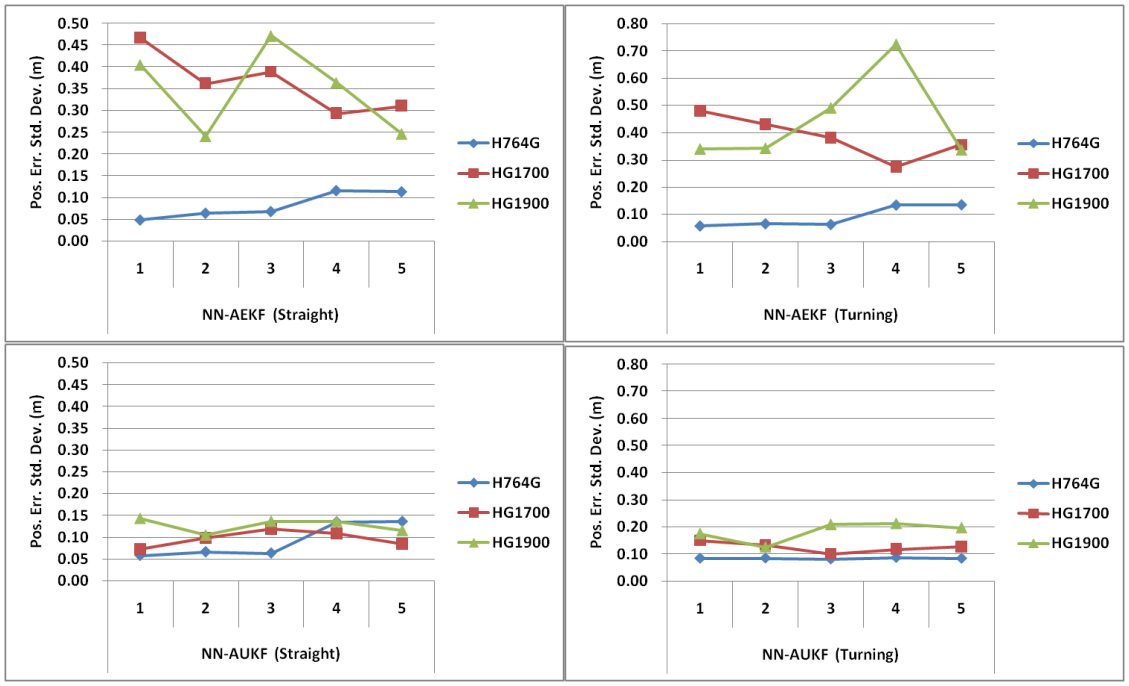

Figure 4.16. The Position Error Standard Deviation of five separate tests according to different IMUs and Neural Network Aided Adaptive Filtering/Smoothing methods (control updates every third points).

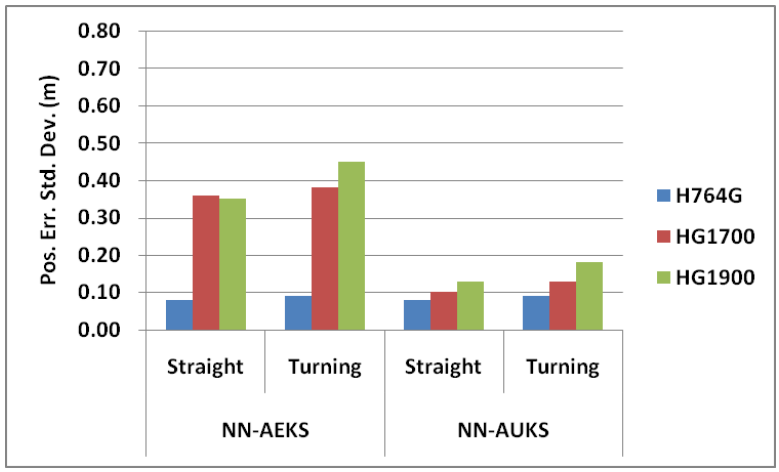

Figure 4.17. The Standard Deviation of Average Position Error according to different IMUs and NN aided filtering/smoothing method (control updates every third point).

4.3.3. Summary

In this chapter, both non-linear Kalman filters/smoothers and adaptations based on neural network-aiding were studied for the locally precise geolocation of UXO detectors. Laboratory tests were conducted using IMUs with different capabilities and along trajectories with different dynamics. The positioning performance was evaluated for both linear and non-linear, as well as adaptive and neural-network-aided adaptive Kalman filter/smoothers. As expected, the nonlinear smoothers, developed from a combination of adaptive unscented Kalman filter and RTS smoother (AUKS) yield superior performance over the standard adaptive extended Kalman smoother (AEKS).

Each neural-network-aided, adaptive filter/smoother improved the overall positioning accuracy for both benign and more dynamic trajectory segments in the test. The navigation-grade IMU (H764G) achieved the area-mapping accuracy level (5 cm) required for UXO detection and discrimination along straight segments and control gaps of 8 seconds. However, the medium grade IMUs (HG1700 and HG1900) performed well (~10 cm) under the same circumstances and using the NN-aided, adaptive non-linear filter/smoother (NN-AUKS). In addition, the neural-network-aiding tends to decrease the *difference* in performance between benign and dynamic components of the trajectory. From the simulation test in chapter 3 and the laboratory test in this chapter, it is clearly noted that the nonlinear estimation methods perform at least as well or better in any given situation and the neural-network aided adaptive filtering improved the overall position accuracy quite clearly.

CHAPTER 5: RAO-BLACKWELLIZED PARTICLE FILTERING

The final proposed integration algorithm is a combination of linear filtering (EKF) and nonlinear, also non-Gaussian filtering, (PF) in the Rao-Blackwellized Particle Filter (RBPF, also called Marginalized Particle Filter) framework. Although the RBPF was originally developed to overcome the inefficiency of the PF, it can be utilized for precise UXO geolocation because it may yield more accurate estimates than the PF and it provides a basic frame to apply various filtering methods (Doucet et al., 2001; Nordlund, 2002). In this chapter, the defined states (section 3.4.1) are divided into the linear and nonlinear states according to the two proposals and each proposal is thoroughly analyzed using the laboratory dataset.

5.1 Rao-Blackwellized Particle Filter (RBPF)

To overcome the computational inefficiency of the PF, the states can be divided into two sub sets which are estimated by the linear filter (Kalman filter) and a nonlinear (non-Gaussian) filter, respectively. This type of filter is called the Rao-Blackwellised particle filter (RBPF). The RBPF takes advantages of the linear and Gaussian state vector of the system model and applies to them the Kalman Filter. The remaining state variables, which suffer from severe nonlinear and/or non-Gaussian structure, are solved using the particle filter. Based on Bayes' rule the solutions from the two filters are fused. For the system and measurement model with additive noise case, if the state x_k can be partitioned into nonlinear, x_k^1, and linear part, x_k^2, the system and measurement model (equations (3.3) and (3.4)) can be rewritten as

$$x_{k+1}^1 = f^1\left(x_k^1\right) + F_k^1 x_k^2 + G_k^1 w_{k+1}^1 \tag{5.1}$$

$$x_{k+1}^2 = f^2\left(x_k^1\right) + F_k^2 x_k^2 + G_k^2 w_{k+1}^2 \tag{5.2}$$

$$y_k = h\left(x_k^1\right) + H_k \cdot x_k^2 + v_k \tag{5.3}$$

The pdf for the system noise vector is assumed to have zero mean and to be Gaussian with known covariance matrix

$$w_k = \begin{pmatrix} w_k^1 \\ w_k^2 \end{pmatrix} \sim N\left(\begin{pmatrix} 0 \\ 0 \end{pmatrix}, \begin{pmatrix} Q_k^1 & M_k \\ M_k^T & Q_k^2 \end{pmatrix}\right) \tag{5.4}$$

where $M_k = E\left[\ w_k^1 \left(w_k^2\right)^T\ \right]$, $Q_k^1 = E\left[\ w_k^1 \left(w_k^1\right)^T\ \right]$ and $Q_k^2 = E\left[\ w_k^2 \left(w_k^2\right)^T\ \right]$.
By assuming w_k^1 and w_k^2 are uncorrelated (i.e. $M_k = 0$), the equation (5.4) can be

written as (for the correlated process noise case, $M_k \neq 0$, see the Nordlund (2002))

$$E\left[\begin{pmatrix} w_k^1 \\ w_k^2 \end{pmatrix}\begin{pmatrix} w_k^1 \\ w_k^2 \end{pmatrix}^T\right] = \begin{pmatrix} Q_k^1 & 0 \\ 0 & Q_k^2 \end{pmatrix} \tag{5.5}$$

The measurement noise is a white noise process distributed as Gaussian with zero-mean and covariance matrix (equation (3.13))

$$v_k \sim N(0, R_k) \tag{5.6}$$

The pdf for x_0^2 is assumed to be Gaussian and the pdf for x_0^1 is known but arbitrary. To compute the filtering posterior pdf, we estimate $p(x_k \mid y_{0:k}) = p(x_k^1, x_k^2 \mid y_{0:k})$ recursively, starting with the pdf $p(x_{0:k}^1, x_k^2 \mid y_{0:k})$, where $x_{0:k}^1 = \{x_0^1, \cdots, x_k^1\}$ and $y_{0:k} = \{y_0, \cdots, y_k\}$.
Using the chain rule for Bayes' rule, this pdf can be factored into two parts according to

$$p(x_{0:k}^1, x_k^2 \mid y_{0:k}) = p(x_k^2 \mid x_{0:k}^1, y_{0:k}) p(x_{0:k}^1 \mid y_{0:k}) \tag{5.7}$$

Step 1 (solve $p(x_{0:k}^1 \mid y_{0:k})$): The second pdf on the right hand side of (5.7) can be rewritten recursively using Bayes' rule (refer equation (3.41)) repeatedly according to

$$p(x_{0:k}^1 \mid y_{0:k}) = \frac{p(y_k \mid x_k^1) p(x_k^1 \mid x_{0:k-1}^1)}{p(y_k \mid y_{0:k-1})} p(x_{0:k-1}^1 \mid y_{0:k-1}) \tag{5.8}$$

Because of the nonlinear state and measure equations for x_k^1, the particle filter is applied to solve (5.8) (see section 3.2.3 for more details about the particle filter).
For each $i = 1, \ldots, N$ (N is the total number of particles) the (measurement) update step of the particle filter is started from the conditional density (Equation (3.41)), $p(y_k \mid x_k^{1,i})$.
The proposal distribution for the particle filter is chosen as $p(x_k^1 \mid x_{0:k-1}^1, y_{0:k-1})$ similar to equation (3.38) and then the particles will be sampled according to $p(x_k^{1,i} \mid x_{0:k-1}^{1,i})$.
The recursive importance weight is calculated recursively as follows (see eq. 3.37)

$$\omega(x_{0:k}^1) = \omega(x_{0:k-1}^1) \frac{p(y_k \mid x_k^1, y_{0:k-1}) p(x_k^1 \mid x_{k-1}^1, y_{0:k-1})}{q(x_k^1 \mid x_{k-1}^1, y_{0:k})} \tag{5.9}$$

If the estimate of the effective number of particles (n_{eff}, in equation (3.40)) is less than the threshold, the adaptive resampling is performed.

The time update of particle filter is typically given by

$$\begin{aligned}\hat{x}_{k+1}^1 &= f_k^1\left(x_k^1\right)+F_k^1 x_k^2 \\ P_{k+1}^1 &= F_k^1 P_k^1 \left(F_k^1\right)^T + Q_k\end{aligned} \tag{5.10}$$

For each $x_k^{1,i}$ the Kalman filter is applied to estimate $\hat{x}_k^{2,i}$ and $P_k^{2,i}$ as follows.

Step 2 (solve $p\left(x_k^2 \mid x_{0:k}^1, y_{0:k}\right)$in equation (5.7)): Since we already obtained $x_k^{1,i}$, we can solve $p\left(x_k^{2,i} \mid x_{0:k}^{1,i}, y_{0:k}\right)$ for $i = 1,\ldots,N$. The following equations summarize the steps to estimate each $p\left(x_k^{2,i} \mid x_{0:k}^{1,i}, y_{0:k}\right)$ using Kalman filter measurement and time update step. .

If the measurements $y_{0:k}$ are independent of x_k^2 given x_k^1, $p\left(x_k^2 \mid x_{0:k}^1, y_{0:k}\right)$ can be rewritten as

$$p\left(x_k^2 \mid x_{0:k}^1, y_{0:k}\right) = p\left(x_k^2 \mid x_{0:k}^1\right) \tag{5.11}$$

Let $z_k^1 = x_{k+1}^1 - f\left(x_k^1\right)$ and $\bar{y}_k = y_k - h\left(x_k^1\right)$; then the system of equations (5.1)~(5.3) are

$$z_k^1 = F_k^1 x_k^2 + G_k^1 w_k^1 \tag{5.12}$$

$$x_{k+1}^2 = F_k^2 x_k^2 + G_k^2 w_k^2 + f^2\left(x_k^1\right) \tag{5.13}$$

$$\bar{y}_k = H_k \cdot x_k^2 + v_k \tag{5.14}$$

The optimal solution of equations (5.11) and (5.12) can be obtained by Kalman filter because this system is linear and Gaussian. Because $z_{0:k}^1$ provides the same information as x_{k+1}^1 as far as x_k^2 is concerned, the pdf of (5.13) is Gaussian

$$x_k^2 \mid x_{0:k}^1 \sim N\left(\hat{x}_k^{2,-}, P_k^{2,-}\right) \tag{5.15}$$

where the estimates $\hat{x}_k^{2,-}$ and $P_k^{2,-}$ are computed by the Kalman filter (see the equation (3.14) and (3.15)).

The recursive estimates of $p\left(x_k^2 \mid x_{0:k}^1, y_{0:k}\right)$ which follow the Gaussian distribution are given by the Kalman filter

$$p\left(x_k^2 \mid x_{0:k}^1, y_{0:k}\right) = N\left(\hat{x}_k^2, P_k^2\right) \tag{5.16}$$

If a new measurement y_k is available, the pdf of equation (5.16) can be computed (see equation (3.7))

$$p\left(x_k^2 \mid x_{0:k}^1, y_{0:k}\right) = \frac{p\left(y_k \mid x_k^1, x_k^2\right) p\left(x_k^2 \mid x_{0:k}^1, y_{0:k-1}\right)}{\int p\left(y_k \mid x_k^1, x_k^2\right) p\left(x_k^2 \mid x_{0:k}^1, y_{0:k-1}\right) dx_k^2} \tag{5.17}$$

Based on the assumptions (linear and Gaussian) this relationship leads to the Kalman filter's measurement update step.

$$\begin{aligned} \hat{x}_k^2 &= \hat{x}_k^{2,-} + K_k\left(\bar{y}_k - H_k \hat{x}_k^{2,-}\right) \\ P_k^2 &= P_k^{2,-} - K_k\left(H_k P_k^{2,-} H_k^T + R_k\right) K_k^T \end{aligned} \tag{5.18}$$

where

$$K_k = P_k^{2,-} H_k^T \left(H_k P_k^{2,-} H_k^T + R_k\right)^{-1} \tag{5.19}$$

The next step is that x_{k+1}^1 is incorporated (if z_k^1 is available, from equation (5.10)), we can compute

$$p\left(x_k^2 \mid x_{0:k+1}^1, y_{0:k}\right) = \frac{p\left(x_{k+1}^1 \mid x_k^1, x_k^2\right) p\left(x_k^2 \mid x_{0:k}^1, y_{0:k}\right)}{\int p\left(x_{k+1}^1 \mid x_k^1, x_k^2\right) p\left(x_k^2 \mid x_{0:k}^1, y_{0:k}\right) dx_k^2} \tag{5.20}$$

The time update step of the Kalman filter which depends on x_{k+1}^1 is computed by

$$p\left(x_{k+1}^2 \mid x_{0:k+1}^1, y_{0:k}\right) = \int p\left(x_{k+1}^2 \mid x_{k+1}^1, x_k^1, x_k^2\right) p\left(x_k^2 \mid x_{0:k}^1, y_{0:k}\right) dx_k^2 \tag{5.21}$$

If we can assume that z_k^1 is a known input, the recursive estimate of time update is

$$p\left(x_{k+1}^2 \mid x_{0:k+1}^1, y_{0:k}\right) = N\left(\hat{x}_{k+1}^2, P_{k+1}^2\right) \tag{5.22}$$

where

$$\begin{aligned} \hat{x}_{k+1}^2 &= F_k^2 \hat{x}_k^2 + f^2\left(x_k^1\right) + K_k^1\left(z_k^1 - F_k^1 \hat{x}_k^2\right) \\ P_{k+1}^2 &= F_k^2 P_k^2 \left(F_k^2\right)^T + G_k^2 Q_k^2 \left(G_k^2\right)^T - K_k^1\left(G_k^1 Q_k^1 \left(G_k^1\right)^T + F_k^1 P_k^2 \left(F_k^1\right)^T\right)\left(K_k^1\right)^T \end{aligned} \tag{5.23}$$

and

$$K_k^1 = F_k^2 P_k^2 \left(F_k^1\right)^T \left(G_k^1 Q_k^1 \left(G_k^1\right)^T + F_k^1 P_k^2 \left(F_k^1\right)^T\right)^{-1} \tag{5.24}$$

5.2 Rao-Blackwellized Particle Smoother (RBPS)

For the smoothing version of the RBPF we can employ the same method as for the UPS. The UPS employed the unscented RTS algorithm to smooth each particle; and, the RBPF the uses the same unscented RTS algorithm to smooth each particle. The RTS smoother was applied to each of the mean and covariance histories of the particles $\hat{x}_{1:N}^{(i)}$, $P_{1:N}^{(i)}$, $i = 1,\ldots,N$ (N is the number of particles) to produce the smoothed mean and covariance $\hat{x}_{1:N}^{S}$, $P_{1:N}^{S}$.

5.3 TEST

5.3.1 Handheld Geolocation System (HGS)

In this test, the RBPF and the previously developed filters/smoothers (EKF/EKS, UKF/UKS, and UPF/UPS) are evaluated using a handheld geolocation system (HGS) with the same conditions of the laboratory test scenarios of chapter 4 (state vectors, loosely-coupled system, etc.).

For the first proposed division of system states in the RBPF, the position of the IMU/GPS platform, being essential parameters for successful UXO detection, are estimated by the PF and the other states related to the IMU errors are estimated by the Kalman filter. That is, the state vector is divided into two parts according to Nordlund (2002) and Hektor (2007) who argue that only position states (latitude, longitude, and height) are highly-nonlinear and all other states can be assumed as linear without significant loss in their simulations and Terrain-Aided airborne test flight. However, this state division is incorrect because not only the position error states but also the orientation and velocity error states experience high nonlinear dynamics in ground-based UXO detection system such as the Cart-based Geolocation System and Hand-held Geolocation system. The new proposal for state division is made in the next section and the comparison with the first proposal and other filters/smoothers will be shown in the section on test results.

The partition of state vector for the first proposal: part1: position errors, part2: velocity error, orientation error and bias and scale factors of gyro and accelerometer

$$x_k = \left[\left(x_k^1\right)^T \quad \left(x_k^2\right)^T \right] \tag{5.25}$$

where

$$\left(x_k^1\right)^T = \left[\delta\phi_k \quad \delta\lambda_k \quad \delta h_k\right]^T \tag{5.26}$$

$$\left(x_k^2\right)^T = \left[\varepsilon_1' \quad \varepsilon_2\right]^T \tag{5.27}$$

and

$$\varepsilon_1' = \left[\psi_N \quad \psi_E \quad \psi_D \quad \delta\dot{\phi} \quad \delta\dot{\lambda} \quad \delta\dot{h}\right]^T \tag{5.28}$$

$$\varepsilon_2 = \left[\delta\omega_{GN} \quad \delta\omega_{GE} \quad \delta\omega_{GD} \quad \delta a_{AN} \quad \delta a_{AE} \quad \delta a_{AD} \quad \kappa_{GN} \quad \kappa_{GE} \quad \kappa_{GD} \quad \kappa_{AN} \quad \kappa_{AE} \quad \kappa_{AD}\right]^T \tag{5.29}$$

where the bias error of the gyro and accelerometer is defined $\left[\delta\omega_{GN} \quad \delta\omega_{GE} \quad \delta\omega_{GD}\right]^T$

and $\begin{bmatrix}\delta a_{AN} & \delta a_{AE} & \delta a_{AD}\end{bmatrix}^T$ respectively. The scale factor error of the gyro and accelerometer is $\begin{bmatrix}\kappa_{GN} & \kappa_{GE} & \kappa_{GD}\end{bmatrix}^T$ and $\begin{bmatrix}\kappa_{AN} & \kappa_{AE} & \kappa_{AD}\end{bmatrix}^T$. The corresponding filter and smoother are denoted RBPF1 and RPBS1.

The second method of the division of states separates them into the navigation related states (position errors, velocity errors and orientation errors) and all other states (bias and scale factor of gyro and accelerometer) because the orientation states are nonlinear in highly dynamic environment of UXO detection survey and velocity states are (highly) correlated with nonlinear states (position and orientation). Thus, the equation (5.26) and (5.27) for the state vectors are changed as follows

$$\left(x_k^1\right)^T = \begin{bmatrix}\delta\phi_k & \delta\lambda_k & \delta h_k & \psi_N & \psi_E & \psi_D & \delta\dot{\phi} & \delta\dot{\lambda} & \delta\dot{h}\end{bmatrix}^T \tag{5.30}$$

$$\left(x_k^2\right)^T = \begin{bmatrix}\delta\omega_{GN} & \delta\omega_{GE} & \delta\omega_{GD} & \delta a_{AN} & \delta a_{AE} & \delta a_{AD} & \kappa_{GN} & \kappa_{GE} & \kappa_{GD} & \kappa_{AN} & \kappa_{AE} & \kappa_{AD}\end{bmatrix}^T \tag{5.31}$$

and the corresponding filter and smoother are designated RBPF2 and RBPS2.

The HGS has only one tactical-grade IMU (HG1900) for low-cost and low-weight purposes and is the designed with a new hardware interface and an automatic target tracking system to determine its position (Figure 5.1). The red circle on the front head of the HGS was used as a target that could be tracked for the accurate positioning of the HGS by using a real-time color image. This external tracked position served the same purpose as GPS in the field. . The error specifications of the HG1900 were described in Table 4.1. However, for this IMU, the bias of the gyro and accelerometer are estimated by coarse and fine calibration procedures (see Appendix B). The actually used values of the biases of the gyro and accelerometer are described in ` in Appendix B.

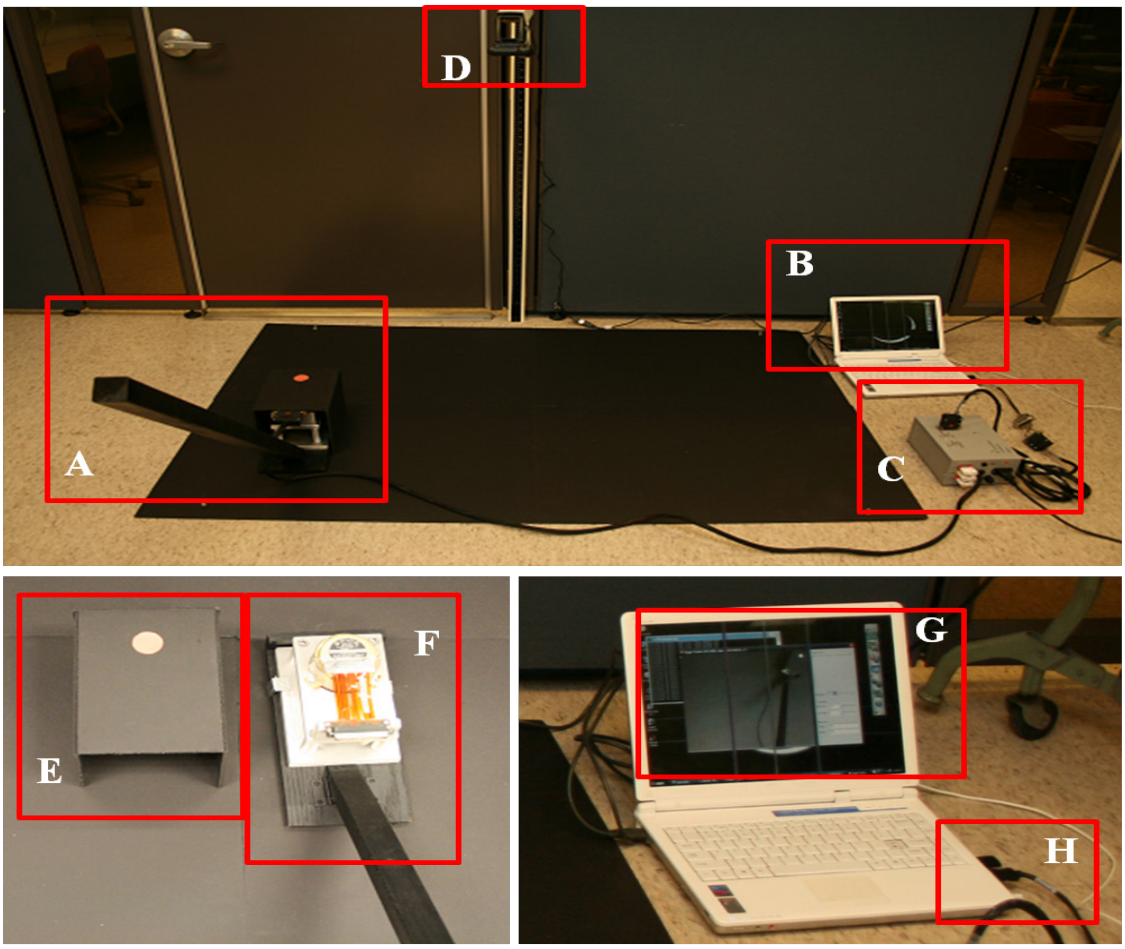

Figure 5.1. The new hardware system for Handheld Geolocation (A: Handheld Geolocation System, B: Laptop (Data collection system), C: Run-box, D: Logitech® Web Cam, E: Target (red dot) with black box, F: HG1900 in HGS, G: Target tracking software, and H: PCMCIA converter).

The previously used hardware system (see Figure 4.7 and Figure 4.8 in the chapter 4) has some limitations in terms of the flexibility and mobility because it requires a desktop computer with an ISA board (the ISA board slot is not supported in modern desktop systems) and a run-box for power. Also, the data collection software provided by Honeywell is only executable on the DOS operating system.

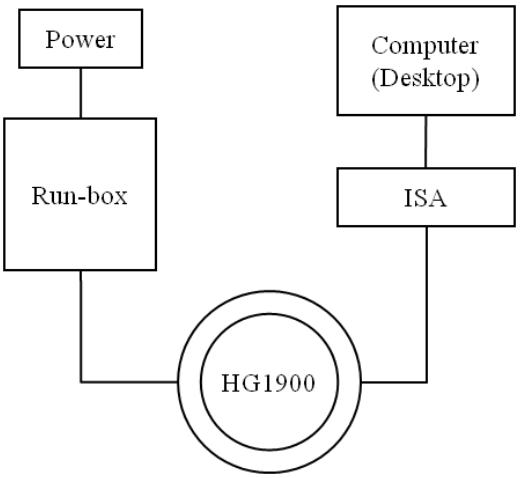

Figure 5.2. The block diagram of the Hardware System.

Therefore, the goal of the new hardware system is directed towards a compactness with flexibility (window based software) and mobility using PCMCIA converter and laptop (Figure 5.3). The PCMCIA converter eliminates the ISA board and enables the use of a laptop instead of a desktop computer.

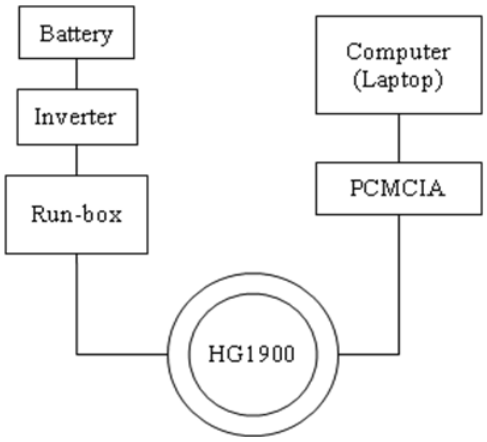

Figure 5.3. The block diagram of the New Hardware System.

Similar to the laboratory tests in chapter 4, the HGS is tested over a small area without GPS signal. Therefore, the position updates of the HGS are obtained by tracking the red target using the image of a webcam (at a 5Hz update rate, if we employ a more advanced laptop computer with USB 2.0 interface and Intel Core 2 Duo ® CPU, we can obtain up to 25~50Hz update rate in the positioning). In order to obtain accurate positions of HGS, an automatic target position extraction system is designed and implemented using the real-time color image.

This system has four main steps. First, the color image from the webcam is converted to a binary image which has only two values, 0 or 255, for each R, G, and B band. In this test, to facilitate the binary conversion only the R band was employed. Second, the object of *interest* (the target) in the binary image is labeled. Labeling is the procedure that collects each pixel into one (meaningful) region according to its size, geometric shape, and number of hole. After labeling, the connected-neighbor regions are numbered differently to discriminate them. The figure 5.4 shows the before and after labeling of the sample image.

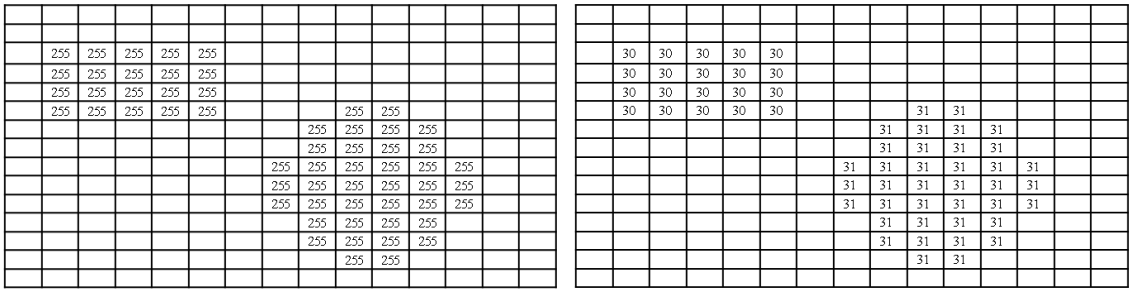

Figure 5.4. The binary image and labeled image (all empty cell are labeled zero).

Third, the labeled image is evaluated to extract the target object using geometric circularity and the size of target. Since our target is a circle (the circle is selected as the target shape because it is easy to detect), the distance from the center to the boundary will be almost constant. Thus, the target which has the least variation of the distance among other objects (such as a rectangle where the distance from the center to the boundary changes continuously (high variance)) will be selected (the employed threshold value for the variation of distance is less than 5 pixels, see Figure 5.5). Also, the size of the target is pre-defined to avoid confusion with small objects which could be regarded as noise. Therefore, if the size of the detected target is smaller than the pre-defined threshold value, it will be discarded (in this test, the threshold value for the size was 100).

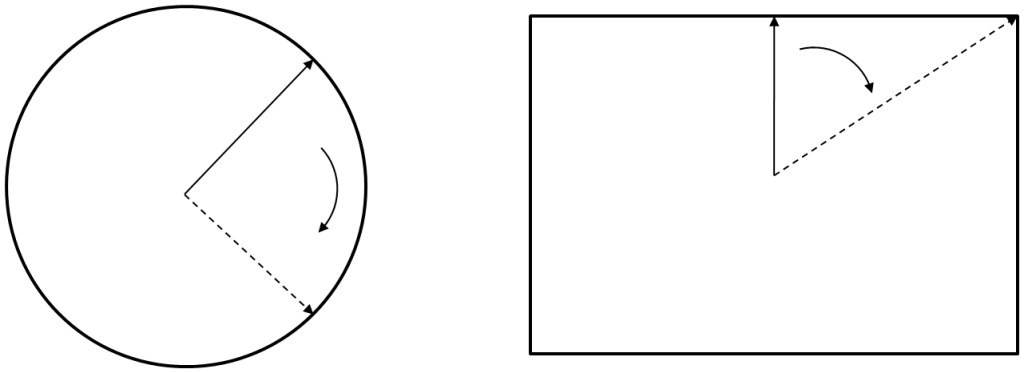

Figure 5.5. The geometric circularity.

Finally, the position (the center of the circle) of the extracted target is screen coordinates is converted to real world coordinates. Figure 5.6 shows the step-by-step flow of the automatic target position extraction using the real-time color image input from the webcam.

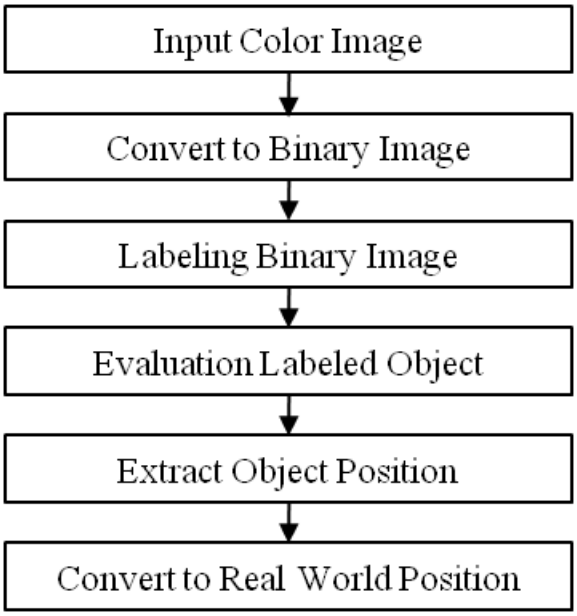

Figure 5.6. The flows of target position extraction.

Figure 5.7 shows the screen shot of the developed software (based on Visual C++ Development studio®) for the automatic target position tracking of the HGS. The current position (window coordinate system (resolution is defined as 640×480 [pixel])) of the HGS, computer time (unit: sec), and number of the target is presented in the caption of software. The transformed binary image from the color image is captured and displayed in the right-top section (binary view) with a pre-defined but adjustable threshold value determined with a slide bar (the pre-defined threshold value was 214 in the test environment). The two condition values (the minimum size of the target and the circularity) to differentiate the target from other objects are defined as 100 and 5, respectively. The actual map size (128cm*960cm) which was measured before the test will be used to convert the target position in the window coordinate system (640×480 [pixel]) to the computed position in the real-world system. Since the webcam (image) and actual map area (target area) are parallel, the actual dimension of one pixel is 0.2cm by 0.2cm.

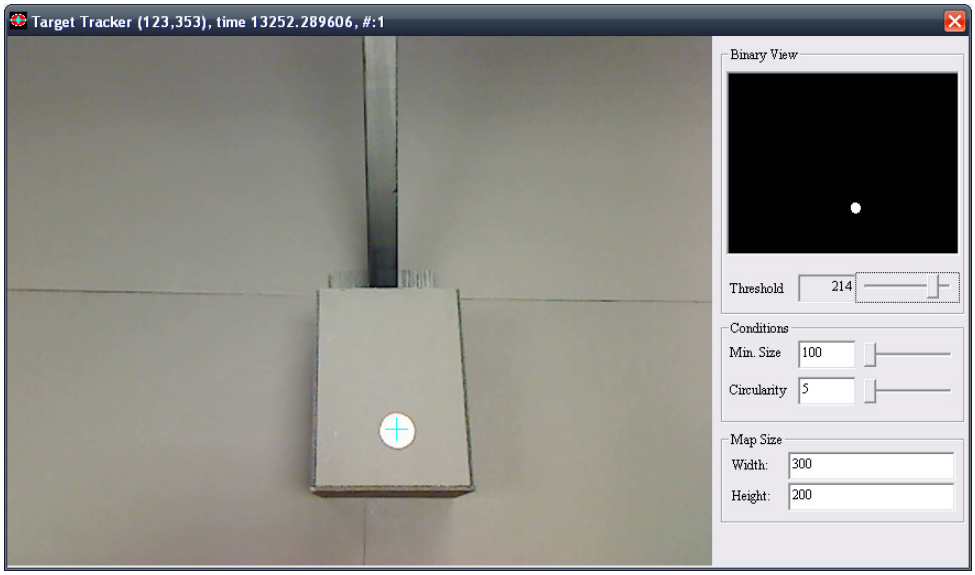

Figure 5.7. Target position tracking software.

The typical dynamics of a hand-held UXO detection platform can be classified into four categories; linear, curved, sweep, and swing (Bell and Collins, 2007). However, since the linear and curved sections are included in the sweep and swing dynamics, only two test trajectories (sweep and swing) are considered. The position accuracy of the HGS system will be tested along five sweep and five swing trajectories. The sweep trajectory has six straight lines and five curved sections. The swing trajectory has five straight lines and four curved sections. The total distance of sweep (swing) of the trajectory is about 0.72 (0.56) m and the HGS takes about 22 (14) seconds. Therefore, the speed of the HGS is about 0.033 (0.04) m/s, respectively. Figure 5.8 shows the trajectories of the five sweep and swing test.

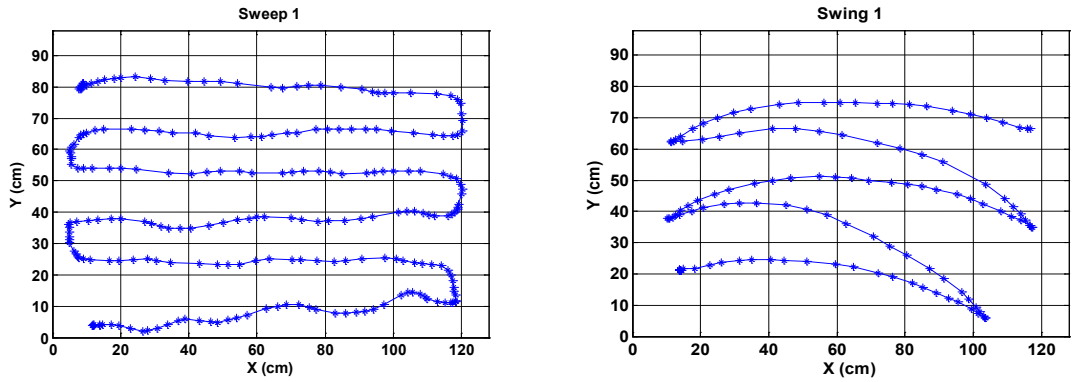

Figure 5.8. The five different trajectories (sweep and swing) of the designed handheld UXO detection platform. (Figure 5.8 is continued)

Figure 5.8 continued

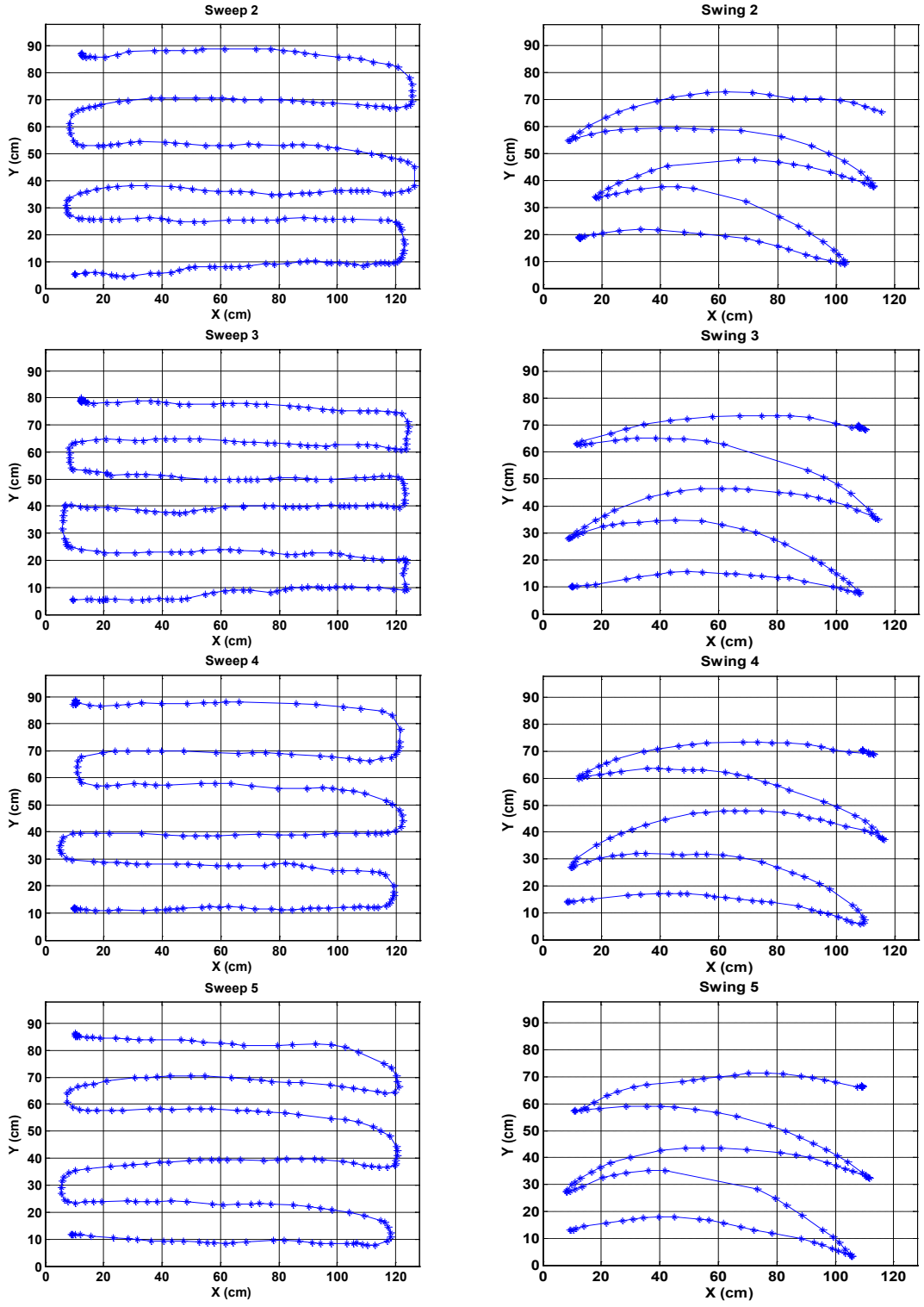

5.3.2 Test Result and Analysis

Various update intervals using the imaged target positions are implemented to compare the filtered/smoothed position estimates with the requirements of position accuracy for MEC geolocation and characterization. In each test case, 5Hz, 2.5Hz, 1Hz, 0.5Hz, and 0.25Hz update rates are employed in the integration. The position accuracy of the HGS was tested by comparing to the target positions which are not employed in the filtering process. For example, if the update rate of the control points is 1Hz, every fifth control point of the automatically tracked target position is used as external control in the filter and all other control points (four points) are employed to compare to the estimated points of the filter / smoother. The standard deviations of the total 2-D errors (The only horizontal part of Equation (3.86), $z_\sigma = \sqrt{z_{\phi,\sigma}^2 + z_{\lambda,\sigma}^2}$) of filtered/smoothed position (from the EKS, UKS, UKS, RBPS1, and RBPS2) were computed and analyzed in the straight and curved sections. The curved section is defined by a pre-defined threshold of absolute value of heading change angle ($\geq 20^\circ$).

Sweep Test: Figure 5.9 (left: straight, right: curved section) shows the standard deviations of the position errors in the five different tests according to the various filtering/smoothing methods and the five update intervals between control points. Figure 5.10 shows the average standard deviations of the error for each of the filters implemented and for each update rate of control points. The averages represent the results of the five separate sweep tests.

As anticipated, the nonlinear filter/smoothers perform better than the standard extended Kalman smoother both on straight and curved segments. In detail, in the straight section, the UKS, UPS, and RBPS2 can achieve the *discrimination* level of position accuracy (better than 2cm for standard deviation) from a 5Hz to a 0.5Hz update rates of the control points and can achieve the *area mapping* level of accuracy (better than 5cm for standard deviations) at a 0.25Hz update rate. The EKS and RBPS1 yield results at 0.5Hz slightly above the discrimination level of accuracy (2.26 cm and 2.32 cm as standard deviations and exceed the area mapping accuracy level when the update rate is 0.25Hz. In the curved section, every filter approached the discrimination level of accuracy (less than 2cm as std. dev.) up to 1Hz update rate and achieved 5cm (std. dev.) accuracy at 0.5Hz. The RBPS1 shows a better performance than EKS, but gets worse than other nonlinear filter-based smoother (UKS and UPS). Especially when the update rate is high (0.5Hz and 0.25Hz), the RBPS1 yields the worse results compared with the other nonlinear filters, but still is better than the EKS, especially for long intervals between control points. The RBPF2 gives a better performance than the RBPS1 in all update rates. Also, the position errors of the RBPF2 are comparable with the other nonlinear smoothers (UKS and UPS) up to 0.5Hz but slightly lower than all other smoothers at 0.25Hz. The RBPS2 gives superior performance when the external ranging solution is blocked or degraded for longer than 4 seconds. Therefore, the orientation and velocity states should be included in the nonlinear states for the RBPF because all navigation-related states (position, velocity, and orientation error states) experienced the high dynamic sweep operation, especially when the external ranging solution is not available.

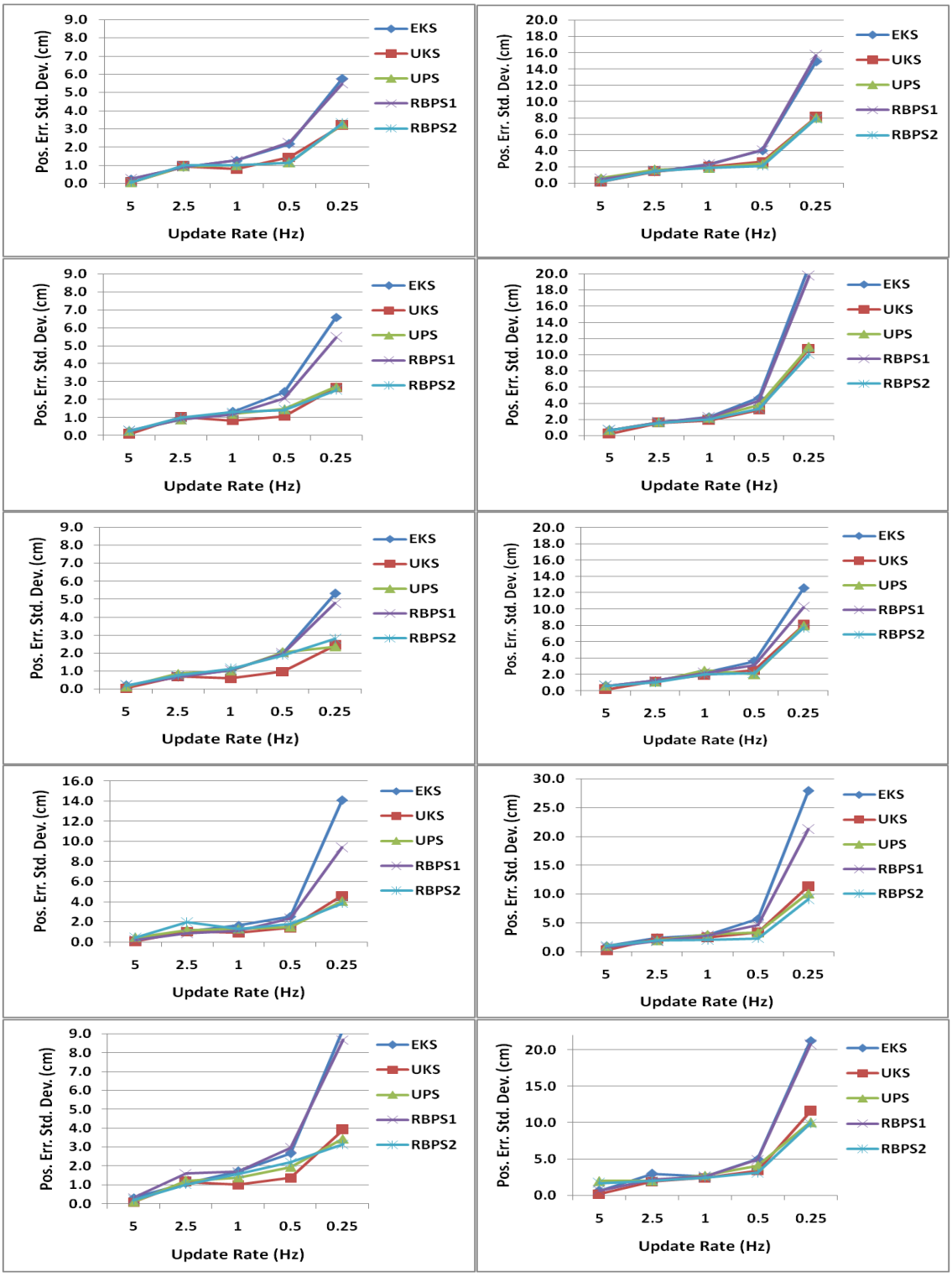

Figure 5.9. The standard deviation of position error in five separate sweep tests according to different smoothing methods (first column: straight section, second column: curved section, first row: test1, second row: test2, third row: test3, fourth row: test4, and fifth row: test 5) (unit: cm)

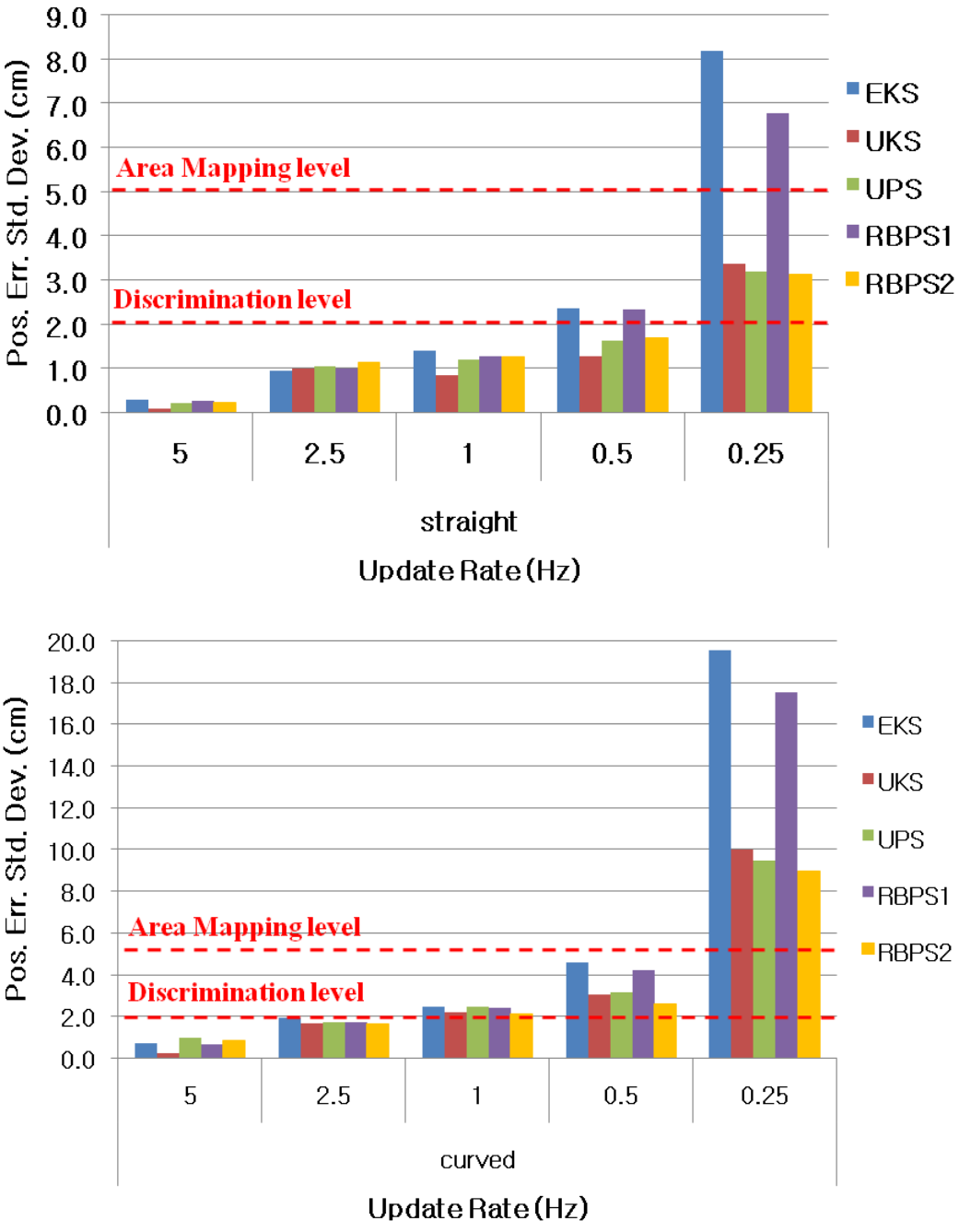

Figure 5.10. The average standard deviations of position errors according to various smoothing methods (first row: straight, second row: curved) (unit: cm).

Swing Test: Overall, the results of the swing test were worse than those from the sweep test, especially when the update rate is less than 1Hz. Similar to the sweep test, the non-linear filter/smoothing techniques demonstrated better performance than the EKS. However, compared to the sweep test, there was less of a difference between straight and curved sections in all estimation methods. Figure 5.11 shows the standard deviations of the position errors of the five different tests according to the various smoothing methods and the update interval between control points. Figure 5.12 shows the average standard deviations of position errors of the results in Figure 5.11. The position accuracy of the swing test was degraded compared with the sweep test, especially when the update rate is less than 1Hz in both straight and curved sections. However, it is noted that the position error of the UKS, UPS, and RBPS2 decreased at 0.25Hz when compared to the EKS and RBPS1 in the straight and curved sections.

In the straight section, the UKS, UPS, and RBPS2 attained the *discrimination* level of position accuracy up to the 1Hz update rate and achieved the *area mapping* level of accuracy at 0.5Hz update rate (compared to the sweep test where the update rates for the discrimination and area mapping level of accuracy were 0.5Hz and 0.25, respectively). The EKS and RBPS1 yields results above the discrimination level of accuracy at 0.5 Hz and the EKS also exceeded the area mapping accuracy at 0.5 Hz. In the curved section, similar to the straight section, the UKS, UPS, and RBPS2 achieved the discrimination level up to 1Hz and the area mapping level up to 0.5Hz. But the position error of the EKS and RBPS1 was over the discrimination level at 2.5Hz and was more than the area mapping level at the 0.5Hz.

In this swing test, the RBPF1 performs better than the EKS, but worse than the other nonlinear filter-based smoothers (UKS, UPS, and RBPS2) especially for long update intervals (0.5Hz and 0.25Hz). The RBPF2 performs best at all update rates. In the sweep test, the RBPS1 yields comparable or slightly better (less than 20 mm) results than the EKS, but the RBPS1 performs comparable to the EKS in both sweep and swing tests. Therefore, although the swing operation can obtain position and orientation data for the UXO detection in shorter time duration and therefore with fewer control points, the sweep operation is preferred because the position errors of the sweep test were smaller than that of swing test due to the linear dynamics of the sweep motion.

The UPS needs at least 200 particles to yield best position accuracy in this test. However, the Rao-Blackwellized based filter/smoothers (RBPS1 and RBPS2) utilized only 20 samples (particles) for the nonlinear filter (particle filter) part. Although there is still room for some position accuracy improvement by increasing the number of particles, it will not yield significant improvements (refer the simulation test in the section 3.4.3, Figure 3. 11). Therefore, the RBPS2 can produce (slightly) better or comparable results compared to the UKS with the 10% of the number of particles used by the UKS.

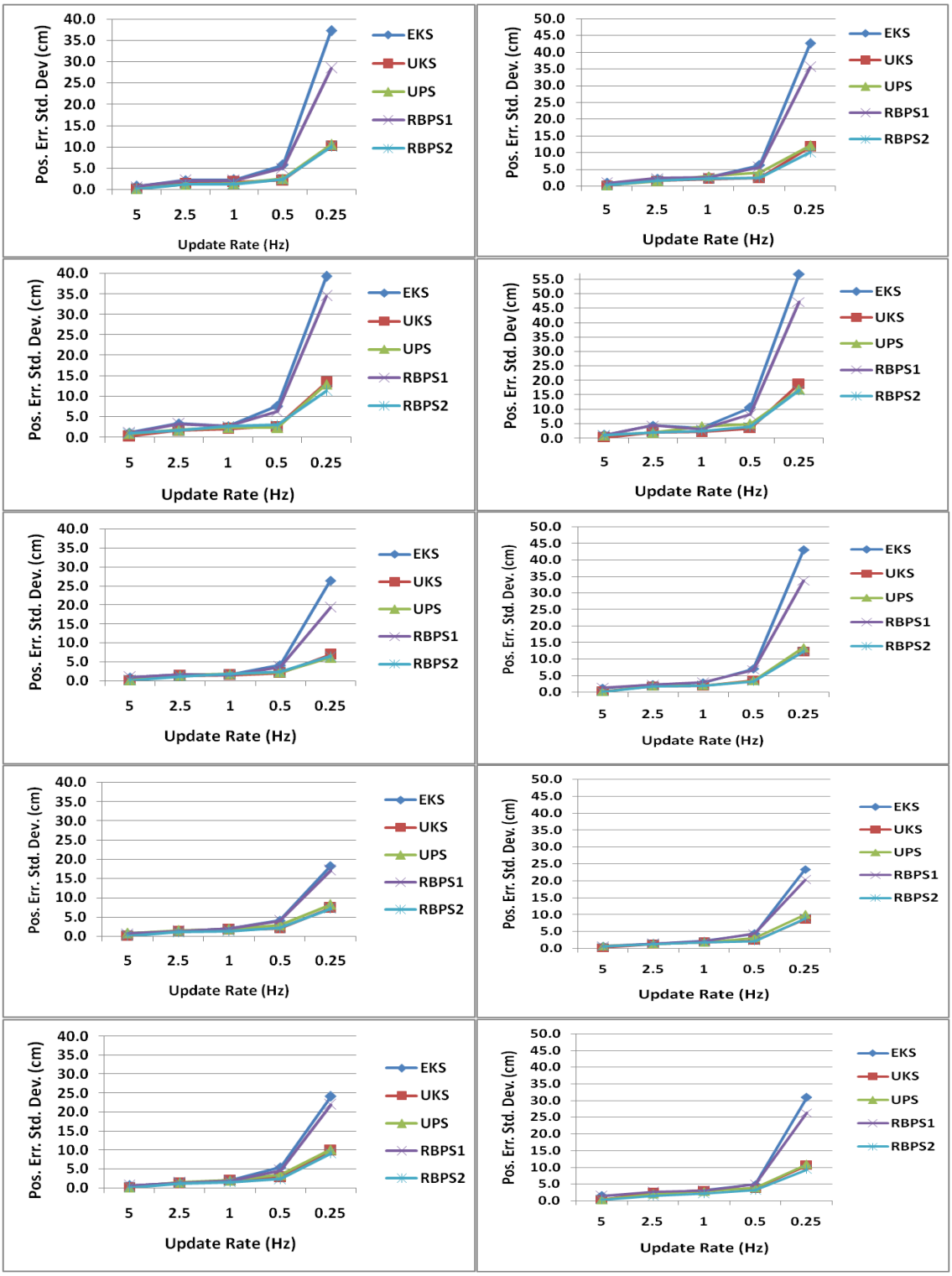

Figure 5.11. The standard deviations of position error in five separate sweep tests according to different smoothing methods (first column: straight section, second column: curved section, first row: test1, second row: test2, third row: test3, fourth row: test4, and fifth row: test 5) (unit: cm)

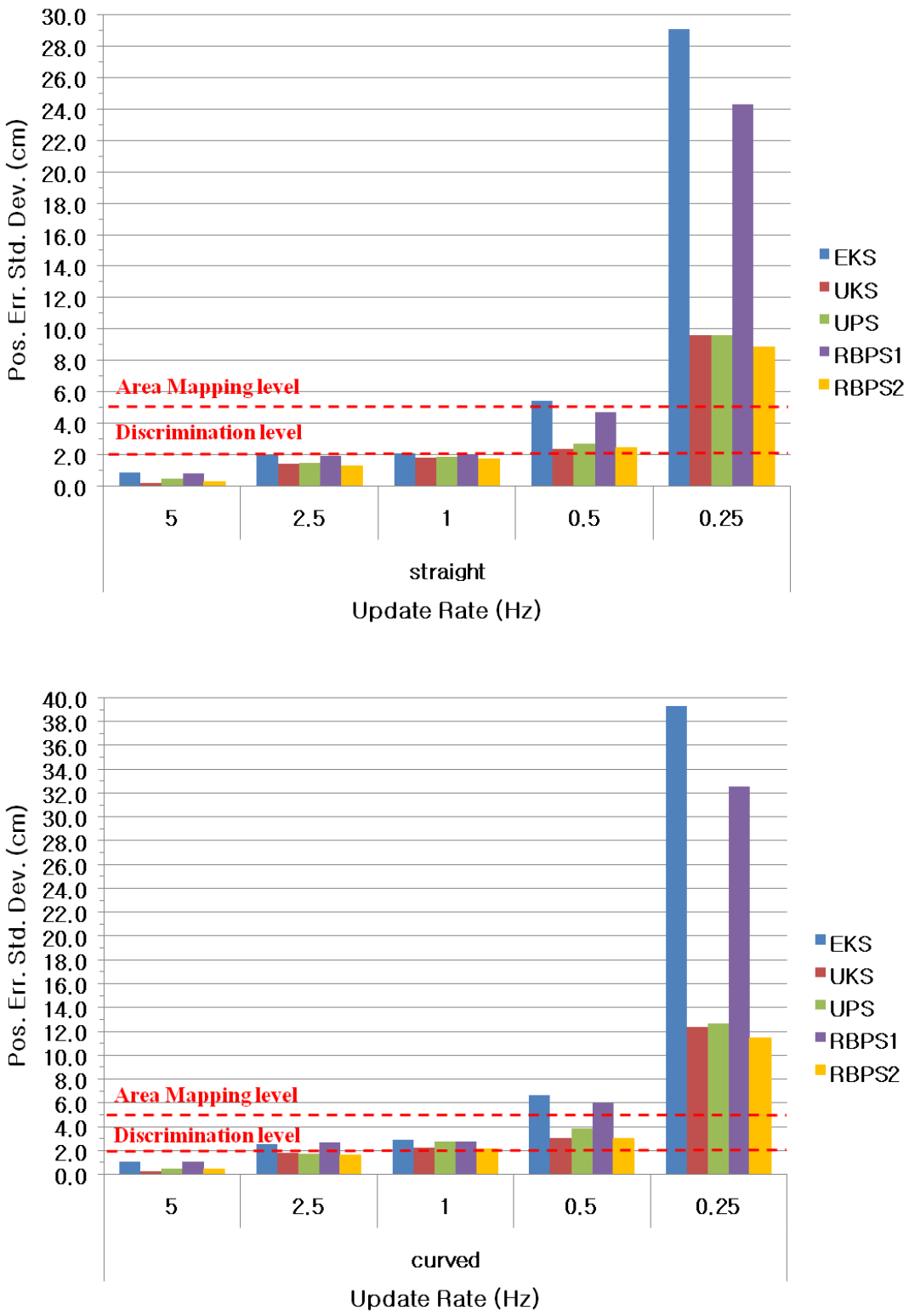

Figure 5.12. The average standard deviations of position errors according to various smoothing methods (first row: straight, second row: curved) (unit: cm).

5.3.3. Summary

A Handheld Geolocation System (HGS) using a tactical-grade IMU was designed to obtain precise position and orientation of an UXO detection system and to be applied in relatively small areas (1.0m by 1.0m). The HGS has only one tactical-grade IMU (HG1900) to satisfy low-weight requirements. Since the test is operated in a closed environment that has no GPS signal available, an automatic position tracking system was designed and implemented. This could be comparable to GPS if we can set the GPS antenna on top of the hand-held system.

To improve the geolocation accuracy, coarse and fine data calibration techniques are employed first to estimate the constant biases of the gyros and accelerometers. Then nonlinear smoothers that are based on forward/backward filtering techniques (EKS, UKS, UPS, RBPS1, and RBPS2) were tested and analyzed for the two typical local handheld detection platform trajectories (sweep and swing).

On the whole, position accuracy improvements were achieved by applying nonlinear filter-based smoothing techniques (UKS, UPS, and RBPS2) in both the straight and curved section. The HG1900-based handheld geolocation system with a nonlinear filter-based smoother achieved the characterization and discrimination level of accuracy if the update rate of control points is less than 0.5Hz and 1Hz for the sweep and swing modes respectively. Therefore, although the data collection using the swing operation can be done in shorter time, the sweep operation is generally better than the swing test because of the dynamics of swing operation is too highly nonlinear.

CHAPTER 6: CONCLUSIONS

The reliable discrimination of UXO by a detection system depends on the employed sensor technology as well as on the data processing methods that invert the collected data to infer the UXO. The various detection system platforms such as handheld, man-portable units, vehicle-based units, and airborne systems mostly use total field magnetometer and electromagnetic induction (EMI) sensors (DSB, 2003). These detection systems require a very accurate positioning (or geolocation) and orientation in order to discriminate the candidate UXO from non-hazardous clutter when inverting magnetic or EMI data (Bell, 2005).

The primary geolocation system considered by many several investigations is based on as a dual-frequency GPS integrated with a three dimensional inertial measurement unit (IMU); i.e. the INS/GPS system. Selecting the appropriate estimation method is a key aspect in obtaining precise geolocation of the INS/GPS systems for the UXO detection performance in dynamic environments. For this purpose, the Extended Kalman Filter (EKF) has been used as the conventional algorithm for the optimal integration of the INS/GPS system. However, newly introduced non-linear filters can deal better with the non-linear nature of the positioning dynamics as well as the potential non-Gaussian statistics of the instrument errors. Therefore, this study focused on these new optimal estimation methods for the high precise geolocation required in UXO detection using simulations and analyses of two laboratory tests. From the various simulation tests, the cart-based as well as the handheld geolocation system data, the following conclusions are obtained:

1. The non-linear filters (UKF and UPF) have been shown to yield superior performance over the EKF in various specific tests which were designed to simulate the UXO geolocation environment (highly dynamic and small area). On average the UKF yields 50% improvement in the position accuracy over the EKF, particularly in the curved sections of the platform trajectory (medium-grade IMU case). The UPF also performed significantly better than the EKF and showed comparable results to the UKF when the IMU noise is symmetric and non-symmetric. Also, since the UXO detection survey does not necessarily require real-time operations, each of the developed filters was modified to accommodate the standard Rauch-Tung-Striebel (RTS) smoothing algorithm. When the smoothing method was applied to the typical UXO detection trajectory, the position error reduced significantly using a minimal number of control points. It would replace the template method by precision geolocation from sensor-mounted IMUs. Finally, these simulation tests confirmed that tactical-grade IMUs (e.g., HG1700 or HG1900) are required to bridge gaps in high-accuracy ranging solution systems, like GPS, longer than 1 second.
2. The results of the simulation tests were validated using the laboratory tests with

3. navigation-grade and medium-grade accuracy IMUs. To overcome inaccurate a priori knowledge of the process noise of the system, standard adaptive filtering methods have been applied to the EKF and UKF, denoting the corresponding smoothers as the AEKS and AUKS. The neural network aided adaptive nonlinear filtering/smoothing methods (NN-EKS and NN-UKS) which are augmented with the RTS smoothing method were compared with the AEKS and AUKS. Each neural network-aided, adaptive filter/smoother improved the position accuracy in both straight and curved sections of the test trajectory. The navigation-grade IMU (H764G) can achieve the area mapping level of accuracy when the gap between control points is about 8 seconds. The medium-grade IMUs (HG1700 and HG1900) with NN-AUKS can maintain an accuracy better than10cm under the same conditions as above. Also, the neural network aiding can decrease the difference of position errors between the straight and the curved sections.
4. In the previous simulation test, the UPF performed best among all other filters. However since the UPF needs a large number of samples to represent the a posteriori statistics in high-dimensional space, the Rao-Blackwellized Particle Filter (RBPF) can be used as alternative to increase the efficiency of the particle filter. The RBPF was tailored to the precise geolocation application for UXO detection using the IMU/GPS system and yielded improved estimation results with a smaller number of samples. The handheld geolocation system using the HG1900 with a nonlinear filter-based smoother can achieve the discrimination level of accuracy if the update rate of control points is less than 0.5Hz and 1Hz for the sweep and swing modes, respectively. Also, the sweep operation is preferred over the swing motion because the position accuracy of the sweep test was generally better than that of swing test because the dynamics of swing motion is more highly non-linear.

It is concluded that the IMU/GPS geolocation system with non-linear filters/smoothers can achieve the discrimination and area mapping level of accuracy in a relatively small area if the update rate of control point is less than 0.5Hz.

Improved performance of the UXO geolocation system will aid significantly in the inversion of field data for more accurate characterization of candidates for buried munitions, thus greatly reducing the number of false positives, which currently can reach 90% or more. This will save billions of dollars in the remediation cost of UXO contaminated sites.

To achieve even better results, the proposed neural network aiding for adaptive filtering could be applied to the RBPF because the RBPF is based on the Kalman filter framework. Also, we may consider other types of new filters such as the Gaussian Sum filter (Alspach and Sorenson, 1972), Kriged filters (Blázquez, 2008), sigmaRho filters (Grewal, 2009) etc. as well as new semi-automatic geolocation systems based on the mobile Terrain Robot or Personal Navigation System. The idea of the semi-automatic geolocation system using a Terrain Robot may address the limitations of the man-portable UXO detection devices. The man-portable units such as handheld or cart-based geolocation system suffer from the constantly changing velocity and orientation of platform due to the terrain and human operator etc. Therefore, if we can use a mobile terrain Robot based geolocation system for the suspected UXO data, we can obtain possibly more uniform velocity and orientation data. Also, we experienced the benefit

of vision-based positioning using real-time image in the HGS test in chapter 5. If the HGS can be integrated with a personal navigation system, we may achieve better position and orientation accuracy because the interval of the simulated external ranging solution system is less than 1 Hz.

Appendix A. Navigation Equations and Assumption

The navigation equations in n-frame are constituted a set of six, non-linear, differential equations (Jekeli, 2000).

$$\frac{d}{dt}\begin{pmatrix} v_N \\ v_E \\ v_D \end{pmatrix} = \begin{pmatrix} a_N + \bar{g}_N - 2\omega_e \cdot \sin\phi \cdot v_E + \dot{\phi} \cdot v_D - \dot{\lambda} \cdot \sin\phi \cdot v_E \\ a_E + \bar{g}_E + 2\omega_e \cdot \sin\phi \cdot v_N + 2\omega_e \cdot \cos\phi \cdot v_D + \dot{\lambda} \cdot \sin\phi \cdot v_N + \dot{\lambda} \cdot \cos\phi \cdot v_D \\ a_D + \bar{g}_D - 2\omega_e \cdot \cos\phi \cdot v_E - \dot{\lambda} \cdot \cos\phi \cdot v_E - \dot{\phi} \cdot v_N \end{pmatrix} \tag{A.1}$$

$$\begin{pmatrix} \dot{\phi} \\ \dot{\lambda} \\ \dot{h} \end{pmatrix} = \begin{pmatrix} \dfrac{v_N}{M+h} \\ \dfrac{v_E}{(N+h)\cos\phi} \\ -v_D \end{pmatrix} \tag{A.2}$$

Assumption 1: our target system (Cart-based Geolocation system (Chapter 4) and Handheld Geolocation system (Chapter 5)) usually experience not too large velocities ($\text{say} \le 10\, m/s$), it can be assumed that $\dot{v}^n = 0$ (that is, $\dot{\phi} = 0$ and $\dot{\lambda} = 0$) and ignoring the horizontal gravity vector ($\bar{g}_N = 0$ and $\bar{g}_E = 0$), the equation (A.1) can be rewritten as follows

$$\frac{d}{dt}\begin{pmatrix} v_N \\ v_E \\ v_D \end{pmatrix} \approx \begin{pmatrix} a_N - 2\omega_e \cdot \sin\phi \cdot v_E \\ a_E + 2\omega_e \cdot \sin\phi \cdot v_N + 2\omega_e \cdot \cos\phi \cdot v_D \\ a_D + \bar{g}_D - 2\omega_e \cdot \cos\phi \cdot v_E \end{pmatrix} \tag{A.3}$$

The equation (A.3) was used as navigation equations through entire chapters.

Appendix B. INS Coarse and Fine Alignment and Calibration

INS Initialization is the determination of the initial position and velocity which required as initial constant in the navigation equations (Appendix A.). If the platform is stationary, its velocity is known and has known coordinates. Besides the initial position and velocity, the initial alignment of inertial sensor which is the direction cosine between the body and the navigation frame (in Strapdown mechanism) must be established before navigation is started because this alignment is employed for subsequent computation of attitude by integration of the gyro output.
In this report, the basic alignment methods are applied to UXO detection platform with external velocity and orientation (primarily azimuth) when system is stationary. The coarse alignment provides crude first values for the attitude angle that subsequently will be refined using linear estimation (chapter 3). As next, the fine alignment methods are used to correct alignment errors based on external positioning or navigation source.

B.1 Coarse Alignment

The coarse alignment for INS can provide orientation of the Strapdown platform with respect to the navigation frame using IMU's accelerometer and angular rates without considering their errors.
In a stationary system ($v^w = 0$), the accelerometer output is

$$a^b = C_w^b \cdot a^w = -C_w^b \cdot \bar{g}^w = -\bar{g}^b \tag{B.1}$$

Also, the gyro output with $\omega_{wb}^b = 0$ in stationary vehicle is

$$\omega_{ib}^b = C_w^b \cdot \omega_{iw}^w \tag{B.2}$$

The ultimate goal of alignment is to determine direction cosine matrix of the transformation from the body frame to the navigation frame using the accelerometer and gyro outputs.
Let c^n as additional vector which is orthogonal to both $\bar{g}^w$ and ω_{ie}^w

$$c^w = \bar{g}^w \times \omega_{ie}^w = \bar{g}^w \times \omega_{iw}^w \tag{B.3}$$

where the second equality owe $\omega_{we}^w = 0$ if the platform is stationary
If we neglect the deflection of vertical, the gravity vector has only one component in down direction:

$$\bar{g}^w = \begin{pmatrix} 0 & 0 & \bar{g} \end{pmatrix}^T \tag{B.4}$$

where $\bar{g}$ is the magnitude of gravity, from equation , since velocity is zero

$$\omega_{iw}^w = \begin{pmatrix} \omega_e \cos\phi \cos\alpha \\ -\omega_e \cos\phi \sin\alpha \\ \omega_e \sin\phi + \dot{\alpha} \end{pmatrix} \tag{B.5}$$

Substituting the equation (B.5) into equation (B.3)

$$c^w = \begin{pmatrix} \bar{g} \cdot \omega_e \cos\phi \sin\alpha \\ \bar{g} \cdot \omega_e \cos\phi \cos\alpha \\ 0 \end{pmatrix} \tag{C.6}$$

Using $[g^w\times]$ as skew-symmetric matrix, the c^b is

$$\begin{aligned} c^b &= C_w^b \cdot c^w \\ &= C_w^b \cdot [\bar{g}^w\times] \cdot \omega_{iw}^w = C_w^b \cdot [\bar{g}^w\times] \cdot C_b^w \cdot C_w^b \cdot \omega_{iw}^w = [\bar{g}^w\times] \cdot \omega_{iw}^w \\ &= -a^b \times w_{iw}^b = -a^b \times (\omega_{ib}^b + \omega_{bw}^b) \\ &= -a^b \times \omega_{ib}^b \end{aligned} \tag{B.7}$$

Equation (C.1), (C.2) and (C.7) are combined into

$$(a^b \quad \omega_{ib}^b \quad -a^b \times \omega_{ib}^b) = C_w^b(-\bar{g}^w \quad \omega_{iw}^w \quad c^w) \tag{B.8}$$

Finally, C_w^b is solved as

$$C_b^w = \begin{pmatrix} 0 & 0 & -\bar{g} \\ \omega_e \cos\phi \cos\alpha & -\omega_e \cos\phi \sin\alpha & -\omega_e \sin\phi + \dot{\alpha} \\ \bar{g} \cdot \omega_e \cos\phi \sin\alpha & \bar{g} \cdot \omega_e \cos\phi \cos\alpha & 0 \end{pmatrix}^{-1} \begin{pmatrix} (a^b)^T \\ (\omega_{ib}^b)^T \\ (-a^b \times \omega_{ib}^b)^T \end{pmatrix} \tag{B.9}$$

Usually, the IMU sensor has the zero wander azimuth ($\alpha = 0$) and azimuth rate $\dot{\alpha} = 0$ then, equation (C.9) in n-frame is

$$C_b^n = \begin{pmatrix} 0 & 0 & -\bar{g} \\ \omega_e \cos\phi & 0 & -\omega_e \sin\phi \\ 0 & \bar{g} \cdot \omega_e \cos\phi & 0 \end{pmatrix}^{-1} \begin{pmatrix} (a^b)^T \\ (\omega_{ib}^b)^T \\ (-a^b \times \omega_{ib}^b)^T \end{pmatrix} \quad \text{(B.10)}$$

Equation (B.9) and (B.11) are employed to determine the body-frame-to-navigation-frame transformation matrix using the accelerometers and gyros output in the fixed strapdown navigation system.
However, this method based on ideal situation that there are no errors in accelerometer and gyroscope. In actual, the accelerometer and gyroscope has errors, especially gyroscope has large rate biases.

B.2 Fine Alignment and Calibration
After coarse alignment, the only small angle differences will be remained. Particularly, gyro biases that are different whenever the system is turned on cause the accuracy degradation of the navigation solution (mostly in the heading). As the fine alignment refines the coarse alignment by using external information, it determines the azimuth reference and the calibration of the gyro biases.
Since the test platform is stationary with respect to the Earth, the position is known without error and the velocity is also zero (called zero velocity condition). Usually, the external azimuth observation (from optical system or directional radar system) is not available, self-alignment and calibration of the (vertical) orientation entirely depend on the sensitivity to Earth's rotation (Thus, it takes long time to determine errors).
The system state vectors, ε, are the orientation error, the gyro biases, and the velocity errors

$$\varepsilon = [\psi_N \quad \psi_E \quad \psi_D \quad \Delta\omega_N \quad \Delta\omega_E \quad \Delta\omega_D \quad \delta V_N \quad \delta V_E]^T \quad \text{(B.11)}$$

The dynamic model for orientation error state is

$$\dot{\psi}^n = -\omega_{ie}^n \times \psi^n - C_s^n \cdot \delta\omega_{is}^s + \delta\omega_{in}^n \quad \text{(B.12)}$$

Since the vehicle is stationary, it is assumed that $\delta\omega_{is}^s$ consist of gyro biases only (thus, $C_s^n \delta\omega_{is}^s$ is also gyro biases in navigation frame).
Let these biases as (simple) random constants

$$\Delta\dot{\omega} = \frac{d}{dt}\begin{pmatrix} \Delta\omega_N \\ \Delta\omega_E \\ \Delta\omega_D \end{pmatrix} = 0 \quad \text{(B.13)}$$

Also, since the position errors are zero

$$\delta\omega_{in}^{n} = \begin{pmatrix} \dfrac{\delta v_E}{r} \\ -\dfrac{\delta v_N}{r} \\ -\dfrac{\delta v_E}{r}\tan\phi \end{pmatrix} \tag{B.14}$$

where $r = R_\phi + h$

From the dynamics of the velocity errors, if we neglect the accelerometer errors, gravity errors, and vertical velocity error

$$\begin{aligned} \frac{d}{dt}\delta v_N &= -2\omega_e \sin\phi \cdot \delta v_E + \overline{g} \cdot \psi_E \\ \frac{d}{dt}\delta v_E &= 2\omega_e \sin\phi \cdot \delta v_N - \overline{g} \cdot \psi_N \end{aligned} \tag{B.15}$$

These equation (B.12), (B.13), and (B.15) are combined to form a set of linear differential equations

$$\dot{\varepsilon} = F \cdot \varepsilon \tag{B.16}$$

with

$$F = \begin{bmatrix} 0 & -\omega_e \sin\phi & 0 & -1 & 0 & 0 & 0 & \dfrac{1}{r} \\ \omega_e \sin\phi & 0 & \omega_e \cos\phi & 0 & -1 & 0 & -\dfrac{1}{r} & 0 \\ 0 & -\omega_e \cos\phi & 0 & 0 & 0 & -1 & 0 & \dfrac{1}{r}\tan\phi \\ 0 & 0 & 0 & 0 & 0 & 0 & 0 & 0 \\ 0 & 0 & 0 & 0 & 0 & 0 & 0 & 0 \\ 0 & 0 & 0 & 0 & 0 & 0 & 0 & 0 \\ 0 & \overline{g} & 0 & 0 & 0 & 0 & 0 & -2\omega_e \sin\phi \\ -\overline{g} & 0 & 0 & 0 & 0 & 0 & 2\omega_e \sin\phi & 0 \end{bmatrix} \tag{B.17}$$

The horizontal velocity components which are the differences between velocity of system and the Earth-referenced velocity of the system (zero, if the vehicle is stationary) are used as observations.

The linear relationship between states and observation is

$$y = H \cdot \varepsilon + \upsilon, \tag{B.18}$$

where the matrix H is

$$H = \begin{bmatrix} 0 & 0 & 0 & 0 & 0 & 0 & 1 & 0 \\ 0 & 0 & 0 & 0 & 0 & 0 & 0 & 1 \end{bmatrix} \tag{B.19}$$

and $\upsilon \sim N(0, R)$

$$R = \begin{bmatrix} \sigma_{vel}^2 & 0 \\ 0 & \sigma_{vel}^2 \end{bmatrix} \cdot \Delta t \tag{B.20}$$

with σ_{vel} is the standard deviations of the velocity observations.

B.3 Test

The five *static* dataset of HG1900 were collected before the sweep and swing test of chapter 5. Data collection process was started after switching the IMUs on. The sampling rate of IMU data is 100Hz and the data duration of each static data collection is about 5 min.

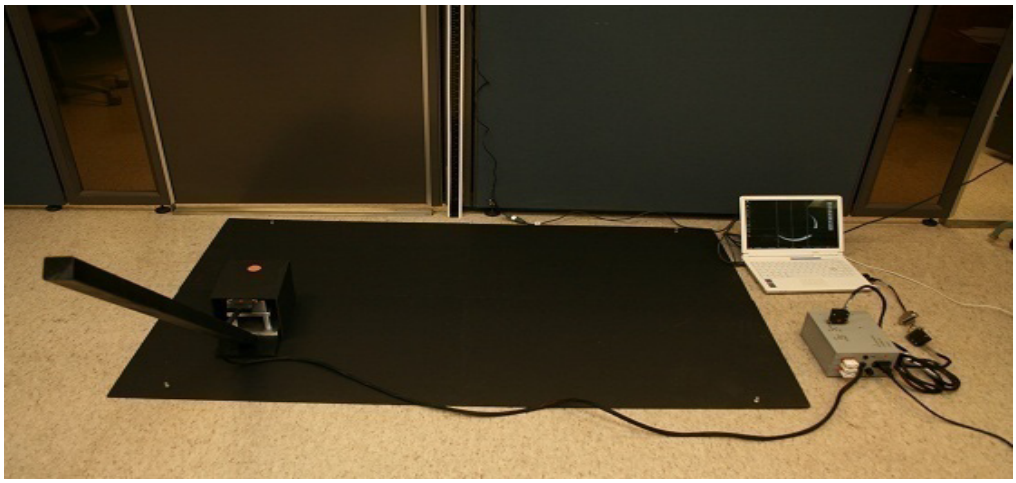

Figure B.1. Data collection system for Coarse and Fine alignment and calibration: Run-box, desktop, monitor and IMU on solid mount.

The table B.1 shows the estimated bias of gyro and accelerometers of HG1900 through coarse and fine alignment and calibration steps. The gyro bias (east direction) showed more larger value than that of the manufacture published (< 7 º/hr). The accelerometer bias (north direction) yielded the two times larger than the manufacturer specifications (1mg, see the table 4.1).

		1	2	3	4	5	Average
Gyro bias	$\delta\omega_{GN}$ [°/hr]	-5.50	-7.50	-4.95	-9.89	-7.29	-7.03
	$\delta\omega_{GE}$ [°/hr]	-11.21	-13.80	-8.20	-13.46	-13.81	-12.10
	$\delta\omega_{GD}$ [°/hr]	-7.48	-7.25	-7.01	-9.54	-7.24	-7.70
Accelerometer bias	δa_{AN} [mg]	2.15	2.13	2.25	2.20	2.28	2.20
	δa_{AE} [mg]	1.18	1.04	0.90	1.11	1.04	1.05

Table B.1. The estimated bias of gyro and accelerometer of HG1900.

References

1. Aggarwal, P., Gu, D., and El-Sheimy, N. (2006), Adaptive Particle Filter for INS/GPS Integration. ION GNSS 19th International Technical Meeting of the Satellite Division, 26-29, Fort Worth, Texas, September 2006, pp.1606-1613.
2. Aleksander, I., Morton, H. B. (1990), General neural unit: retrievability performance. Electronics Letters, 27, 1776-1777.
3. Anderson, B.D.O, Moore, J.B. (1979), *Optimal Filtering*, Prentice Hall, New York, NY, 1979.
4. Andrieu, C., de Freitas, N., Doucet, A., and Jordan, M.I. (2003), An introduction to MCMC for machine learning. *Machine Learning*, 50, 5-43.
5. Anthony, M., P. Bartlett (1999), *A Theory of Learning in Artificial Neural Networks*. Cambridge University Press, Cambridge, UK, 1999.
6. Arulampalam, M.S., Maskell, S., Gordon, N., and Clapp, T. (2001), A tutorial on particle filters for online nonlinear/non-gaussian bayesian tracking, *IEEE Trans. Signal Process.* 50 (2001) (2), pp. 174–188.
7. Avitzour, D. (1995), Stochastic simulation Bayesian approach to multitarget tracking, Radar, Sonar and Navigation, IEE Proceedings, Publication Date: Apr 1995, Volume: 142, Issue: 2, On page(s): 41-44.
8. Barto, A. G., Sutton, R. S., and Anderson, C. W. (1983), Neuronlike adaptive elements that can solve difficult learning control problems. *IEEE Transactions on Systems, Man, and Cybernetics*, SMC-13:834-846.
9. Beadle E. R., Djurić, P. M. (1997), A fast-weighted Bayesian bootstrap filter for nonlinear model state estimation, *IEEE Trans. on Aerospace and Electronic Systems*, vol. 33, no. 1, pp. 338-343, 1997.
10. Bell, T. (2001), Subsurface discrimination using electromagnetic induction sensors, IEEE Transaction Geoscience and Remote Sensing, 39: 1286-1293.
11. Bell, T. (2005), Geo-location Requirements for UXO Discrimination, Presented at SERDP & ESTCP Geolocation Workshop, 1-2 June 2005, Annapolis, MD.
12. Bell T., Collins, L. (2007), Handheld UXO Sensor Improvements to Facilitate UXO/Clutter Discrimination, SERDP Final Report, Vol 1., Nov. 2007.
13. Billings, S. D., Pasion, L. R., Beran, L., Oldenburg, D., Sinex, D., Song, L., Lhomme, N., (2007), ESTCP MM-0504, Practical Discrimination Strategies for Application to Live Sites: Demonstration Report for the Former Lowry Bombing and Gunnery Range: ESTCP Program Office.
14. Bishop, C.M. (1995), *Neural Networks for Pattern Recognition*, Oxford University Press, London, UK, 1995.
15. Brown, R.G., Hwang, P.Y.C. (1992), *Introduction to Random Signals and Applied Kalman Filtering,* John Wiley & Sons, Inc., New York, NY, 1992.

16. Capuzzo JP (2007), After ordnance scare, beachgoers told to dig with care, New York Times, NY, 2007.
17. Cawsey, A (1998), *The Essence of Artificial Intelligence*, Prentice Hall PTR, Upper Saddle River, NJ, 2008.
18. Chiang, K.W. (2004), INS/GPS Integration Using Neural Network for Land Vehicular Navigation Application. Ph.D. Thesis, University of Calgary, UCGE Report 20209.
19. Chiang, K.W. (2005), INS/GPS Integration Using Neural Networks for Land Vehicular Navigation Applications. Ph.D. thesis, University of Calgary, UCGE Report 20209.
20. Clynch, J. R. (2001), Lecture note for FUNDAMENTALS OF GEOSPATIAL INFORMATION AND SERVICES, Naval Postgraduate School, Monterey, CA, 2001.
21. Collins L.M., Zhang Y., Li J., Wang H., Carin L., Hart S., Rose-Pehrsson S., Nelson H., and McDonald J. (2001), A comparison of the performance of statistical and fuzzy algorithms for unexploded ordnance detection, Special issue on Recognition Technology, IEEE Trans Fuzzy Systems 9(1): 17-30.
22. Defense Science Board (2003), Report of the Defense Science Board Task Force on Unexploded Ordnance, Office of the Under Secretary of Defense for Acquisition, Technology, and Logistics, Washington, D.C. 20301-3140, December 2003.
23. Demuth, H., Beale, M. (2004), Neural network toolbox for use with Matlab, The MathWorks, Natick, MA, 2004.
24. Ding, M., Zhou, Q., and Wang, Q. (2006), The Application of Self-adaptive Kalman filter in NGIMU/GPS Integrated Navigation System. Volume 2 of the Proceedings of the Sixth International Conference on Intelligent Systems Design and Applications, Washington, DC, Oct. 2006, pp.61-65.
25. Doucet, A. (1999), Joint Bayesian Detection and Estimation of Noisy Sinusoids via Reversible Jump MCMC, *IEEE Trans. Signal Processing,* vol. 47, no. 10, pp. 2667-2676, Istanbul, Turkey, 1999.
26. Doucet, A. (2000), On Sequential Training of Neural Networks Models, *Neural Computation*, vol. 12, no. 4, pp. 955-993, 2000.
27. Doucet, A., de Freitas J.F.G. and Gordon, N.J. (2001), An Introduction to Sequential Monte Carlo Methods, in *Sequential Monte Carlo Methods in Practice,* New York: Springer-Verlag, January 2001.
28. Doucet, A. (2008), A Tutorial on Particle Filtering and Smoothing: Fifteen years Later, (with A.M. Johansen), in *Handbook of Nonlinear Filtering*, Oxford University Press, to appear.
29. Efron B (1982), *The Jackknife, the Bootstrap and Other Resampling Plans*. CBMS-NSF Regional Conference Series in Applied Mathematics, Monograph 38, SIAM, Philadelphia, 1982.
30. Mohamed, E., El-Ghazouly, A., and El-Sheimy, N. (2008), Evaluation of Wavelet Multipath Mitigation Technique in the Final Measurement Domain, Proceedings of the 2009 International Technical Meeting of the Institute of Navigation, January 26 - 28, 2009, Disney's Paradise Pier Hotel, Anaheim, CA.
31. El-Sheimy, N., Nassar, S., and Noureldin, A. (2004), Wavelet de-noising for IMU alignment. *IEEE Aerospace and Electronic Systems Magazine*, 19(10), 32 – 39.

32. Euston, M., Kim, J. (2007), Rao-Blackwellised Inertial-SLAM with Partitioned Vehicle Subspace, Australasian Conference on Robotics and Automation (ACRA'07), Brisbane, Australia, Dec 10-12, 2007.
33. Foely, J. (2006), Sensor Orientation Effects on UXO Geophysical Target Discrimination, SERDP Project No. MM-1310, Final Report, Dec. 2006.
34. Garcia, V. J. (1997), Determination of noise covariances for extended Kalman filter parameter estimators to account for modeling errors, Ph. D. dissertation, University of Cincinnati, 1997.
35. Gelb, A. (ed.) (1974), *Applied Optimal Estimation*. MIT Press, Cambridge, MA, 1974.
36. Giremus, A. Doucet, A. Calmettes, V., and Tourneret, J. Y., (2003), A Rao-Blackwellized particle filter for INS/GPS integration, Acoustics, Speech, and Signal Processing, 2004. Proceedings. (ICASSP '04). IEEE International Conference on 17-21 May 2004, Volume: 3, On page(s): iii- 964-7 vol. 3.
37. Godsill, S. J., Doucet, A., and West, M. (2000), Monte Carlo smoothing for nonlinear time series, In Symposium on Frontiers of Time Series Modeling, Tokyo, Japan, Institute of Statistical Mathematics, 2000.
38. Golden, R. M. (1996), *Mathematical Methods for Neural Network Analysis and Design*, MIT Press, Cambridge, MA, 1996.
39. Gordon, N., Salmond, D., and Smith, A.F.M. (1993), Novel approach to nonlinear and non gaussian state estimation. Proceeding Inst. Elect. Eng., F, Vol. 140, pp. 107-113.
40. Grejner-Brzezinska, D. A.(2001), Direct Sensor Orientation in Airborne and Land-based Mapping Applications, 51 pp, June 2001. OSU report 461.
41. Grewal, M.S., Andrews, A.P. (1993), *Kalman Filtering: Theory and Practice*. John Wiley & Sons, Inc., New York, 1993.
42. Grewal, M.S., Andrwes, A.P. (2001), *Kalman Filtering: Theory and Practice Using MATLAB®*. John Wiley & Sons, Inc., New York, 2001.
43. Grewal, M. S., Weil, L. R. (2001), *Global Positioning Systems, Inertial Navigation and Integration*, New York, Wiley, 2001.
44. Guo, J.C., Teng, J., Li, Q., and Zhang, Y. (2003), The de-noising of gyro signals by biorthogonal wavelet transform. Volume 3 of the Proceedings of the Canadian Conference on Electrical and Computer Engineering, 4 - 7 May 2003. pp.1985 – 1988.
45. Gustafsson, F., Gunnarsson, F., Bergman, N., Forssell, U., Jansson, J., Nordlund, P.J., and Karlsson, R. (2001), A framework for particle filtering in positioning, navigation and tracking problems, Proceedings of the 11th IEEE Signal Processing Workshop on Statistical Signal Processing, 6-8 Aug. 2001, pp.:34 – 37.
46. Hawkins, W., Daku, B.L.F., and Prugger, A.F. (2005), Vehicle localization in underground mines using a particle filter, Canadian Conference on Electrical and Computer Engineering, 1-4 May 2005, pp.2159 – 2162.
47. Haykin S. (1999), *Neural Networks: A Comprehensive Foundation* (2nd Edition), Prentice Hall, New Jersey, 1999.
48. Haykin, S. (2001), *Kalman Filtering and Neural Networks*. John Wiley & Sons, Inc., New York, 2001.

49. Hektor, T. (2007), Marginalized Particle Filter for Aircraft Navigation in 3-D, Ph.D. Dissertation, Linkoping University, Linköping, Sweden, 2007.
50. Hide, C., Moore, T., and Smith, M. (2004), Adaptive Kalman filtering algorithms for integrating GPS and low cost INS, Position Location and Navigation Symposium 2004 (PLANS 2004), 26-29 April 2004, pp.227 – 233.
51. Higuchi, T. (1997), Monte Carlo filter using the genetic algorithm operators, *Journal of Statistical Computation and Simulation*, 59(1):1-23, 1997.
52. Honavar, V., Uhr L. (1994), *Artificial Intelligence and Neural Networks: Steps Towrard Principled Integration*, Academic Press, Boston, 1994.
53. Jansson, P. (1998), Precise kinematic GPS positioning with Kalman filtering and smoothing: theory and applications. PhD Thesis, Report No. 1048, Department of Geodesy and Photogrammetry, Royal Institute of Technology, Stockholm, Sweden.
54. Jekeli, C. (2000), *Inertial Navigation Systems with Geodetic Applications*, Walter deGruyter, Inc., Berlin, 2000.
55. Jekeli, C (2004), Cold Atom Interferometer as Inertial Measurement Unit for Precision Navigation, Proceedings of the 60th Annual Meeting, June 7 - 9, 2004, Dayton Marriott Hotel, Dayton, Ohio.
56. Jekeli, C., J.K. Lee (2007), Technical Assessment of IMU-Aided Geolocation Systems for UXO detection and Characterization. Technical Report, Project Number MM-1565, Strategic Environment R&D program (SERDP), Arlington, VA.
57. Julier, S.J. (1998), A Skewed Approach to Filtering. SPIE Conference on Signal and Data Processing of Small Targets, Orlando. Florida, April 1998.
58. Julier, S.J., Uhlmann J.K., and Durrant-Whyte H.F. (1995), A new approach for filtering nonlinear systems. Proc. of the American Control Conference, Seattle, WA, pp.1625-1632.
59. Julier, S.J., Uhlmann J.K. (1996), A general method for approximating nonlinear transformations of probability distributions, Technical report, Department of Engineering Science, University of Oxford, Oxford, England.
60. Julier, S.J., Uhlmann J.K., and Durrant-Whyte H.F. (2000), A new approach for nonlinear transformations of means and covariances in filters and estimators. *IEEE Transactions on Automatic Control*, 45(3), 477-482.
61. Jwo D.H., Huang H.C. (2004), Neural network aided adaptive extended Kalman filtering approach for DGPS positioning, *Journal of Navigation*, pp. 449-463, 2004.
62. Kalman, R.E. (1960), A New Approach to Linear Filtering and Prediction Problems. *Trans. of the ASME--Journal of Basic Engineering*, 82, Num. Series D, 35-45.
63. Kim, D., Bisnath, S., Langley, R.B., and Dare, P. (2004), Performance of Long-baseline Real-Time Kinematic Applications by Improving Tropospheric delay Modeling, Proceedings of the Institute of Navigation International Technical Meeting ION GNSS, 21-24 September 2004, Long Beach, California.
64. Kitagawa, G. (1996), Monte Carlo filter and smoother for non-Gaussian nonlinear state space models, *J. Comput. Graph. Stat.,* vol. 5. Pp. 1-25, 1996.
65. Klass, M., Briers M., de Freitas N., Doucet, A., Maskell, S., and Lang, D. (2006), Fast particle smoothing: If I had a million particles, in Proc. ICML 2006, Pittsburgh, PA, pp. 481-488.

66. Koch, K. R. (1987), *Parameter Estimation and Hypothesis Testing in Linear Models*, Bonn, Springer Verlag, 1987.
67. Komunjer, I. (2007), Asymmetric power distribution: Theory and applications to risk measurement. *Journal of Applied Econometrics*, 22(5), 891-921.
68. Kong, A., Liu, J. S., and Wong, W. H. (1994), Sequential imputations and Bayesian missing data problems, *Journal of the American Statistical Association*, 89 (425):278-288, 1994.
69. Kornuyenko, O.V., Sharawi, M.S., and Aloi, D.N. (2005), Neural Network Based Approach for Tuning Kalman Filter Electro Information Technology, 2005 IEEE International Conference on, Publication Date: 22-25 May 2005, On page(s): 1- 5.
70. Kraft, E. (2003), A quaternion-based unscented Kalman filter for orientation tracking. Volume 1 of the Proceedings of the Sixth International Conference of Information Fusion, pp.47 – 54.
71. Kushner, H.J. (1967), The dynamics of many physical systems are nonlinear and non-symmetric; Dynamical equations for optimum non-linear filtering. *Journal of Differential Equations*, 2, 179-190.
72. Lee, J.K., Jekeli, C. (2009), Improved Filter Strategies for Precise Unexploded Ordnance Geolocation using IMU/GPS integration, Journal of Navigation, JULY 2009, VOL. 62, NO. 3, 365–382.
73. Li, X. (2008), Comparing the Kalman filter with a Monte Carlo-based artificial neural network in the INS/GPS vector gravimetric system, Journal of Geodesy, DOI 10.1007/s00190-008-0293-y.
74. Liu, S., Chen, R. (1998), Sequential Monte Carlo Methods for Dynamic Systems, *Journal of the American Statistical Association*, Vol 93, 1032-1044, 1998.
75. Mackay, D.J.C. (1992), A practical Bayesian framework for backpropagation networks, *Neural Computation*, 4, 448-472, 1992.
76. Maybeck, P. S. (1979), *Stochastic models, estimation and control*: Academic Press, New York, 1979.
77. Meditch, J.S. (1969), *Stochastic Optimal Linear Estimation and Control*. McGraw-Hill, New York, 1969.
78. Mehra, R. K. (1972), Approaches to adaptive filtering, *IEEE Trans. Automat. Contr.*, AC-17, pp. 693-698.
79. Mendel, J. M., McLaren, R. W. (1970), *Reinforcement learning control and pattern recognition systems*. In J. M. Mendel, & K. S. Fu (Eds.), Adaptive, learning and pattern recognition systems: Theory and applications (pp. 287-318). New York: Academic Press.
80. Nassar, S. (2003), Improving the Inertial Navigation System (INS) Error Model for INS and INS/DGPS Applications. Ph.D. Thesis, University of Calgary, UCGE Report No.20183.
81. Naveaua, P., Gentonb, M.G., and Shenc, X. (2005), A Skewed Kalman Filter, *Journal of Multivariate Analysis*, 2005, 382 – 400.
82. Nordlund, P.J., Gustafsson, F. (2001), Sequential Monte Carlo filtering techniques applied to integrated navigation systems. Volume 6 of the Proceedings of the American Control Conference, 25-27 June 2001, pp.4375 – 4380.
83. Nordlund, P.J. (2002), Sequential Monte Carlo filters and integrated navigation, Ph.D.

Dissertation, Linkoping University, Linköping, Sweden, 2002.
84. Osman, A., Noureldin, A., Nassar, S., and El-Sheimy, N. (2003), INS/DGPS Integration Utilizing Wavelet Multi-Resolution Analysis. ION National Technical Meeting, 22-24 January 2003, Anaheim, CA, pp.704-710.
85. Petovello, M.G. (2003), Real-time Integration of a Tactical-Grade IMU and GPS for High-Accuracy Positioning and Navigation. Ph.D. Thesis, University of Calgary, UCGE Report No. 20173.
86. Pourtakdoust S. H., Ghanbarpour A. H. (2007), An Adaptive Unscented Kalman Filter for Quaternion Based Orientation Estimation in Low Cost AHRS, Journal of Aircraft Engineering and Aerospace Technology , Vol. 79, No. 5, pp. 485-493, Emerald Group Publishing, 2007.
87. Rauch, H. E., Tung, F., and Striebel, C. T. (1965), Maximum likelihood estimates of linear dynamic systems, *AIAA J*. vol. 3. No. 8, pp. 1445-1450, 1965.
88. Reddy, G., Herr, H. (2006), Using a Gimbal to Calibrate Inertial sensors, Position, Location, And Navigation Symposium, 2006 IEEE/ION, April 25-27, 2006 Page(s):744 – 749.
89. Redmill, K.A., Kitajima, T., and Ozguner, U. (2001), DGPS/INS integrated positioning for control of automated vehicle, Proceedings of the IEEE Intelligent Transportation Systems, 25-29 Aug. 2001, pp.172 – 178.
90. Rogers, R.M. (2000), *Applied Mathematics in Integrated Navigation Systems*. AIAA Education Series, American Institute of Aeronautics and Astronautics, Inc., Reston, VA, 2000.
91. Rubin, D.B. (1998), Using the SIR algorithm to simulate posterior distributions, in J.M. Bernardo, M.H. DeGroot, D.V. Lindley, and A.F.M. Smith Ed., Bayesian Statistics 3, Oxford University Press, pp. 385-402, 1998.
92. Rumelhart, D. E., Hinton, G. E., and Williams, R. J. (1986), Learning representations by back-propagating errors. *Nature*, 323:533--536.
93. Salychev, O., Schaffrin, B., (1992), New filter approaches for GPS/INS integration, in *Proc. 6th Intl. Geodetic Symp. on Satellite Positioning*, pp. 670–680, Columbus, OH, March 1992, Vol. II, eds Kumar, M. & Fell, P.J.
94. Salychev, O. (1999), *Inertial Systems in Navigation and Geophysics*, Bauman MSTU Press, Moscow, 1999.
95. Salytcheva, A.O. (2004), Medium Accuracy INS/GPS Integration in Various GPS Environments. M.Sc. Thesis, University of Calgary, UCGE Report 20200.
96. Sarkka, S. (2006), Recursive Bayesian Inference on Stochastic Differential Equations. Doctoral dissertation, Helsinki University of Technology Laboratory of Computational Engineering Publications, 2006.
97. Sarkka, S. (2008), Unscented Rauch--Tung--Striebel Smoother, *Automatic Control, IEEE Transactions on,* Volume 53, Issue 3, April 2008 Page(s):845 - 849.
98. Schaffrin, B. (1994), Quality Control for sequential GPS Satellite data, "COMPSAT' 94 Short Communications in Computation Statistics, Vienna, Austria, Aug. 1994, pp. 68-70.
99. Schaffrin, B. (1995), On some alternatives to Kalman filtering, in Geodetic Theory Today, pp. 235–245, ed. Sans`o, F., Springer Series, IAG-Symp., No. 114, Springer,

Berlin.
100. Scherzinger, B.M. (2000), Precise robust positioning with inertial/GPS RTK. Proceedings of the 13th International Technical Meeting of the Satellite Division of the Institute of Navigation**,** September 19-22, 2000, Salt Palace Convention Center, Salt Lake City, Utah, The Institute of Navigation, Alexandria, VA., pp. 155-162.
101. Schwarz, K. P. (1999), Adaptive Kalman Filtering for INS/GPS, *Journal of Geodesy*, Volume 73, Number 4 / May, 1999.
102. Shin, E.H. (2001), Accuracy Improvement of Low Cost INS/GPS for Land Application. M.Sc. Thesis, University of Calgary, UCGE Report No. 20156.
103. Shin, E.H. (2005), Estimation Techniques for Low-Cost Inertial Navigation. Ph.D. Thesis, University of Calgary, UCGE Report 20219.
104. Simms, J., Carin L. (2004), Innovative navigation systems to support digital geophysical mapping ESTCP #200129 phase II demonstrations. Revised Report, September 2004, U.S. Army Corps of Engineers Engineer Research and Development Center, Vicksburg, MS.
105. Simon, D. (2006), *Optimal State Estimation: Kalman, H-infinity, and Nonlinear Approaches*, John Wiley & Sons, New Jersey, 2006.
106. Skaloud, J. (1995), Strapdown INS Orient ation Accuracy with GPS Aiding. MSc Thesis, Department of Geomatics Engineering, University of Calgary, Calgary, Alberta, Canada, UCGE Report No. 20079.
107. Smith, A.F.M., Gelfand, A.E. (1992), Bayesian statistics without tears: a sampling-resampling perspective, American Statistician, 46, 84-88, 1992.
108. Song, Q., Han, J.D. (2008), An Adaptive UKF Algorithm for the State and Parameter Estimations of a Mobile Robot, Acta Automatica Sinica, Volume 34, Issue 1, January 2008, Pages 72-79**.**
109. St-Pierre, M., Gingras, D. (2004), Comparison between the unscented Kalman filter and the extended Kalman filter for the position estimation module of an integrated navigation information system, IEEE Intelligent Vehicles Symposium, 14-17 June 2004, pp.831 – 835.
110. Tarokh, A. B., Miller, E. L., Won, I. J. and Huang, H. (2004), Statistical classification of buried objects from spatially sampled time or frequency domain electromagnetic induction data, *Radio Science*, Vol 39, Np. 4, July/August, 2004, p RS4S05-1-RS4S05-11.
111. Titterton, D.H., Weston, J.L. (2004), *Strapdown Inertial Navigation Technology*. Peter Peregrinus, Piscataway, NJ, 2004.
112. U.S. Army Corps of Engineers (2006), Innovative navigation systems to support digital geophysical mapping ESTCP #200129, Phase III APG demonstrations and Phase IV development. Final Report, 17 February 2006, U.S. Army Corps of Engineers, Engineering and Support Center, Huntsville, AL.
113. Van der Merwe, R., Doucet, A., de Freitas, N., and Wan, E. (2000), The unscented particle filter. Technical Report CUED/F-INFENG/TR 380, Engineering Department, Cambridge University, Cambridge, England.
114. Van Der Merwe, R., Wan, E. (2004), Sigma-Point Kalman Filters For Integrated Navigation. Proceedings of the 60th Annual Meeting of The Institute of Navigation (ION), Dayton, Ohio, June 2004.

115. Vernaza, P., Lee, D. D. (2006), Rao-Blackwellized Particle Filtering for 6-DOF Estimation of Attitude and Position via GPS and Inertial Sensors, Proceedings of the 2006 IEEE International Conference on Robotics and Automation, Orland, Florida, May 2006.
116. Wan, E.A., van Der Merwe, R. (2001), The unscented Kalman filter. Chapter 7 in: Simon Haykin (Ed.), *Kalman Filtering and Neural Networks*, John Wiley & Sons, New York.
117. Wang, J.J., Wang, J., Sinclair, D., and Watts, L. (2006), A neural network and Kalman filter hybrid approach for GPS/INS integration, 12th IAIN Congress & 2006 Int. Symp. on GPS/GNS*S*, Jeju, Korea, 18-20 October, 277-282.
118. Wang, J.J., Ding, W., and Wang, J., (2007), Improving adaptive Kalman Filter in GPS/SDINS integration with neural network, 20th Int. Tech. Meeting of the Satellite Division of the U.S. Inst. of Navigation, Fort Worth, Texas, 25-28 September, 571-578.
119. Welch, G., G. Bishop, (2001), *An Introduction to the Kalman Filter*, Chapel Hill. SIGGRAPH, 2001.
120. Yi, Y., Grejner-Brzezinska, D.A. (2006), Tightly-coupled GPS/INS Integration Using Unscented Kalman Filter and Particle Filter. ION GNSS 19th International Technical Meeting of the Satellite Division, 26-29 September 2006, pp.2182-2191.
121. Zhan R., Wan, J. (2006), Neural network-aided adaptive unscented Kalman filter for nonlinear state estimation, Signal Processing Letters, IEEE Volume 13, Issue 7, July 2006 Page(s):445 – 448.
122. Zhang, H.T. (2006), Performance Comparison of Kinematic GPS Integrated with Different Tactical Grade IMUs. M.Sc. Thesis, University of Calgary, UCGE Report 20237.
123. Zhang, P., Gu, J., Milios, E.E., and Huynh, P. (2005), Navigation with IMU/GPS/digital compass with unscented Kalman filter. Volume 3 of the Proceedings of the IEEE International Conference on Mechatronics and Automation, pp.1497 – 1502.
124. Zhang, X. (2003), Integration of GPS with a Medium Accuracy IMU for Metre-Level Positioning. M.Sc. Thesis, University of Calgary, UCGE Report No. 20178.